

ELECTROCHEMICAL METAL NANOWIRE GROWTH FROM SOLUTION

Zur Erlangung des akademischen Grades

Doktor im Ingenieurwesen

(Dr.-Ing.)

Von Alexander Nerowski

Geboren am 10. Juni 1984 in München

TU Dresden, Fakultät Maschinenwesen, Institut für Werkstoffwissenschaften,
Lehrstuhl für Materialwissenschaft und Nanotechnik

1. Gutachter: Prof. Dr. Gianaurelio Cuniberti, TU Dresden
2. Gutachter: Prof. Dr. Dominique Vuillaume, CNRS Lille

Tag der Verteidigung: 29.05.2013

Erklärung

a) Hiermit versichere ich, dass ich die vorliegende Arbeit ohne unzulässige Hilfe Dritter und ohne Benutzung anderer als der angegebenen Hilfsmittel angefertigt habe; die aus fremden Quellen direkt oder indirekt übernommenen Gedanken sind als solche kenntlich gemacht.

b) Bei der Auswertung des Materials sowie der Herstellung des Manuskripts habe ich Unterstützungsleistungen von folgenden Personen erhalten:

Herr Dr.-Ing. Uwe Mühle (Unterkapitel 5.2)

Frau Dipl.-Ing. Ulana Cikalova (Anhang)

Herr M.Sc. Fatih Nadi Gür (Kapitel 6)

Herr Dipl.-Ing. Jürgen Nicolai (Anhang)

Herr Dipl.-Ing. Markus Pötschke (Unterkapitel 3.2 und Kapitel 5)

Herr Dipl.-Phys Ulrich Wiesenhütter (Unterkapitel 5.2)

Herr Tobias Janik (Kapitel 6)

Frau Yvonne Ritz (Unterkapitel 5.2)

Weitere Personen waren an der geistigen Herstellung der vorliegenden Arbeit nicht beteiligt. Insbesondere habe ich nicht die Hilfe eines kommerziellen Promotionsberaters in Anspruch genommen. Dritte haben von mir keine geldwerten Leistungen für Arbeiten erhalten, die in Zusammenhang mit dem Inhalt der vorgelegten Dissertation stehen.

c) Die Arbeit wurde bisher weder im Inland noch im Ausland in gleicher oder ähnlicher Form einer anderen Prüfungsbehörde vorgelegt und ist auch noch nicht veröffentlicht worden.

d) Die Promotionsordnung der Fakultät Maschinenwesen an der TU Dresden vom 01.07.2001 wird anerkannt.

Kurzfassung

Die Zielstellung der vorliegenden Arbeit ist es, die elektrochemische Herstellung von metallischen Nanodrähten zu einer wettbewerbsfähigen Methode zu machen, die sich mit standardisierten Prozessen, wie z. B. der Lithographie messen kann.

Dies beinhaltet auf der einen Seite die Produktion der Nanodrähte als zuverlässige und reproduzierbare Bauteile, die im nanoelektrischen Schaltungsdesign Verwendung finden können. Daher befasst sich diese Arbeit mit einer systematischen Untersuchung der Ursachen für die Verzweigung von Nanodrähten, den notwendigen Bedingungen um gerades Wachstum zu erlangen und mit den Parametern, die Einfluss auf den Durchmesser der Drähte haben. Der Wuchs von sehr dünnen (bis zu 15 nm), geraden und unverzweigten Nanodrähten aus Platin wird gezeigt.

Auf der anderen Seite ist es erklärtes Ziel, über rein elektronische Anwendungen hinaus zu gehen. Eine Untersuchung der Kristallographie der Nanodrähte zeigt, dass die Drähte aus Nanopartikeln bestehen, die eine gemeinsame kristallographische Orientierung aufweisen. Die Vielseitigkeit der Drähte wird anhand einer Sensoranwendung gezeigt, mit der es möglich ist, einzelne nanoskalige Objekte (wie z. B. Bakterien) zu detektieren.

Abstract

The aim of this work is to make electrochemical metal nanowire growth a competitive method, being up to par with more standardized procedures, like *e.g.* lithography.

This includes on the one hand the production of nanowires as reliable and reproducible parts, potentially suited for nanoelectronic circuit design. Therefore, this work presents a systematic investigation of the causes of nanowire branching, the necessary conditions to achieve straight growth and the parameters affecting the diameter of the wires. The growth of ultrathin (down to 15 nm), straight and unbranched platinum nanowires assembly is demonstrated.

On the other hand, it is the objective to go beyond purely electronic applications. An examination of the crystallography of the wires reveals nanoclusters inside the wire with a common crystallographic orientation. The versatility of the wires is illustrated by implementing them into an impedimetric sensor capable of the detection of single nanoscaled objects, such as bacteria.

Content

Content	V
Figures	VII
Tables	VIII
Abbreviations and Variables	IX
1 Introduction	1
1.1 Motivation	1
1.2 State-of-the-Art	3
1.3 Scope of This Thesis	4
2 Materials and Methods	6
2.1 Lithography	7
2.2 Tip-Probing Station	10
2.3 Others	12
3 Physical Background and Theory	14
3.1 Kinetic Model for Nanowire Growth	14
3.1.1 Formalism	15
3.1.2 Results	22
3.2 Dissociation Scheme of K_2PtCl_4	29
4 Nanowire Growth with DEP	33
4.1 Characterization of Solution	33
4.1.1 TEM Investigation of Clusters in Solution	33
4.1.2 Cyclic Voltammetry	34
4.2 Growth Kinetics and Morphology of the Wires	36
4.2.1 Temperature Dependence	38
4.2.2 Concentration Dependence	42
4.2.3 Dependence on Applied Voltage Amplitude	46
4.2.4 Other Signal Variations	48
5 Nanowire Growth with DENA	53
5.1 Effect of Setup Parameters on Morphology	53
5.1.1 Concentration and Frequency Dependence	53
5.1.2 Electric Field Impact on the Morphology	59
5.1.3 Contacting the Nanowires	62
5.1.4 Wave Form Variation	63
5.2 TEM Investigations of Nanowires	64

5.2.1	Presence of Clusters in Platinum Nanowires.....	65
5.2.2	Lattice Orientation of the Clusters in the Nanowire.....	66
5.2.3	Influence of the Waveform on the Crystallinity and Morphology	69
5.2.4	Growth at Electrode Edges.....	72
6	Sensor Application	75
6.1	Sensor Characterization.....	76
6.1.1	AC Characteristics of the Wires.....	76
6.1.2	Gap Formation	80
6.2	Measured Data.....	81
6.2.1	Electric Properties of <i>E. coli</i>	81
6.2.2	Sensitivity of the Nanowire-Based Sensor.....	83
6.3	Future Perspective	85
7	Closing Remarks	87
7.1	Conclusion.....	87
7.2	Outlook.....	88
	Appendix	91
	Solution of Differential Equation (3-16).....	91
	Root-Mean-Square of Superimposed Sine Waves	92
	Fractal Dimension of Wires in Subsection 5.1.4	93
	Scientific Output.....	96
	Acknowledgements	97
	Curriculum Vitae	99
	References	100

Figures

Figure 1-1. Silver nanowires as waveguides.....	1
Figure 1-2. Bottom-up grown nanowires.....	2
Figure 1-3. Scheme of electrochemical nanowire growth experiment.....	3
Figure 2-1. Interdigitated electrode design.....	9
Figure 2-2. Tip-to-tip design.....	9
Figure 2-3. Setup of nanowire growth experiments.....	11
Figure 2-4. Temperature control of samples.....	12
Figure 3-1. Physical principle of the DEP force.....	14
Figure 3-2. Scheme of the convection-diffusion model.....	16
Figure 3-3. Growth velocity of the nanowire dependent on the temperature.....	25
Figure 3-4. Concentration profile of neutral, polarizable molecules (voltage variation).....	27
Figure 3-5. Concentration profile of neutral, polarizable molecules (bulk concentration variation).....	29
Figure 3-6. Reaction scheme of the dissociation of K_2PtCl_4 in water.....	31
Figure 3-7. Dissociation scheme of 10 μM K_2PtCl_4 in water.....	32
Figure 4-1. TEM images of platinum clusters.....	34
Figure 4-2. Cyclic voltammetry of 10 μM K_2PtCl_4 at room temperature.....	35
Figure 4-3. Growth velocity of nanowires in dependence on the temperature.....	40
Figure 4-4. Nanowires grown at different substrate temperatures.....	42
Figure 4-5. Measured nanowire growth velocity as a function of the <i>cis</i> - $PtCl_2$ concentration at 298 K.....	43
Figure 4-6. Measured nanowire growth velocity as a function of the <i>cis</i> - $PtCl_2$ concentration at 316 K.....	44
Figure 4-7. SEM-images of wires grown at different <i>cis</i> - $PtCl_2$ -concentrations.....	45
Figure 4-8. Nanowire growth velocity in dependence on the peak voltage.....	46
Figure 4-9. Nanowire morphology for different peak voltages.....	47
Figure 4-10. Number of side-branches at the nanowires per nanowire length.....	48
Figure 4-11. Nanowires grown at different frequencies.....	50
Figure 4-12. Nanowires grown with signals shaped differently than sine.....	52
Figure 5-1. SEM-images of Pt nanowires grown from acidic solution.....	54
Figure 5-2. Dependence of the nanowire diameter on frequency and concentration.....	57

Figure 5-3. Schematics of the nanowire growth process	59
Figure 5-4. Dependence of nanowire morphology on surrounding electric field	61
Figure 5-5. Contacting of straight, thin wires.....	62
Figure 5-6. SEM-images of the evolution of morphology according to the wave form	64
Figure 5-7. TEM image of Pt nanowires grown at the sides of the gold microelectrodes.....	66
Figure 5-8. Investigation of clusters of the wire in Figure 5-7a.....	67
Figure 5-9. Investigation of clusters of the wire in Figure 5-7b and c.....	68
Figure 5-10. Wire in Figure 5-7b at the interface to the gold electrode	69
Figure 5-11. Investigation of a kinked wire	70
Figure 5-12. Nanowires growing down from an edge	73
Figure 6-1. Setup of sensor concept	75
Figure 6-2. Electrical behavior of a typical nanowire	79
Figure 6-3. Creation of the gap	80
Figure 6-4. Trapped <i>E. coli</i> in a gap between nanowires	83
Figure 6-5. Sensor impedance versus frequency	84
Figure 6-6. Concept figure of future sensor chip	85
Figure A-1. Selection of different regions of interest in SEM images.....	93
Figure A-2. Example of an SEM image converted to a binary image.....	94
Figure A-3. Fractal dimensions of nanowires.....	95

Tables

Table 0-1. Variables and their meanings	IX
Table 0-2. Abbreviations.	X
Table 2-1. Overview of experimental methods.....	6
Table 3-1. Simulation parameters for nanowire growth.....	23
Table 3-2. Reaction rates for K_2PtCl_4 hydrolysis at $T = 298$ K.	31

Abbreviations and Variables

Table 0-1. Variables and their meanings. Vector variables may occur without the arrow, which refers to a component of the vector specified in the text. Units are as indicated, if not stated otherwise in the text. Some symbols have indices which correspond to a certain state, condition, position, etc. If so, the context is further explained in the text.

Symbol	Meaning [unit where applicable]
A	Area [m ²]
A	Integration constants, units given in text
a	Fit parameters, units given in text
C	Capacity [F]
c	Concentration [1/m ³]
D	Diffusion coefficient [1/(m ² s)]
d	Diameter [m]
\vec{E}	Electric field (dependent on context) [V/m]
E	Energy (dependent on context) [eV]
\vec{e}_r	Radial unity vector [1]
\vec{F}	Force [N]
f	Frequency of applied electrical voltage [Hz]
i	Counter in sums [m]
\vec{j}	Particle flux density (dependent on context) [1/(m ² s)]
j	Electrical current density (dependent on context) [A/m ²]
$K(\omega)$	Clausius-Mossotti factor [1]
\hat{k}	Reaction rate constant [m/s]
k	Reaction rate (dependent on context), units given in the text
k	Partition coefficient (dependent on context) [1]
k_B	Boltzmann constant [J/K]
L	Phenomenological coefficient [s/(m ³ kg)]
ℓ_{nw}	Length of nanowire [m]
q	Electrical charge [C]
R	Resistance [Ohm]
r	Radial coordinate [m]
St	Stefan-number [1]

T	Temperature [K]
t	Time [s]
V	Time-independent voltage (dependent on context) [V]
V	Volume (dependent on context) [m ³]
v	Time-varying voltage (dependent on context) [V]
v	Velocity (dependent on context) [m/s]
X	Reactance [Ohm]
\vec{x}	Spatial position [m]
Z	Impedance [Ohm]
α	Polarizability (dependent on context) [Cm ² /V]
α	Ratio bulk concentration/concentration at wire (dependent on context) [1]
δ	Skin depth [m]
ϵ	Electrical permittivity [F/m]
η	Dynamic viscosity [Pas]
λ	Wavelength [nm]
μ	Chemical potential [J] (dependent on context)
μ	Magnetic permeability [N/A ²] (dependent on context)
$\tilde{\mu}$	Electrochemical potential [J]
ρ	Charge density [Cm ⁻³]
σ	Conductivity [S/m]
ω	Angular frequency [s ⁻¹]

Table 0-2. Abbreviations.

Symbol	Meaning [unit where applicable]
AC	Alternating current
DC	Direct current
DENA	Directed electrochemical nanowire assembly
DEP	Dielectrophoresis
fcc	face-centered cubic
SEM	Scanning electron microscopy
TEM	Transmission electron microscopy

1 Introduction

1.1 Motivation

One-dimensional nanostructures, *e.g.* nanowires or nanotubes, represent building blocks to realize novel, ultrasmall circuitry with versatile properties.¹⁻³ Among them are *e.g.* thermal and mechanical stability or their extremely high conductivity and suitability for photon transport (see Figure 1-1).⁴⁻⁷

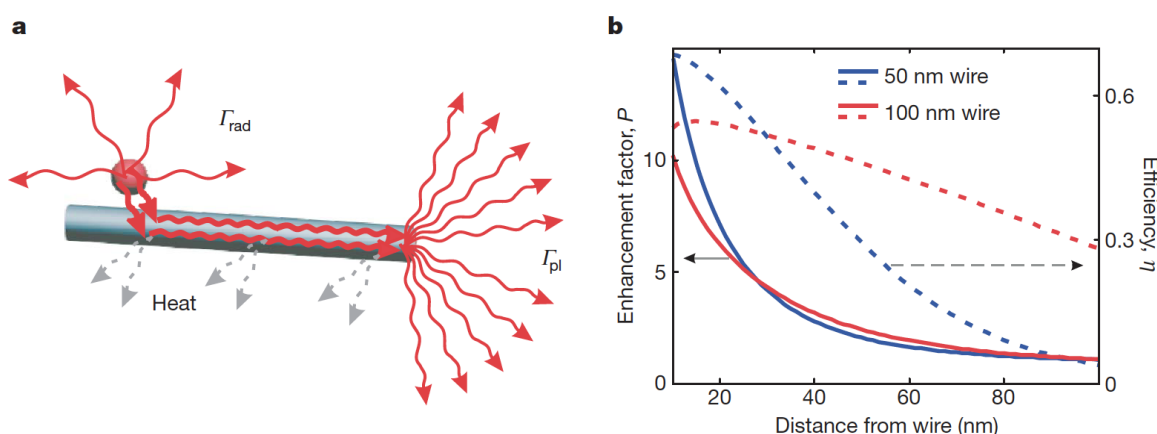


Figure 1-1. Silver nanowires as waveguides as example for the intriguing properties of nanowires (Akimov *et al.*).⁷ (a) Scheme of a quantum dot coupling photons to a nanowire. (b) Waveguide characteristics of nanowires.

Due to their ability to act as parts of an electronic circuit, one-dimensional nanostructures have already performed well as key elements of sensitive sensors. There are two prominent examples of nanostructures which serve as sensors based on electronic read-out.

- Carbon nanotubes, vertical⁸ and horizontal integration⁹ (voltammetric principles, field-effect transistors) and
- Silicon nanowires (field-effect transistors).^{10, 11}

Biomedical sensor applications have been of particular interest, especially due to their high relevance to society.¹² Metal nanowires have mainly found application as interconnects in electronic circuits,¹³ but also *e.g.* as highly specific hydrogen sensors (resistance change).¹⁴ Yet, since metal cannot be gated and thus no field-effect upon analyte exposure occurs, the sensor applications are limited.

Two fundamentally different methods exist to fabricate these one-dimensional nanostructures. In top-down fabrication material is cut from a bulk, until the desired structure is achieved. This includes well-refined processes like etching, nano-printing or electron beam structuring.¹⁵ Yet, there are some severe limitations inherent to this method. First, only two-dimensional structures can be fabricated. Second, the size of lithographically made structures is always limited by the wavelength of the exposure device. These restrictions can be overcome by the alternative bottom-up concept, based on the assembly of nanostructures starting at the atomic or molecular level.

Significant efforts have been made to explore bottom-up fabrication techniques like the vapor-liquid-solid process for semiconducting nanowires, or self-assembly from solution for metal nanowires and other, often more complex geometries.¹⁶⁻¹⁹ The bottom-up approach offers a cost-efficient solution for future electronics as it relies on low material consumption and avoids the use of expensive nanolithography techniques.²⁰ Moreover, this new class of materials is particularly suitable for life-science (*cf.* Figure 1-2a).²¹ However, with the bottom-up method new problems occur: the control of the morphology of the structures remains demanding (see Figure 1-2b).²² Plus, their integration into circuits represents one of the major challenges existing in the field of bottom-up nanowires.²³

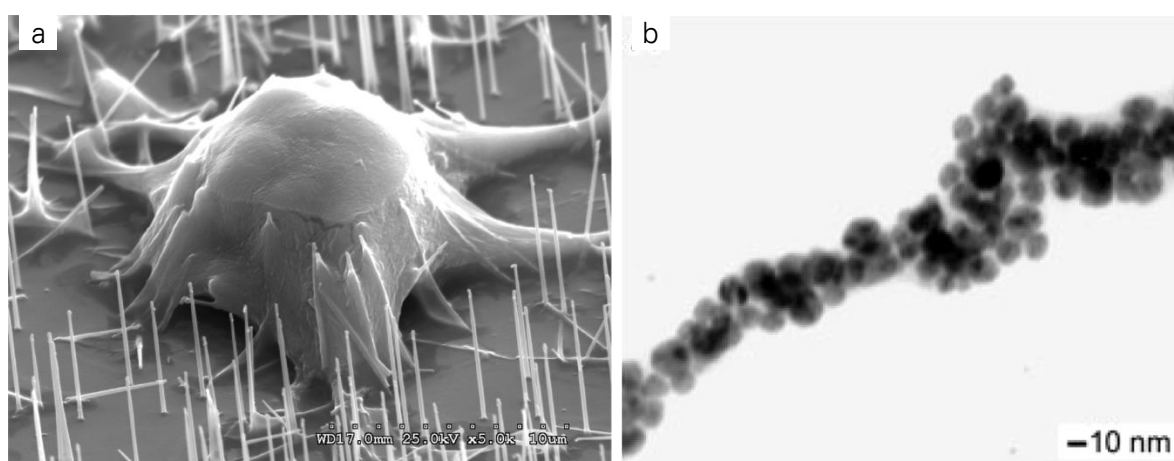


Figure 1-2. Bottom-up grown nanowires. (a) Transmission electron microscopy image of silver nanowires, synthesized from solution (Sun *et al.*).²¹ (b) Si nanowires interfacing a mammalian cell, showing the suitability of nanowires for life-science applications (Kim *et al.*).²²

1.2 State-of-the-Art

In order to address the integration problem, several recently proposed methods involve dielectrophoresis (DEP), the movement of a neutral, polarizable object due to a spatially inhomogeneous electric field.²⁴ DEP has become a powerful tool with various application possibilities.²⁵ For instance, combination of DEP with directed fluid flow can also be employed for guiding nanowires between electrodes in solution to the desired contactsite.^{26, 27} Hermanson *et al.* has realized the growth of microwires directly from metallic clusters in solution using dielectrophoresis, which has the advantage that the wires are directly connected.²⁸ Figure 1-3 shows the setup of such an experiment, which will be also the basis for this work. Soon, the method was employed to grow nanowires from neutral molecules.²⁹

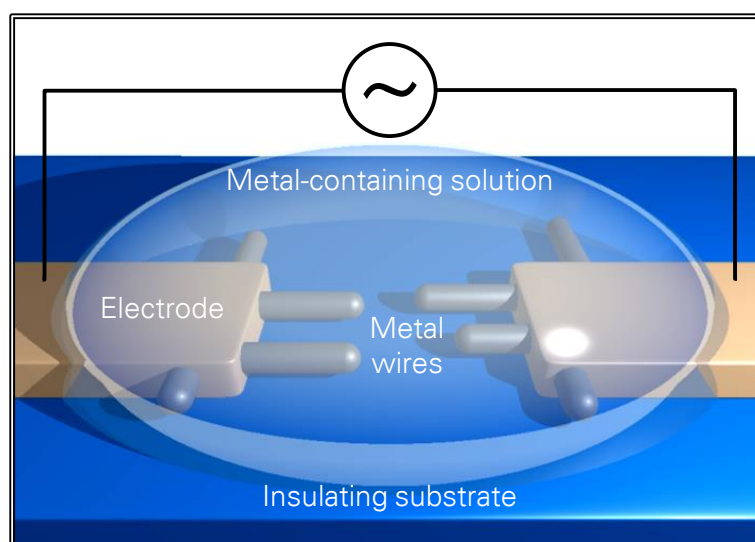


Figure 1-3. Scheme of electrochemical nanowire growth experiment. A drop of metal-containing solution is placed onto an insulating substrate with microfabricated electrodes. Upon application of an AC voltage, the metallic objects in the solution move to the electrode, nucleate and form a wire by electrodeposition.

The nanowires can be grown quickly and with any aspect ratio, in a time frame from seconds up to few minutes, which represents a major improvement compared to time-consuming conventional lithography.³⁰ Also semiconducting clusters could be arranged in this way, which opened up the application of dielectrophoretically grown wires to field-effect sensing.³¹ On the other hand, nanowires can be grown via

assembly of charged metallic complexes, which is termed “directed electrochemical nanowire assembly” (DENA).³² The outcome in both cases is usually a dendritic, curly or thick (several 100 nm) nanowire. Several suggestions to optimize the morphology for both DENA and DEP have been made. Bhatt *et al.* found out that adding a high-viscosity substance to a nanocluster-containing medium increases the straightness of the microwires.³³ Diameter and branching of the nanowires grown using either the DEP or the DENA approach, can be manipulated by changing the parameters of the applied electric signal, *e.g.* amplitude and frequency.^{34, 35} Despite the relative simplicity of both methods, the full control over straightness, diameter, and branching of the grown nanowires has not been achieved so far.³⁶ While these are fundamental requirements in nanoelectronics, it is also important to gain control over the crystallinity of the wire. It determines, for instance, their suitability for plasmonics or their electrical transport properties.³⁶⁻³⁸ For instance, Kawasaki *et al.* investigated the angle of branching in platinum nanowires and related it to crystallographic axes in a face-centered cubic (fcc) crystal, assuming the wires to be monocrystalline.³⁹ To date, a detailed investigation of the crystallinity of electrochemically grown nanowires has not yet been performed.

1.3 Scope of This Thesis

The aim of this work is to allow the electrochemical approaches DENA and DEP to be a competitive method to fabricate nanowires.

This includes on the one hand the production of nanowires as reliable and reproducible parts, potentially appropriate for nanoelectronic circuit design. Therefore, this work presents a systematic investigation of the causes of branching, the necessary conditions to achieve straight growth and the parameters affecting the diameter of the wires.

On the other hand, it is the objective to go beyond purely electronic applications. For reasons discussed above, a detailed examination of the crystallography of the wires is conducted. In the end, the versatility of the wires is illustrated by implementing them into a nanobiosensor application.

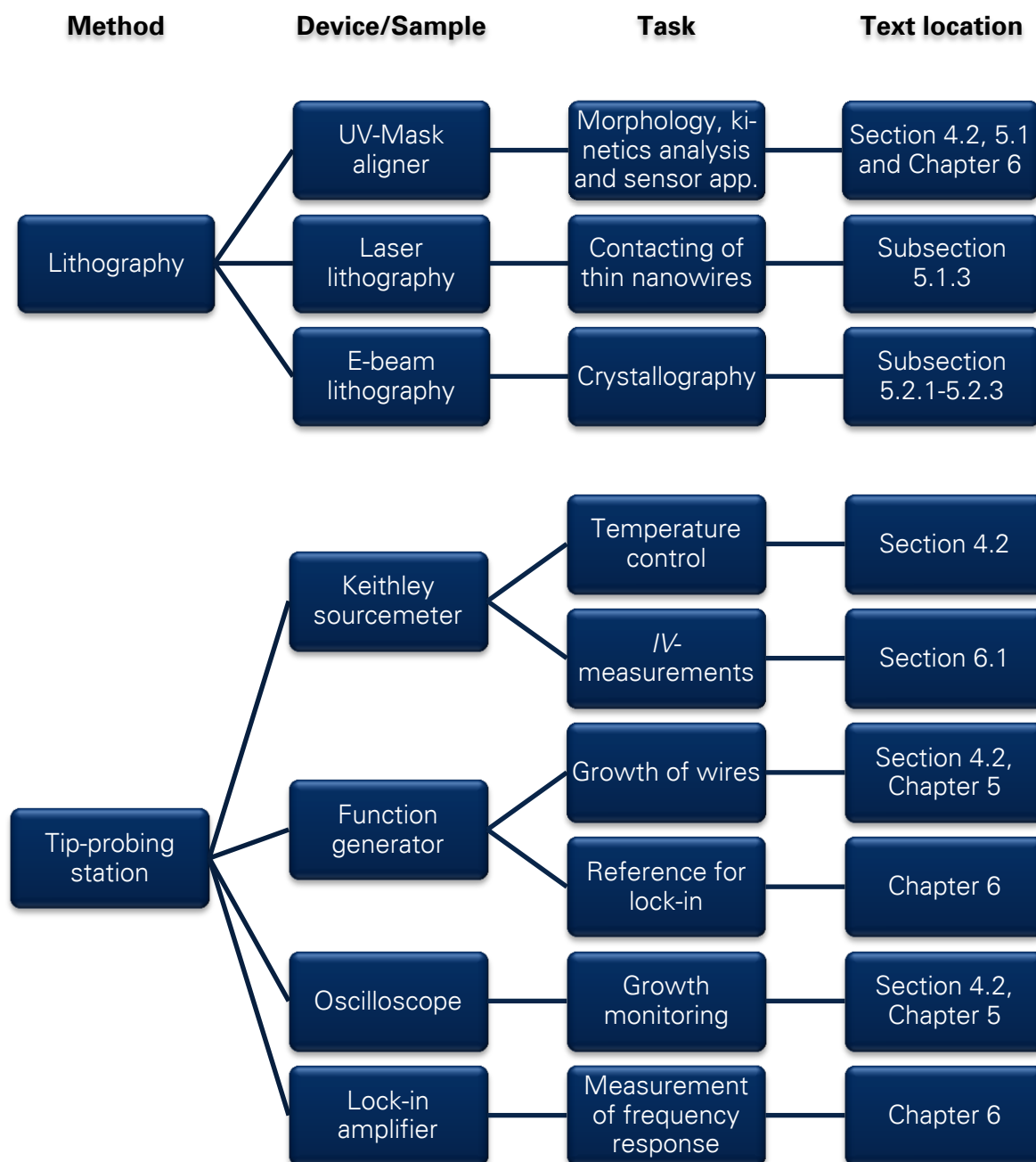
The outline of this thesis is as follows:

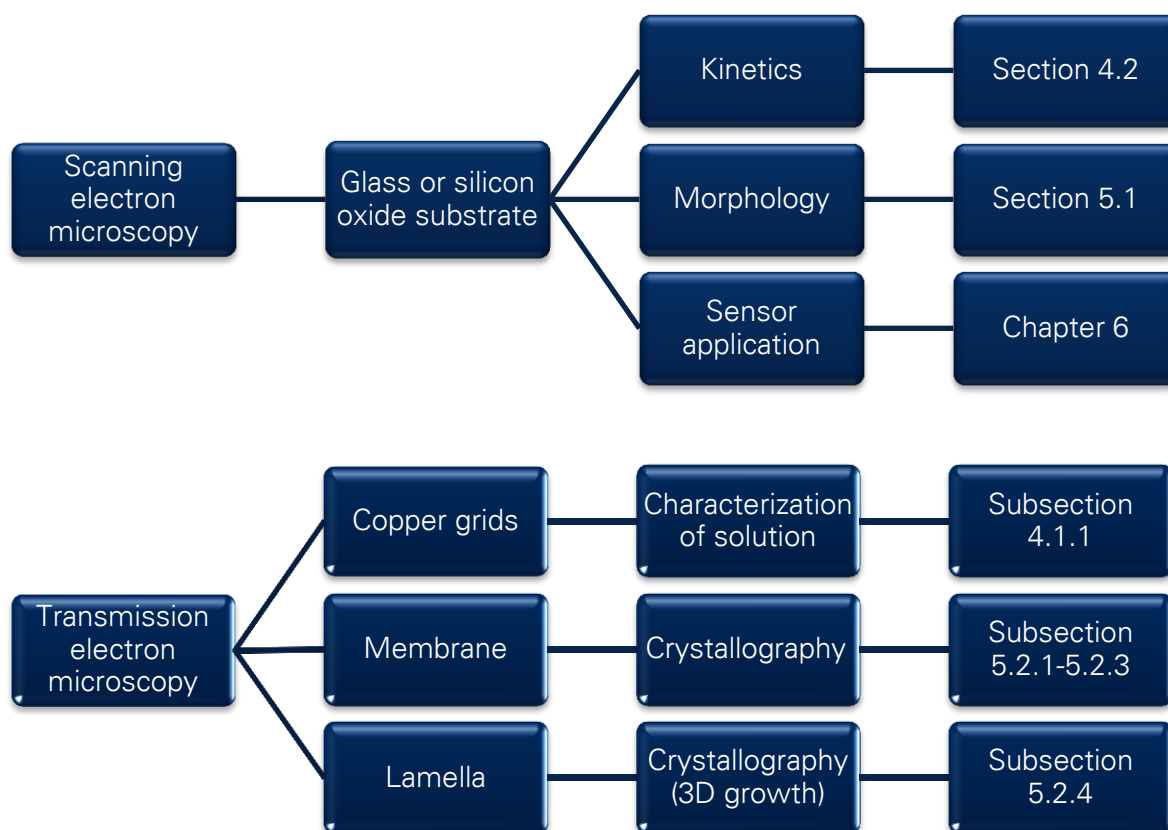
- Chapter 2 provides information about the used equipment and materials.
- Chapter 3 analyzes theoretically the growth process of a nanowire grown with dielectrophoresis for a simple model. The purpose of the chapter is to introduce the concepts of diffusion limitation and reaction limitation in the context of nanowire growth. The gained results explain how the nanowire growth velocity changes upon variation of setup parameters.
- Chapter 4 presents experiments in which nanowires are grown by means of dielectrophoresis (DEP). The nanowire growth velocity is measured at different settings and the resulting data are used to verify the model from Chapter 3. Furthermore, the chapter gives insight into how **branching** occurs at nanowires and how to avoid it.
- Chapter 5 presents experiments in which nanowires are grown by means of directed electrochemical nanowire assembly (DENA). Based on the theoretical study in Chapter 3, pivotal principles how to reduce the **diameter** are gained. Important conclusions on how to achieve **straight wires** are drawn from an examination of the **crystallography** of the nanowires, as well as from a study of the electric field surrounding the nanowire.
- Chapter 6 presents the electrical characterization of the wires and a **sensor application**, based on the measurement of the impedance of nanoscaled objects. The sensor concept shows the possibility of single-object detection. Potential developments are discussed.

2 Materials and Methods

This chapter introduces the various experimental techniques used in this work. Table 2-1 summarizes the methods and their applications as well as where in the text they are used. A detailed description of each method follows afterwards.

Table 2-1. Overview of experimental methods, their applications and the respective passages in the text.





The lithography techniques were used to provide the microelectrode structures on which the nanowire growth took place. These structures were contacted with needles at the tip-probing station in order to perform growth experiments and electrical characterization of the nanowires and the sensor. After the experiments, the samples were investigated using scanning or transmission electron microscopy (SEM/TEM, respectively).

In addition to these main methods, the cyclic voltammetry setup for characterizing the solution (Subsection 4.1.2) and the bacteria preparation for the sensor application (Chapter 6) are described.

2.1 Lithography

The fabrication of the microelectrodes was done using three different kinds of lithography. Table 2-1 provides information which kind was used for what experiments. The choice of lithography type was made according to requirements specific to the experiment and/or substrate. Mask lithography was used for the analysis of the nanowire growth kinetics in Section 4.2, the nanowire morphology in

Section 5.1, the three-dimensional growth in Subsection 5.2.4, and the sensor application in Chapter 6, since only simple exposure was needed. Exposure and precise alignment was necessary for the 2-step lithography as employed in Subsection 5.1.3, which could be accomplished by means of scanning laser lithography. Finally, investigating the crystallography in Subsections 5.2.1 to 5.2.3 demanded very precise structuring, therefore electron-beam lithography was employed.

Three different kinds of substrates were used: 24 mm x 24 mm glass slides (Section 4.2 and Chapter 6) were the solution with the lowest costs. 15 mm x 15 mm silicon wafer pieces with 300 nm SiO₂ (Section 5.1 and Subsection 5.2.4), having a low degree of surface contaminations, are suitable to achieve full control over the nanowire growth morphology. For the TEM-investigations, 50 nm thin silicon nitride membranes (Si₃Ni₄, Tedpella) met the requirements for direct imaging, *i.e.* without further sample preparation (Subsections 5.2.1 to 5.2.3). For the substrates it was crucial to be insulating since otherwise the leakage current through the substrate is too high for electrochemical wire assembly to work.⁴⁰

For both mask and laser lithography, the lithography recipes were the same. A positive photoresist (AR-P 5350, Allresist) was spin-coated on the substrate with 6500 rpm to reach a thickness of 800 nm, followed by subsequent heating on the hotplate at 378 K for 4 min. The exposure with mask lithography (MJB4, Karl Suss Microtec) was performed with a mercury lamp as UV source at a wavelength of $\lambda = 365$ nm for 1.5 s. The laser lithography (DWL66fs, Heidelberg Instruments) exposed the photoresist using a 4 mm write-head at $\lambda = 405$ nm. The structures were developed for 60 s in diluted developer (1 part developer, 2 parts water). 3 nm chromium (adhesion layer) followed by 17 nm gold (electrode material) were thermally evaporated on the substrate at $5 \cdot 10^{-5}$ mbar. The lift-off was done in 1-Methyl-2-pyrrolidinone (NMP 99,5 %, Sigma Aldrich) at 340 K for 45 min.

For e-beam lithography, the recipe differed mainly regarding the photo-resist. A positive resist (PMMA 495K A4, Micro Chem) was spin-coated onto the substrate with a speed of 3500 rpm to reach a thickness of 100 nm. The samples were

exposed using e-beam lithography (Raith 150^{TWO}) and developed with methylisobutylketon/isopropanol (ratio 1:3, Micro Chem) and isopropanol as stopper. The developed structures were then coated by thermal evaporation with 3 nm Cr (adhesion layer) and 15 nm Au (electrode material). The lift-off was done in acetone.

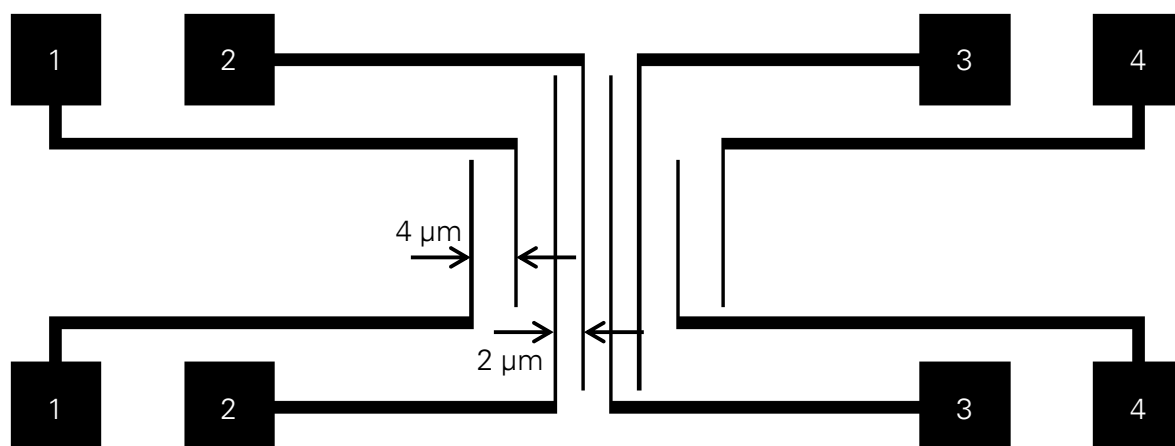


Figure 2-1. Interdigitated electrode design (not to scale). The needles of the tip-probing station contact the square pads (edge length 0.5 mm). The outer electrode pairs (1&4) have a distance of 4 μm and the inner pairs (2&3) a distance of 2 μm to each other. The width of the electrodes was 2 μm .

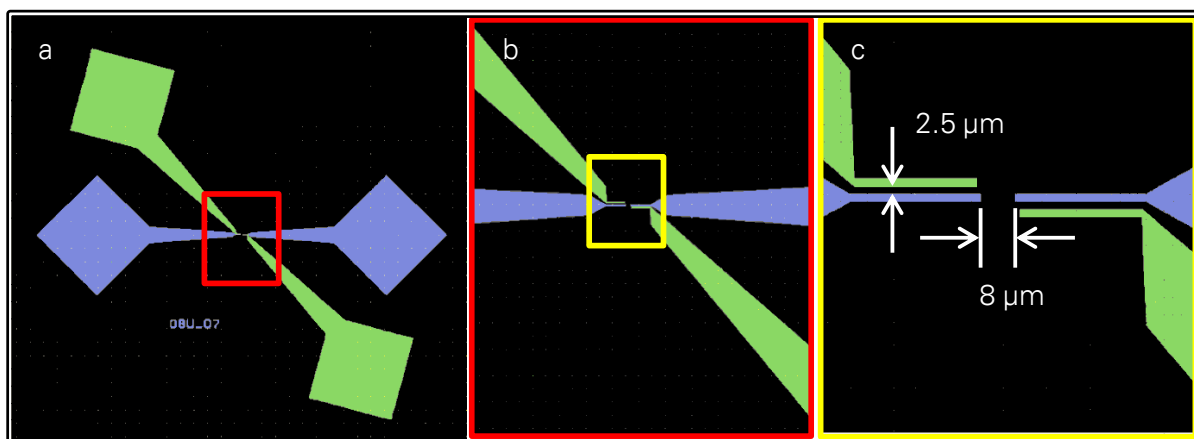


Figure 2-2. Tip-to-tip design (blue layer), including second layer (green) for contacting thin wires. (a) Overview. Square pads represent contact points for needles. (b+c) Zoom-in of design. The width of the electrodes was 2 μm .

Two kinds of structures were employed: the interdigitated electrodes in Figure 2-1 and the tip-to-tip electrodes in Figure 2-2 (blue layer), which could be extended with a second layer (green) to contact wires grown at the side. The interdigitated electrode design was used for the kinetics investigation in Section 4.2, since many nanowires grew along the edges of the electrode and thus statistics could be

performed easily. The nanowires grew at both sides of the electrode, therefore for one experiment only electrode pads with the same number were contacted. The tip-to-tip design on the other hand was used for all other investigations.

2.2 Tip-Probing Station

The tip-probing station comprises a microscope, a chuck with vacuum connection and two needle holders with micropositioners (Karl Suss Microtec) to contact the samples (see Figure 2-3a+b). Before conducting experiments, needles, chuck, and tweezers were rinsed with isopropanol to ensure a contaminant-free environment. The voltage at the electrodes was provided by a function generator (Tektronix AFG320, maximum slew rate: $3.5 \cdot 10^8$ V/s) and observed with an oscilloscope (Tektronix TDS3014). For each growth experiment 15 μ l (for interdigitated electrodes) or 1.5 μ l (for tip-to-tip electrodes) solution were put on the electrodes and an AC voltage was applied. As a result, the nanowires grew between the fingers of the interdigitated electrodes. Specific details about the applied external voltage are provided in the respective sections. The varied setup parameters included the bulk concentration of the metal species in solution c_{∞} , the amplitude and shape (sine, square...) of the applied AC voltage V_p , the frequency of the same f and the temperature of the substrate T . Figure 2-3c displays the electric equivalent circuit for the used setup. It has to be noted that the solutions used in the experiments for this work were always highly diluted. Therefore, the resistance of the solution was much higher than the input impedance of the oscilloscope (1 M Ω), which means that in good approximation the full output voltage of the function generator was applied to the solution during nanowire growth. The oscilloscope was the measurement device for the growth experiments, a lock-in amplifier (Stanford Research, SR830) for the impedance measurements in Chapter 6. The function generator served as reference signal for the lock-in amplifier. I/V -measurements were carried out with a "sourcemeter" (supply and measurement in one device, Keithley 2602 System SourceMeter).

In Chapters 4 and 6, the nanowires were grown from a K_2PtCl_4 salt solution in different concentrations (see respective sections). A sudden increase in voltage at

the oscilloscope indicated the connection of two nanowires and the voltage was turned off. In Chapter 5, all experiments were conducted with an acidic solution. The solution was diluted with deionized water from a bought H_2PtCl_6 stock-solution (8 wt.%, Sigma Aldrich) until a concentration of $200\text{ }\mu\text{M}$ was reached. Since the solution becomes unstable with increasing pH, the experiments were conducted within 3 hours maximum after dilution.⁴¹ The stock-solution was kept in the dark to protect it from UV-influences. After a growth time of 5 min, the function generator was switched off.

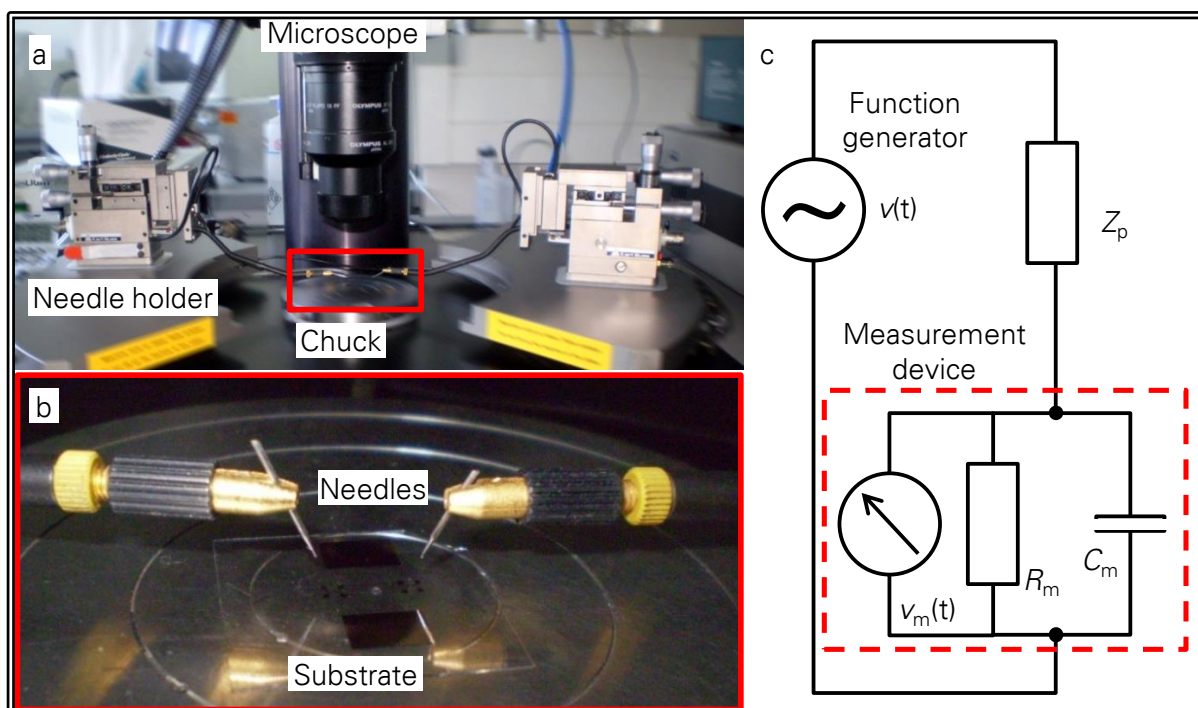


Figure 2-3. Setup of nanowire growth experiments. (a) Picture of probe station with microscope, chuck and needle holder. (b) Picture of needles contacting a glass substrate (marked section in panel a). (c) Equivalent circuit of setup with Z_p being the impedance of the object between the needles. The input impedance of the measurement device is modelled as a capacitor and a resistor in parallel.

The temperature of the glass slide was controlled by a thermoelectric element and measured with a negative temperature-coefficient resistor (NTC EPCOS Type B57861S, R/T No. 8016) glued with conductive silver paint on the surface of the thermoelectric element (*cf.* Figure 2-4a). The dual channel Keithley sourcemeter served as current source for the thermoelectric element and as resistance measurement device for the NTC (Proportional-integral control loop). Since Peltier

elements are not as suitable for cooling as for heating, the chuck was connected to a cold-water reservoir, to make low temperatures available. With this setup, the substrate temperature was varied from 289 K to 316 K.

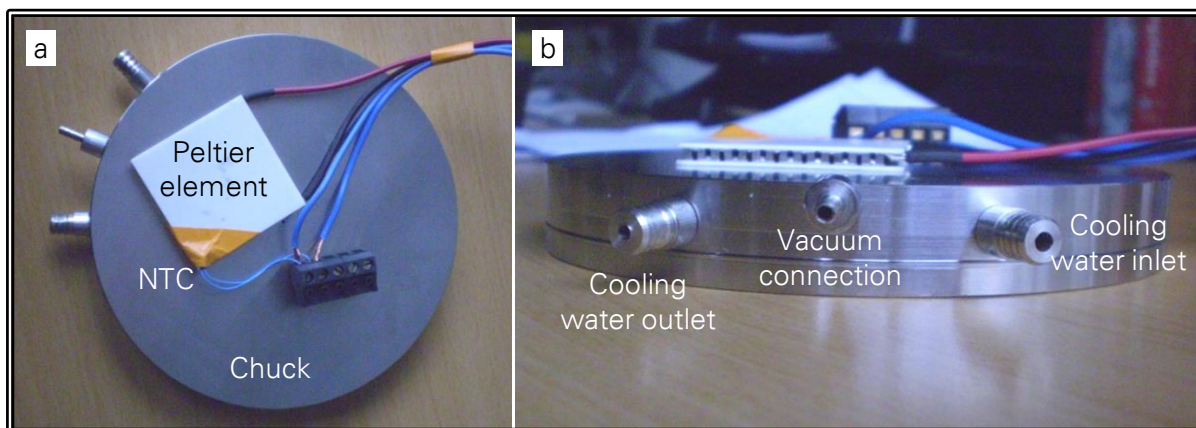


Figure 2-4. Temperature control of samples. (a) Peltier element with NTC temperature sensor. (b) Chuck with Peltier element on top and connections for cooling water and vacuum tube.

2.3 Others

After the experiments, the nanostructures were visualized using either SEM or TEM. For SEM characterization, the samples were mounted on a sample holder and, in case of glass substrates, thermally coated with 3 nm chromium or sputtered with carbon in order to make the sample conductive. The silicon substrates were investigated on the sample holders as they were.

The SEM images were taken with either the Philips XL 30 ESEM-FEG or the Zeiss DSM 982 Gemini. Depending on the sample, the acceleration voltage was chosen between 1 kV and 5 kV at a working distance of 5 mm.

TEM images of clusters in solution (Subsection 4.1.1) were taken with the Zeiss EM 912 Omega (120 kV). Nanowires on the silicon nitride membranes (Subsections 5.2.1 to 5.2.3) were investigated using the FEI Titan 80-300 (300 kV). The nanowire in a lamella, cut out with a focused ion beam (Subsection 5.2.4), was investigated using the Zeiss Libra 200 (200 kV).

The cyclic voltammetry setup to characterize the 10 μM K_2PtCl_4 solution (see Subsection 4.1.2), comprised a common three-electrode cell, as *e.g.* described by

Mabbot.⁴² One beaker contained the analyte solution, as well as working and counter electrode (square platinum). A capillary was placed ~5 mm in front of the working electrode and, in combination with a diaphragm, served as salt bridge to the second beaker containing 3 M KCl as electrolyte and the reference electrode (Ag/AgCl in saturated KCl). A potentiostat (Princeton Applied Research EG&G 273) was used to control the voltage between reference and working electrode, which was scanned from -2 V to +2 V at 30 mV/s.

For the sensor application in Chapter 6, the *Escherichia coli* (*E. coli*) strain MC4100-YFP (Bauer Center for Genomics Research) was incubated in a nutrition medium. 1 ml of the solution containing the nutrients and the bacteria was centrifuged at 10^3 rpm for 20 min. The supernatant was disposed and the tube was filled with 1 ml double-distilled water to wash the bacteria. The bacteria were mixed with the water until the solution was a homogenous emulsion and the tube was again centrifuged as above. The supernatant was disposed and the final bacteria suspension was obtained by adding 1 ml double-distilled water and mixing it with the precipitated bacteria.

3 Physical Background and Theory

To prove the present understanding of nanowire assembly, this chapter provides a theoretical analysis of the wire growth, which includes the diffusion of the platinum species and the effect of the dielectrophoretic force (hereafter DEP force) on the complexes. In a first step, a model for the nanowire growth for neutral objects in solution is discussed, and thereafter the validity of the model for charged objects in solution (DENA). Chapter 4, compares the results with experimental measurements of the nanowire growth velocity.

3.1 Kinetic Model for Nanowire Growth

In a very simplified model, electrochemically assisted nanowire growth from solution involves two phases: movement of an object in solution and deposition of the same or of its reduced form. Depending on the electric properties of this object, different motion mechanisms take effect. In this phase, diffusion according to the Fick laws and motion due to forces exerted on the objects by the electric field are considered. For electrically charged objects, particularly ions, the force is called the Coulomb force \vec{F}_C . For neutral objects, *e.g.* uncharged clusters or molecules, motion in the electric field is caused by the dielectrophoretic (DEP) force \vec{F}_{DEP} , which describes the force on a neutral, polarizable object due to a spatially inhomogeneous field.²⁴

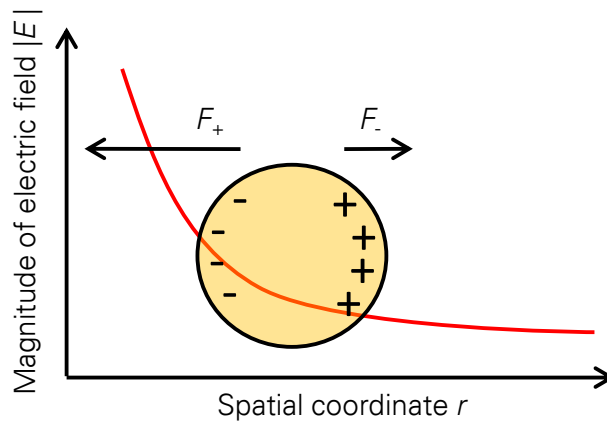


Figure 3-1. Physical principle of the DEP force.

Due to charge separation in the object upon application of an external electric field, different field magnitudes exert different forces F_+ and F_- to the “charge clouds” in the object. The resulting net force causes the movement towards the electric field source (*cf.* Figure 3-1).

3.1.1 Formalism

To estimate the concentration profile of neutral molecules under the influence of convection, diffusion and reaction at the nanowire tip during the wire growth, steady-state conditions are assumed. The latter is justified, because the transition time from non-steady state to steady state is short compared to the period of the applied electrical voltage f^{-1} .^{30, 34} This model is based on the fact that the dominant part of the electric field emerges from the nanowire tip and the relevant mechanisms for the growth process take place in the tip vicinity. A more general form of the Fick laws is applied, stating that two influences, namely the DEP force \vec{F}_{DEP} and the gradient of the chemical potential μ , are the causes for the particle flux density \vec{j} :

$$\vec{j} = L(\vec{F}_{\text{DEP}} - \text{grad } \mu) \quad (3-1)$$

and

$$\frac{\partial c}{\partial t} = -\text{div } \vec{j}. \quad (3-2)$$

This is similar to an approach demonstrated by Eftekhari, who developed a formalism for flux density under the influence of gravity and a concentration gradient using Onsager’s phenomenological coefficients L .⁴³ The chemical potential is dependent on the ratio of the substance’s local activity to that of the bulk. The activity comprises interparticular forces on the one hand and the concentration on the other hand. For dilute solutions, interparticular forces can be neglected and after Schwabe,⁴⁴ the chemical potential is in good approximation

$$\mu = k_B T \log \frac{c(r)}{c_\infty}. \quad (3-3)$$

Since the metallic nanowire tip is considered to be a sphere electrode (*cf.* Figure 3-2), the problem is treated radially, which means that $\vec{F}_{\text{DEP}} = F_{\text{DEP}} \vec{e}_r$ and $\vec{j} = j \vec{e}_r$, where F_{DEP} and j stand for the radial component of the DEP force and the flux density, respectively. \vec{e}_r is the radial vector pointing away from the inner sphere electrode.

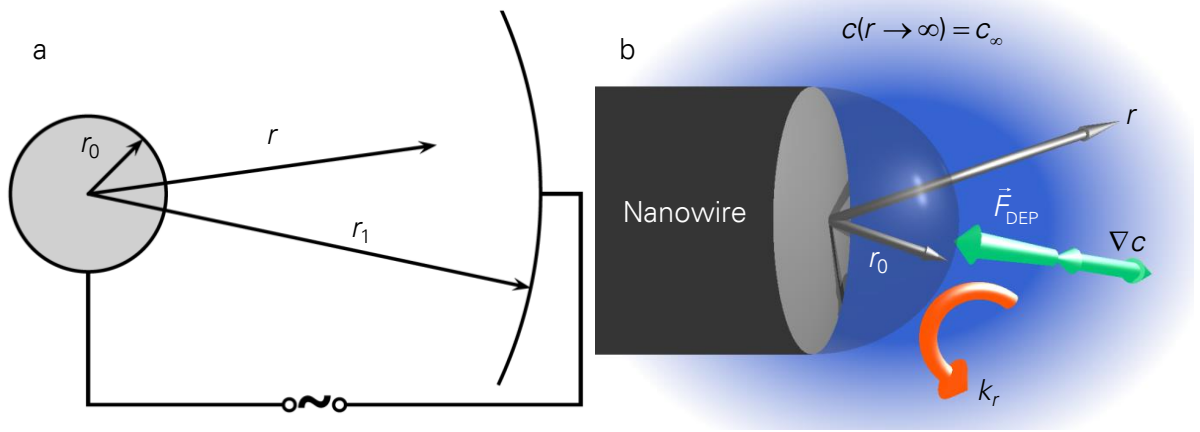


Figure 3-2. Scheme of the convection-diffusion model. (a) The inner electrode is the nanowire tip, the outer electrode is the next metallic object (either electrode or wire). An AC potential is applied to the electrodes. (b) Green arrows indicate the forces on the molecules in solution due to DEP and diffusion (can act towards and away from the tip). The boundary conditions include the reaction rate (red arrow) and the bulk concentration in infinite distance of the tip.

Since the electric field for such small curvatures as a nanowire tip decreases very rapidly, only the vicinity of the nanowire tip is of interest. Here, the field lines follow a radial pattern and in good approximation one can consider the whole problem radial. With the nabla operator in sphere coordinates and the steady-state condition, Equation (3-2) can be rewritten as

$$\text{div } \vec{j} = \frac{1}{r^2} \frac{\partial}{\partial r} \left(r^2 L \left(F_{\text{DEP}} - \frac{\partial \mu}{\partial r} \right) \right) = 0. \quad (3-4)$$

Integration yields

$$A_1 = r^2 L \left(F_{\text{DEP}} - \frac{\partial \mu}{\partial r} \right), \quad (3-5)$$

with A_1 [s^{-1}] being the integration constant with the dimension of the inverse time.

The phenomenological coefficient L can be determined from the 1st Fick law:

$$j = L \frac{\partial \mu}{\partial r} = -L \frac{\partial}{\partial r} \left(k_B T \log \frac{c(r)}{c_\infty} \right) = -L k_B T \frac{1}{c(r)} \frac{\partial c}{\partial r}, \quad (3-6)$$

or

$$j = -D \frac{\partial c}{\partial r}, \quad (3-7)$$

from which follows:

$$L = \frac{D c(r)}{k_B T}. \quad (3-8)$$

The DEP force is calculated with

$$F_{\text{DEP}} = \frac{\alpha}{2} \nabla |E|^2 = \frac{\alpha}{2} \frac{\partial |E_{\text{RMS}}|^2}{\partial r}, \quad (3-9)$$

taking into account the radial nature of the problem.²⁴ Herein, E is the electric field and α is the polarizability of the molecule in solution. For periodic voltages, it is appropriate to use the time-averaged value E_{RMS} of the (radial) electric field distribution. The magnitude of the force depends on the gradient of the electric field energy, because the higher the gradient the higher the difference in acting and counter-acting force F_+ and F_- (see Figure 3-1). For molecules, the polarizability α can be looked up in databases, whereas for nanoclusters, the polarizability is given as

$$\alpha = \frac{1}{2} d_p^3 \pi \epsilon_m K(\omega).^{24} \quad (3-10)$$

$K(\omega)$ is the Clausius-Mossotti factor, which depends on the difference of the absolute permittivities of the medium (solution) and the particle, $\epsilon_m(\omega)$ and $\epsilon_p(\omega)$. It determines, whether the polarization of the object is able to follow the external polarization. If both polarizations are in phase, $K(\omega)$ is 1, meaning that the object moves towards higher field magnitudes ("positive DEP"). At the so-called cross-over frequency ω_c , $K(\omega)$ becomes negative and the object is repelled from the field source ("negative DEP").^{24, 45} The electric field and the polarization are then out of phase. For a sphere, the Clausius-Mossotti factor is

$$K(\omega) = \frac{\epsilon_p(\omega) - \epsilon_m(\omega)}{\epsilon_p(\omega) + 2\epsilon_m(\omega)}. \quad (3-11)$$

For metal, for frequencies up to 10^{15} Hz (which is far above the frequencies used in the experiments of this work), $K(\omega) = 1$.³⁵ The electric field is modeled according to the field distribution in a sphere capacitor

$$E = \frac{V_{\text{RMS}}}{(1/r_0 - 1/r_1)r^2}, \quad (3-12)$$

where the externally applied voltage V_{RMS} is assumed to be the dominant part of the potential between the electrodes. For $r_0 \ll r_1$, which holds true shortly before the nanowires connect, the electric field can be written as

$$E = \frac{V_{\text{RMS}}r_0}{r^2}. \quad (3-13)$$

The electrical energy gradient is then

$$\frac{\partial |E_{\text{RMS}}|^2}{\partial r} = \frac{\partial (V_{\text{RMS}}r_0)^2}{\partial r r^4} = \frac{-4(V_{\text{RMS}}r_0)^2}{r^5}. \quad (3-14)$$

The DEP force can be represented as a product of r -dependent and r -independent functions:

$$F_{\text{DEP}} = \hat{F}_{\text{DEP}} r^{-5}. \quad (3-15)$$

In Equation (3-15), the strong radial dependence is emphasized, resulting in extremely high forces near the nanowire tip (and thus high attraction of polarizable objects) and also a very rapid decrease for large distances, making this force a short-range influence. Inserting the formula for the chemical potential μ from Equations (3-6) and the formula for the phenomenological coefficient L from Equation (3-8) into Equation (3-5), gives an ordinary differential equation of first order:

$$\frac{\partial c}{\partial r} - \frac{\hat{F}_{\text{DEP}}}{k_{\text{B}} T r^5} c = -\frac{A_1}{r^2 D}. \quad (3-16)$$

The model includes the following boundary conditions (see Figure 3-2b):

- the concentration in an infinite distance from the nanowire tip is the bulk concentration c_{∞} . From this, the first boundary condition is

$$c(r \rightarrow \infty) = c_{\infty} \quad (3-17)$$

- the flux at the nanowire tip $j(r=r_0) = j_0$ is equal to the concentration at the nanowire tip $c(r=r_0) = c_0$ times the reaction rate k_r of the deposition at the nanowire tip. The second boundary condition reads

$$j_0 = -k_r c_0. \quad (3-18)$$

The solution for the concentration profile is then

$$c(r) = c_\infty \exp\left(\frac{\hat{F}_{DEP}}{4k_B T r^4}\right) \frac{\int_{r_0}^r \frac{\exp\left(-\frac{\hat{F}_{DEP}}{4k_B T r'^4}\right)}{r'^2} dr' + \frac{D \exp\left(-\frac{\hat{F}_{DEP}}{4k_B T r_0^4}\right)}{r_0^2 k_r}}{\int_{r_0}^\infty \frac{\exp\left(-\frac{\hat{F}_{DEP}}{4k_B T r'^4}\right)}{r'^2} dr' + \frac{D \exp\left(-\frac{\hat{F}_{DEP}}{4k_B T r_0^4}\right)}{r_0^2 k_r}}. \quad (3-19)$$

Further solution details can be found in the Appendix. This formula has three main parts. The exponential term before the fraction represents the DEP force: the lower the value of the radial coordinate r , the higher the electric field gradient and thus the attraction of polarizable objects by the DEP force. The integrals in the fraction describe the diffusion due to a concentration gradient and the terms in the fraction involving the reaction rate k_r account for the deposition reaction taking place at the nanowire tip.

There are two relevant limiting cases.

- For an unlimited reaction rate $k_r \rightarrow \infty$, the terms including k_r in Equation (3-19) vanish. The transport of particles limits the growth process and the concentration profile becomes

$$c(r) = c_\infty \exp\left(\frac{\hat{F}_{DEP}}{4k_B T r^4}\right) \frac{\int_{r_0}^r \frac{\exp\left(-\frac{\hat{F}_{DEP}}{4k_B T r'^4}\right)}{r'^2} dr'}{\int_{r_0}^\infty \frac{\exp\left(-\frac{\hat{F}_{DEP}}{4k_B T r'^4}\right)}{r'^2} dr'}. \quad (3-20)$$

At the tip, depletion of the particles takes place. This is in accordance with the concentration profile for the boundary condition $c(r=r_0)=0$ and corresponds to a diffusion-limited model.

- For a very low reaction rate $k_r \rightarrow 0$, the reaction limits the growth process and the solution for the concentration profile becomes

$$c(r) = c_\infty \exp\left(\frac{\hat{F}_{DEP}}{4k_B T r^4}\right). \quad (3-21)$$

In this case the particles accumulate at the nanowire tip. This is in accordance with the concentration profile which results if the flux vanishes $j=0$. The differential equation then reduces to $0 = L(F_{DEP} - \frac{\partial \mu}{\partial r})$. This corresponds to the reaction-limited case.

The flux density j can be obtained over the integration constant A_1 (cf. Equations (3-4) and (3-5)):

$$j = \frac{A_1}{r^2} = -\frac{1}{r^2} \frac{c_\infty D}{\int_{r_0}^{\infty} \frac{\exp\left(-\frac{\hat{F}_{DEP}}{4k_B T r'^4}\right)}{r'^2} dr' + \frac{D \exp\left(-\frac{\hat{F}_{DEP}}{4k_B T r_0^4}\right)}{r_0^2 k_r}} \quad (3-22)$$

and subsequently the growth velocity v_g , which is an easily measurable quantity (see Chapter 4).

$$v_g = -j_0 V_{Pt}. \quad (3-23)$$

V_{Pt} is the volume of the particle attached to the wire. In case of a cluster, V_{Pt} can simply be calculated from the particle diameter d_p . However, when dealing with molecules, the volume of the molecule in solution is different from the volume of the deposited atom in the wire. In that case, V_{Pt} is calculated from the molar mass and the density of the deposited bulk material. The physical interpretation of Equations (3-22) and (3-23) contains several main statements about the influence of the process parameters:

- The growth velocity is linear with the bulk concentration c_∞ .
- For a high reaction rate, the second term in the denominator of the fraction vanishes and the growth velocity is linear with the diffusion coefficient D (diffusion limitation).
- For a low reaction rate, the integral in the denominator is negligible and the growth velocity is proportional to the reaction rate k_r (reaction limitation).

The second boundary condition in Equation (3-18) is only valid, as long as the concentration at the nanowire tip c_0 is less than the maximum surface concentration c_{\max} . If the reaction rate is not fast enough to reduce all arriving particles in time, particles accumulate at the nanowire tip. If the maximum tip surface coverage is reached (all reaction sites occupied), the flux density at the nanowire tip is not proportional to the concentration anymore but proportional to the maximum concentration at the surface c_{\max} :

$$j_0 = -k_r c_{\max} = \frac{A_1}{r_0^2}. \quad (3-24)$$

This replaces the second boundary condition, whereas the first boundary condition ($c(r \rightarrow \infty) = c_\infty$) remains. Calculating the integration constants as above yields the concentration profile for the case of a maximally covered tip surface ($c_0 > c_{\max}$)

$$c(r) = \exp\left(\frac{\hat{F}_{\text{DEP}}}{4k_B T r^4}\right) \left(c_\infty - \frac{k_r c_{\max} r_0^2}{D} \int_r^\infty \frac{\exp\left(-\frac{\hat{F}_{\text{DEP}}}{4k_B T r'^4}\right)}{r'^2} dr' \right) \quad (3-25)$$

and the growth velocity is

$$v_g = k_r c_{\max} V_{\text{Pt}}. \quad (3-26)$$

This equation shows that from a certain point, the growth velocity cannot increase anymore with the bulk concentration c_∞ , because c_{\max} is a constant depending on the material. If c_{\max} is exceeded by the concentration at the nanowire tip c_0 , every reaction site at the nanowire tip is occupied and an additional increase in either local or bulk concentration could not enhance the speed of the deposition.

In the numerical solution, first the concentration profile according to Equation (3-19) was calculated. If the concentration at the nanowire tip c_0 is higher than the maximum concentration c_{\max} , the concentration profile was replaced by the concentration profile achieved with Equation (3-25).

The nanowire growth kinetics is, as any chemical reaction, temperature-dependent. In Equation (3-25), this concerns the diffusion coefficient D and the reaction rate k_r . The diffusion coefficient D can be calculated from the Stokes-Einstein equation

$$D = \frac{k_B T}{3\pi\eta(T)d_p}, \quad (3-27)$$

where k_B is the Boltzmann constant, T is the temperature, η is the temperature-dependent viscosity of the liquid, and d_p is the particle diameter.⁴⁶ The viscosity η of an aqueous electrolyte solution is that of water, as long as the solution contains predominantly water (down to a fraction of about 90 wt.%), which is a condition well met in the present experiments.⁴⁷ The temperature dependence of the viscosity in turn was fit to the equation $\eta(T) = a_1 \exp\left(\frac{a_2}{T}\right)$ using reported viscosity data.^{48, 49} With the fit parameters $a_1 = 838.8 \text{ nPas}$ and $a_2 = 2045 \text{ K}$, the maximum deviation of the fit from the data is less than 4 % within the considered temperature range from 285 K to 320 K. The particle diameter d_p depends on the size of the polarizable object in solution. The reaction rate k_r is modeled according to an Arrhenius ansatz

$$k_r = \hat{k}_r \exp\left(\frac{-E_A}{k_B T}\right), \quad (3-28)$$

where \hat{k}_r is the reaction rate constant and E_A is the activation energy for the deposition reaction.⁵⁰ These parameters are discussed in Sections 3.1.2 and 4.

3.1.2 Results

The nanowires investigated in this work are grown from a platinum-containing solution. Chapter 4, in which the used substance is Potassium tetrachloroplatinate(II)

(K_2PtCl_4), is mainly dedicated to the experimental investigation of the growth kinetics of such wires. Its dissociation in water is described in Section 3.2. By a special preparation of the solution, one can obtain only the neutral complex $\text{cis}[\text{PtCl}_2(\text{H}_2\text{O})_2]$, from hereon shortly written cis-PtCl_2 , in water. Therefore, the simulation parameters describe the growth of a platinum wire with such substance.

Some of the simulation parameters were drawn from experimental data. In particular, it is worth describing how the reaction rate and the maximum concentration at the nanowire tip c_{max} were determined. Experimental data for the growth velocity over the temperature were fit according to the Equation (4-1) in Subsection 4.2.1, assuming a reaction-limited regime described with Equation (3-26). The activation energy E_{A} for the deposition reaction corresponds to the fit parameter a_3 and is 1.8 eV. The fit parameter a_2 ($2.68 \cdot 10^{22}$ m/s) corresponds to the product of reaction rate constant (see Equation (3-28)), maximum surface concentration and the volume of a platinum atom $\hat{k}_{\text{r}} c_{\text{max}} V_{\text{Pt}}$. The volume V_{Pt} is known to be $1.5 \cdot 10^{-29}$ m³, however for c_{max} only an upper bound can be set, that is $c_{\text{max}} = 1/V_{\text{Pt}} \doteq 110$ M. As it will be seen later in this section and in connection with the experimental results, this upper bound is several orders of magnitude higher than a realistic value. Therefore, the simulations were conducted with $c_{\text{max}} = 10$ μM , which is equal to the bulk concentration c_{∞} . The according pre-exponential factor of the reaction rate is then $\hat{k}_{\text{r}} = 2.96 \cdot 10^{29}$ m/s.

The simulation was performed with a MatLab code using the parameters as in Table 3-1, unless not varied (as indicated in the respective figures).

Table 3-1. Simulation parameters for nanowire growth.

Parameter	Symbol	Value	Reference
Activation energy	E_{A}	1.8 eV	Experiment, <i>cf.</i> Chapter 4
Bulk concentration	c_{∞}	10 μM	Setup
Max. surface concentration	c_{max}	10 μM	Experiment, <i>cf.</i> Chapter 4

Particle diameter	d_p	~ 0.3 nm	Literature ⁵¹
Polarizability	α	10^{-37} Cm ² /V	Literature ³⁰
Temperature	T	298 K	Setup
Tip radius	r_0	30 nm	Experiment, <i>cf.</i> Chapter 4 and 5
Voltage (Peak)	V_p	4 V	Setup
Volume of particle	V_{pt}	$1.5 \cdot 10^{-29}$ m ³	Bulk platinum

The involved integrals in Equations (3-19) and (3-25) cannot be solved analytically – they were solved with a trapezoid approximation with 1000 logarithmically spaced steps. In the numerical solution the second limit ($r \rightarrow \infty$) was set to 0.1 mm, for which the integrals are practically constant (they converge because of the $1/r^2$ in the integrand).

Figure 3-3 shows the calculated nanowire growth velocity versus the temperature for two different tip radii 10 nm (panel a) and 30 nm (panel b). The maximum surface concentration c_{\max} is varied. If the concentration at the nanowire tip surface c_0 does not exceed c_{\max} , the growth process is going towards diffusion limitation, as described by Equation (3-22); complete diffusion limitation would mean a concentration at the tip $c_0 = 0$, described with Equation (3-20). The growth velocity increases with decreasing maximum surface concentration c_{\max} , since the total flux density j is connected to the fit parameter discussed above and the reaction rate increases accordingly. Hence, the total deposition rate increases, raising the growth velocity, too. In case that c_0 is higher than c_{\max} , the growth velocity is described by the exponential dependence in Equations (3-26) and (3-28), which corresponds to reaction limitation. The dashed blue curve corresponding to $c_{\max} = 1$ μ M in Figure 3-3a describes such a case. At a certain temperature (here at ~ 294 K), the reaction rate increased that much, that the concentration at the nanowire tip surface decreased again below c_{\max} and a kink indicates the switching to the diffusion-limited regime. Panel b, displaying the growth velocity versus temperature for a nanowire radius of 10 nm, reveals in principle the same tendencies. Yet, the reaction-limited regime already occurs for $c_{\max} = 10$ μ M. Due to the smaller nanowire tip, the dielectrophoretic force exerted on the metal complexes in solution is higher, causing

a higher concentration at the nanowire tip. The growth velocities in the dashed-line region for $c_{\max} = 1 \mu\text{M}$ and $10 \mu\text{M}$ are not different from each other, since the flux density remains constant due to the fit from the experimental data. However, going to lower c_{\max} , the position of the kink shifts slightly to higher temperatures. High temperature causes a high reaction rate, which is needed to decrease the concentration of the metal complexes at the nanowire surface below the lower maximum surface concentration. Comparing the blue curves in panels a and b, it becomes clear that the kink for a larger tip radius is shifted to a lower temperature and that the growth velocity is lower after $\sim 294 \text{ K}$, that is the kink position in the left diagram. The cause for the shift is that a larger tip exerts a smaller dielectrophoretic force on the metal complexes in solution, thus a lower reaction rate (*i.e.* lower temperature) suffices to decrease the concentration at the tip surface below c_{\max} .

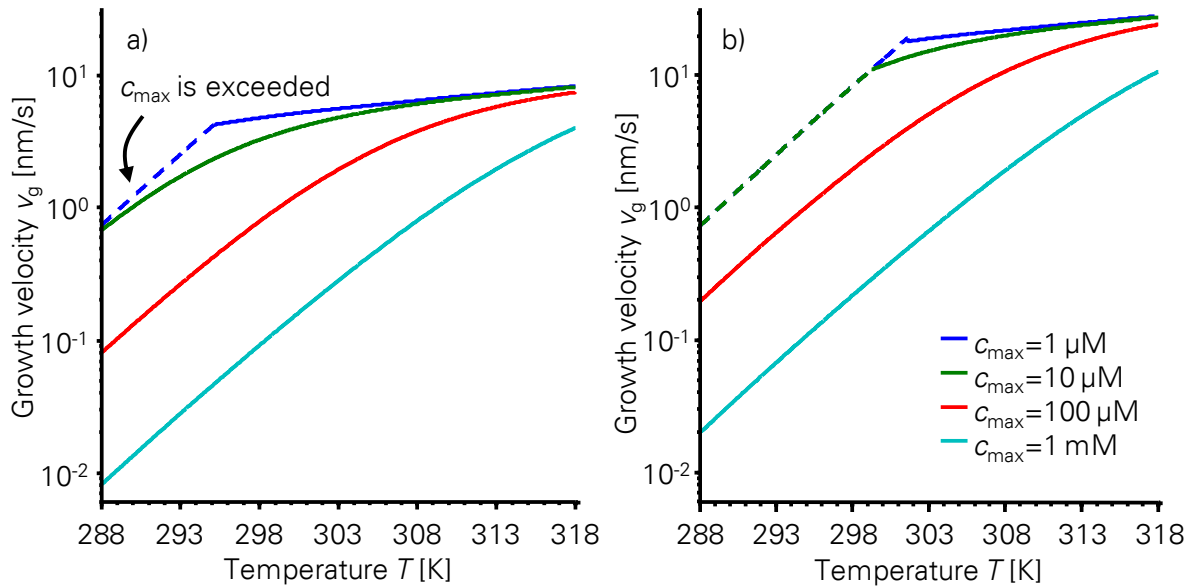


Figure 3-3. Growth velocity of the nanowire dependent on the temperature (semilogarithmic). Decreasing c_{\max} raises the growth velocity. (a) Nanowire tip radius is $r_0 = 30 \text{ nm}$. For $c_{\max} = 1 \mu\text{M}$ at $\sim 294 \text{ K}$ a kink occurs, below which c_{\max} is exceeded at the nanowire tip (dashed line). (b) Nanowire tip radius is $r_0 = 10 \text{ nm}$. The growth velocities are higher than in panel a and the kink occurs already for $c_{\max} = 10 \mu\text{M}$ at a higher temperature than in panel a ($\sim 300 \text{ K}$).

Figure 3-4 shows the radial dependence of the local concentration, relative to the bulk concentration c_∞ . In both panels a and b, the peak-voltage was varied from 2 V to 10 V . Panel a is calculated with a tip radius of 30 nm . The concentration is approximately the bulk concentration at $1 \mu\text{m}$ distance, which is on the order of the

distance between the electrodes. At this distance from the nanowire tip, the problem might not be handled radial anymore. However, the model can still serve as a good estimate. The concentration profile exhibits a decrease towards the nanowire tip. In this case the DEP force on the metal complexes is low compared to the gradient of the chemical potential, which in turn causes depletion at the nanowire tip, going towards the diffusion-limited regime. The region from 10 nm to 1 μm is attributed to diffusion, because all curves, no matter at what voltage, are still joined. At around 10 nm the curves split and each curve ends at a stationary value well below the bulk concentration. This fits to the short-range nature of the DEP force, described in Equation (3-15), its influence only shows in the first 10 nm from the wire tip. The curve distribution is according to expectation, high voltages cause a higher stationary value because of the higher attractive force. The curves are not distributed equidistantly, since the voltage does not enter the concentration profile linearly (cf. Equations (3-19) and (3-25)). An interesting feature is the crossing of the curves at ~ 5 nm, shown in the inset. Low voltage in this case causes a steep gradient and diffusion strives to minimize it. The lower the stationary value at the tip is, the steeper is the concentration gradient and the bulk concentration is reached nearer to the tip.

Panel b on the other hand is calculated with a tip radius of 10 nm, which changes the picture drastically. Since the electric field gradient now is much higher than in the former case (because of the smaller tip curvature), much stronger attractive forces cause accumulation of *cis*-PtCl₂ at the nanowire tip (note the double-logarithmic scale). Again, the distance between the individual curves is not equal, and the curves join at around 20 nm (see inset). Interestingly, the bulk concentration is reached much earlier; a detailed analysis of the single terms in Equation (3-19) shows that in the fraction the term $\int_{r_0}^r \dots dr'$ is much smaller than the term including the reaction rate k_r for $r < 100$ nm. Physically, this means that the concentration gradient has much less influence on the particle flux density than the DEP force. Above 100 nm, the two integrals in the fraction $\int_{r_0}^r \dots dr'$ and $\int_{r_0}^{\infty} \dots dr'$ are approximately equal, making the whole fraction equal to one. At this distance, the influence of the concentration

gradient on the flux density is too low to have a considerable impact on the concentration profile. This corresponds to the reaction limited case described with Equation (3-21): the height of the accumulation is only determined by the electric field and thus by the applied voltage and the distance from the nanowire tip. In fact, there is a small region, where the effect of the concentration gradient is on the order of the DEP force, which can be seen in the inset of panel b. Here, a slight depletion takes place, before the curves reach the bulk concentration. Remarkably, only the blue curve (2 V, respectively) crosses the curves as observed in the inset of Figure 3-4a. This curve exhibits a concentration at the tip surface lower than the bulk concentration, which indicates that the deposition reaction is not limiting, yet. Therefore, diffusion has a similar effect as in the left diagram on the curve progression.

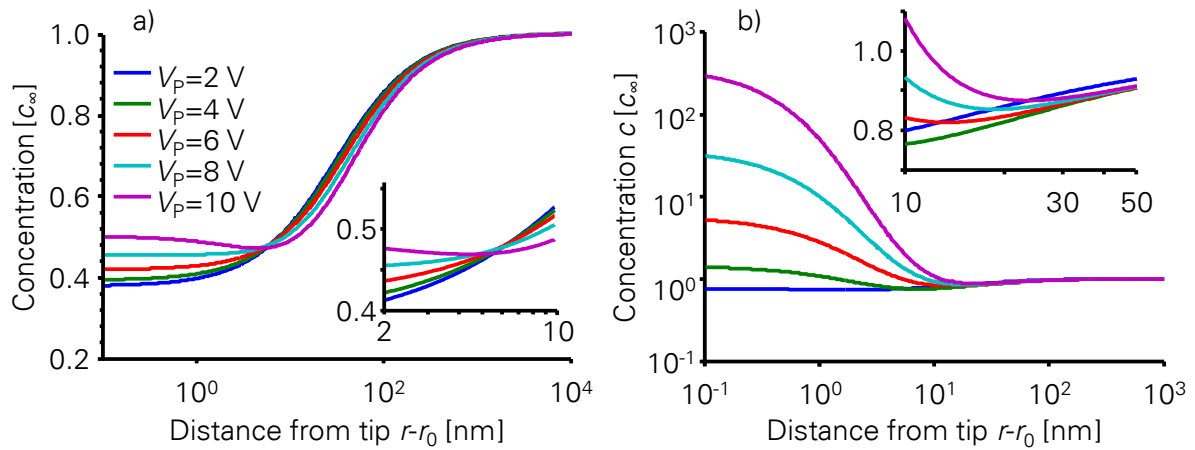


Figure 3-4. Concentration profile of neutral, polarizable molecules (voltage variation) in dependence on distance from the nanowire tip, relative to the bulk concentration c_∞ . The color code is the same for both panels. (a) Variation of applied voltage with tip radius of 30 nm (logarithmic x-axis). (b) Variation of voltage with tip radius of 10 nm (both axes logarithmic), the inset is a detail of the curves.

Theoretically the voltage has little impact on the growth velocity v_g . Once the maximum concentration c_{\max} is exceeded at the tip surface, Equation (3-25) applies for the growth velocity v_g , where the concentration profile does not come into play. If the concentration at the tip surface is lower than c_{\max} , the growth velocity is influenced by the concentration profile. However, the process is diffusion-limited (Equation (3-20) describes the kinetics very well) and the exponential term before the fraction is ~ 1 and thus, only minute changes in the concentration profile are caused

by a variation of the voltage. This is physically plausible, because diffusion is the dominating transport mechanism in a diffusion-limited regime.

Figure 3-5 shows the results for varying the bulk concentration c_∞ and the temperature T . In panel a, the concentration is varied from 10 μM to 10 mM. The y-axis shows the concentration change relative to the bulk concentration c_∞ . For low bulk concentrations, depletion takes place as in Figure 3-4a, corresponding again to the transient from reaction limitation to diffusion limitation. Approaching higher concentrations, the system behavior is not only covered by Equation (3-19), because an increase in the bulk concentration would simply result in the same concentration profile linearly scaled (c_∞ enters the equation linearly). Thus, the above described case distinction using Equation (3-25) is involved. Increasing the bulk concentration then brings the reaction kinetics towards the reaction-limited case. The concentration profile for the two highest bulk concentrations 1 mM and 10 mM nearly overlap, which corresponds to Equation (3-21). As a consequence, it is not possible to increase the accumulation relative to the bulk concentration at the nanowire tip above a certain value, if only the bulk concentration is varied. This is important when determining the radius of the nanowire, as described in Subsection 5.1.1.

In panel b, the dependence of the concentration on the distance from the wire tip and the temperature is plotted. Taking out a single line at 298 K represents the curve for 10 μM in panel a. Going to lower temperatures (*i.e.* lower in the diagram), means that the reaction rate decreases according to Equation (3-28), causing a high gradient of the chemical potential compared to the DEP force and thus leading to the reaction-limited case. Going to higher temperatures (*i.e.* higher in the diagram), corresponds to a higher reaction rate which first weakens the accumulation at the nanowire tip until finally complete depletion at 313 K is reached. This is the diffusion-limited regime, as discussed above.

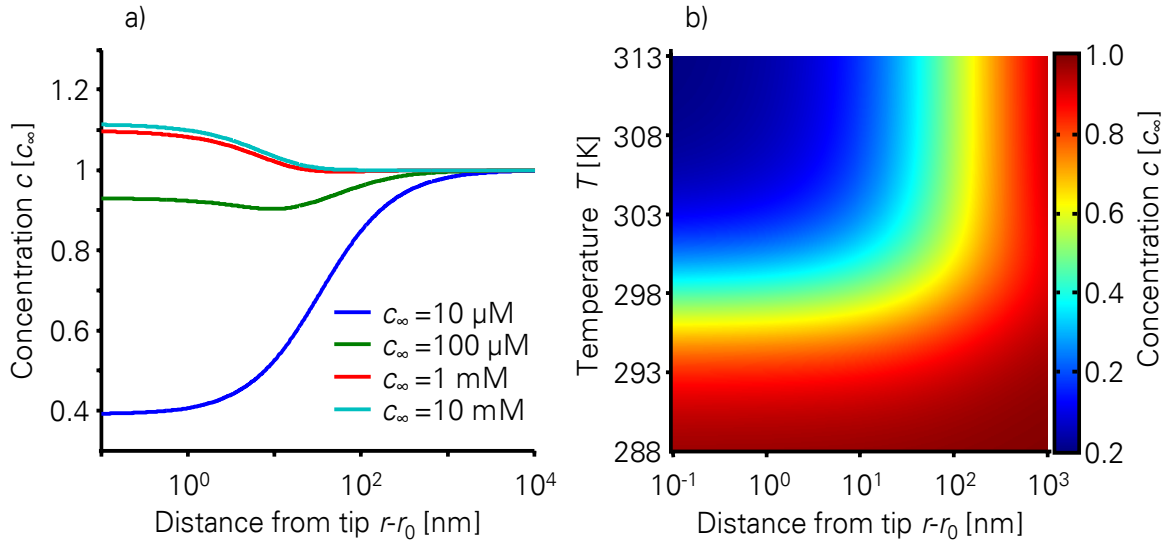


Figure 3-5. Concentration profile of neutral, polarizable molecules (bulk concentration variation) in dependence on distance from the nanowire tip, relative to the bulk concentration c_∞ . (a) Variation of bulk concentration (logarithmic x-axis). (b) Temperature dependence (bulk concentration $10 \mu\text{M}$, logarithmic x-axis).

Due to the simplicity of the model, the results achieved in this section show insufficiencies regarding the quantitative agreement with the experimental data (*cf.* Chapter 4). However, the model provides qualitative guidelines, used to explain results in the upcoming chapters. The analysis in this chapter was conducted for the case of the DEP force. DENA on the other hand deals with charged complexes and the force has to be modeled according to the Coulomb force $\vec{F}_c = q\vec{E}$, which then also changes the sign. Despite differences in the formalism concerning the force, the concept of reaction kinetics applies to both DEP and DENA, as literature shows.^{32, 34} Based on these facts, also the experimental findings using the DENA method in Section 5.1 can be explained.

The model however neglects the influence of charge density caused by periodic ion redistribution on the electric field. This problem takes considerable numerical effort and is part of future research.

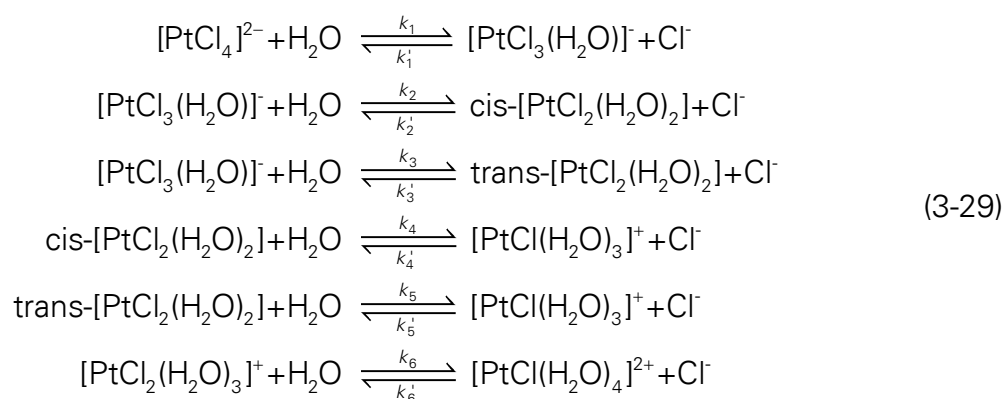
3.2 Dissociation Scheme of K_2PtCl_4

The simulation of this section was done by Markus Pötschke, Chair for Materials Science and Nanotechnology, Dresden.³⁰

As discussed in Section 3.1, the aim is to achieve mainly neutral metal complexes in the aqueous solution. Therefore, this section treats the dissociation scheme of K_2PtCl_4 in water and under what conditions the neutral complex *cis*- $PtCl_2$ occurs most. The hydrolysis of K_2PtCl_4 is strongly pH-sensitive: in acidic solutions, $[PtCl_x(H_2O)_{4-x}]^{2-x}$ species are formed,^{52, 53} whereas in extremely basic solutions $[PtCl_x(OH)_{4-x}]^{2-}$ species are observed.⁵⁴ K_2PtCl_4 solutions with a concentration of 10 μM aged for about 48 h yielded a pH of 8.6. Lower concentrations correspond to lower pH-values. At this intermediate pH, both the OH^- and the H^+ concentration, are much lower than in either reference.

The effective reaction rate to describe the $[PtCl_x(OH)_{4-x}]^{2-}$ route is estimated to be approximately proportional to the OH^- concentration,⁵⁴ as OH^- is actively involved in the reaction. Thereby the effective reaction rate at the pH-value in the present experiments is reduced by the order of 10^5 compared to pH=14.

In contrast, the $[PtCl_x(H_2O)_{4-x}]^{2-x}$ route does not involve H^+ ions, so only minor changes are expected for the reaction rates with changing pH value. Hence, the dissociation model by Elding was adopted,^{52, 53} summarized in Figure 3-6. The chemical equations are given by Equation (3-29).



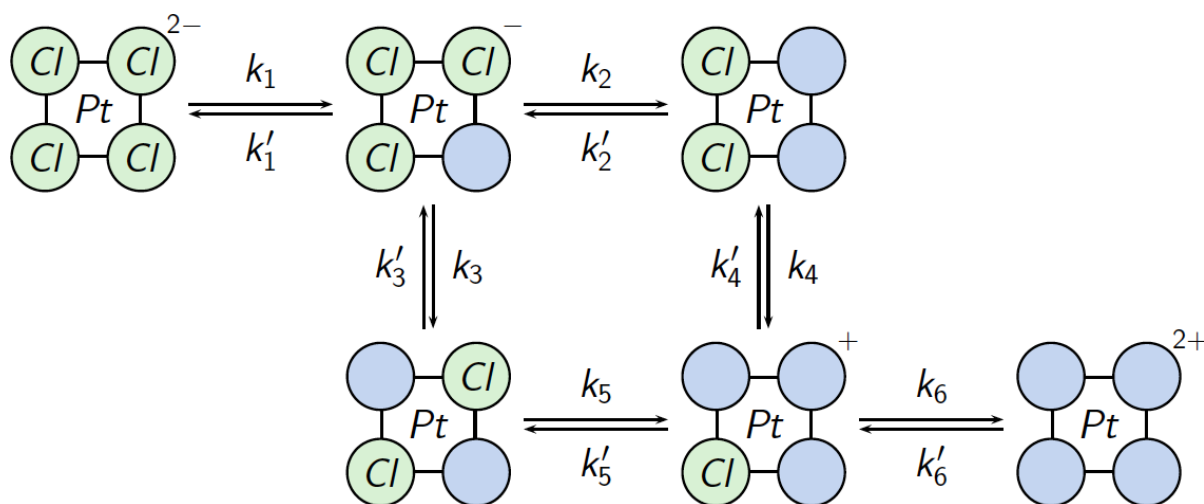


Figure 3-6. Reaction scheme of the dissociation of K_2PtCl_4 in water, according to Elding.^{52, 53} The reaction rates are given in Table 3-2.

The ligand exchange reactions (Equation (3-29)) show first order kinetics and result in the set of differential equations (3-30). The reaction rates k_n for the forward reaction and k'_n for the backward reaction (n is the index of one of the reactions in Equation (3-29)) are given in Table 3-2. The index i of the concentration c_i is the number of chloride ions – in the case of $i = 2$, there are two species, namely the *cis* ($2c$) and *trans* ($2t$) conformation.

Table 3-2. Reaction rates for K_2PtCl_4 hydrolysis at $T = 298$ K.

n	1	2	3	4	5	6
k_n [s^{-1}]	$3.6 \cdot 10^{-5}$	$6 \cdot 10^{-5}$	$2.8 \cdot 10^{-8}$	$3 \cdot 10^{-7}$	$1 \cdot 10^{-4}$	$2.8 \cdot 10^{-7}$
k'_n [$s^{-1}M^{-1}$]	$2.8 \cdot 10^{-3}$	$7.5 \cdot 10^{-2}$	$4.6 \cdot 10^{-5}$	$2 \cdot 10^{-3}$	0.46	$2.66 \cdot 10^{-2}$
reference	52	52	52	52	53	53

$$\begin{aligned}
 c_{Cl} &= c_3 + 2c_{2c} + 2c_{2t} + 3c_1 + 4c_0 \\
 \dot{c}_4 &= -k_1c_4 + k'_1c_3c_{Cl} \\
 \dot{c}_3 &= +k_1c_4 - k'_1c_3c_{Cl} - k_2c_3 + k'_2c_{2c}c_{Cl} - k_3c_3 + k'_3c_{2t}c_{Cl} \\
 \dot{c}_{2c} &= +k_2c_3 - k'_2c_{2c}c_{Cl} - k_4c_{2c} + k'_4c_1c_{Cl} \\
 \dot{c}_{2t} &= +k_3c_3 - k'_3c_{2t}c_{Cl} - k_5c_{2t} + k'_5c_1c_{Cl} \\
 \dot{c}_1 &= +k_4c_{2c} - k'_4c_1c_{Cl} + k_5c_{2t} - k'_5c_1c_{Cl} - k_6c_1 + k'_6c_0c_{Cl} \\
 \dot{c}_0 &= +k_6c_1 - k'_6c_0c_{Cl}
 \end{aligned} \tag{3-30}$$

Figure 3-7 shows the numeric solution of Equation (3-30) using MATLABs *ode45* function. For a $10 \mu M$ K_2PtCl_4 solution, the fraction of *cis*- $PtCl_2$ from 2000 to

3500 min is larger than 92.5 % (green area). In this case, the solution was used as it is. For K_2PtCl_4 concentrations larger than $10\text{ }\mu\text{M}$, the solution contains significant amounts of negatively charged metal complexes which were removed by anion exchangers (see experiments in Chapter 4), to achieve well-defined deposition conditions with only neutral platinum complexes for a DEP process. For any concentration, the first hour is dominated by the PtCl_4^{2-} complex, which gives clear conditions for a DENA process.

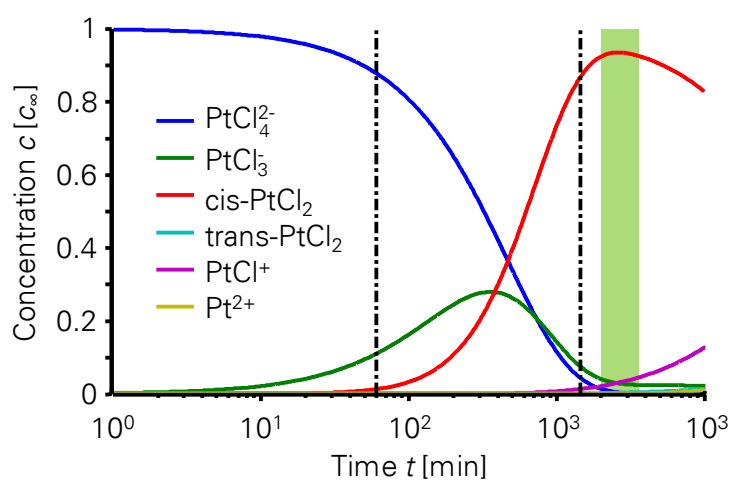


Figure 3-7. Dissociation scheme of $10\text{ }\mu\text{M}$ K_2PtCl_4 in water. The green area highlights the time interval at which mainly neutral metal complexes are present in the solution. The vertical dashed lines mark one hour and one day.

4 Nanowire Growth with DEP

The growth velocity of platinum nanowires in aqueous solution of K_2PtCl_4 is investigated in dependence on the metal complex concentration, substrate temperature and voltage. The solution is specially prepared to provide mainly the neutral complex cis-PtCl_2 (see Section 3.2) for growing nanowires by dielectrophoresis. The resulting cis-PtCl_2 concentration will be denoted c_∞ in this chapter.

The resistance of a typical wire turned out to be on the order of $2.4 \text{ k}\Omega$. Together with the diameter of the wire of 100 nm and its length of $4 \text{ }\mu\text{m}$ this yields a conductivity of 212 kS/m , which is roughly one order of magnitude lower than the bulk conductivity of pure platinum. This difference is attributed to the polycrystalline structure and crystallographic defects of the wire – detailed information on the nanowire crystallinity can be found in Section 5.2. An intense discussion of the electrical behavior of the wire is presented in Section 6.1.

4.1 Characterization of Solution

4.1.1 TEM Investigation of Clusters in Solution

Since the solution is stored 27 h in daylight (see Section 3.2) cluster formation as a consequence of autocatalysis of platinum or due to UV reduction of the platinum complexes is possible.^{55, 56} In order to reveal the presence of platinum nanoclusters, TEM investigations were conducted. For the sample preparation, a $10 \text{ }\mu\text{M}$ solution of K_2PtCl_4 was aged for 27 h in daylight. $1 \text{ }\mu\text{l}$ of the solution was put onto a copper TEM grid, which was plasma-cleaned for 10 s. The solution was then soaked off the grid with a filter paper. Clusters with an average diameter of around 23 nm were found with a narrow diameter-distribution, as shown in Figure 4-1.

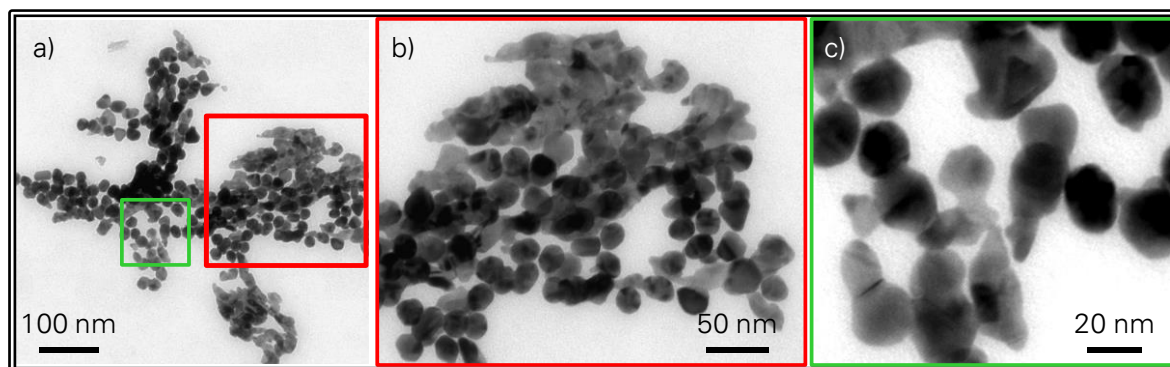


Figure 4-1. TEM images of platinum clusters in a 10 μM K_2PtCl_4 solution aged for 27 h. (a) Overview. (b)+(c) Close-up images of the marked sections in panel a, measured diameter: ca. 23 nm.

4.1.2 Cyclic Voltammetry

To characterize the solution further, cyclic voltammetry was done at room temperature to examine the solution for reducible complexes (see Figure 4-2). The anodic potential at the working electrode was applied first, to check the solution for reducible species. The scan rate was set to 30 mV/s. Two 10 μM K_2PtCl_4 solutions were investigated, one of which was freshly prepared and the other one aged for 27 h in daylight (as in the experiments). At least in the fresh solution one or more peaks were expected to indicate the presence of reducible platinum complexes, according to the already discussed dissociation scheme. However, neither in the aged solution nor in the fresh solution considerable peaks were observed during the anodic phase. This indicates that the solutions were too dilute to measure a significant current from the reduction of the complexes. The aged solution exhibits a higher current/voltage slope, hinting to an increased conductivity of the solution. This can be explained with the larger amount of dissolved chlorine ions in solution, which have a higher mobility than charged platinum complexes due to their smaller size.

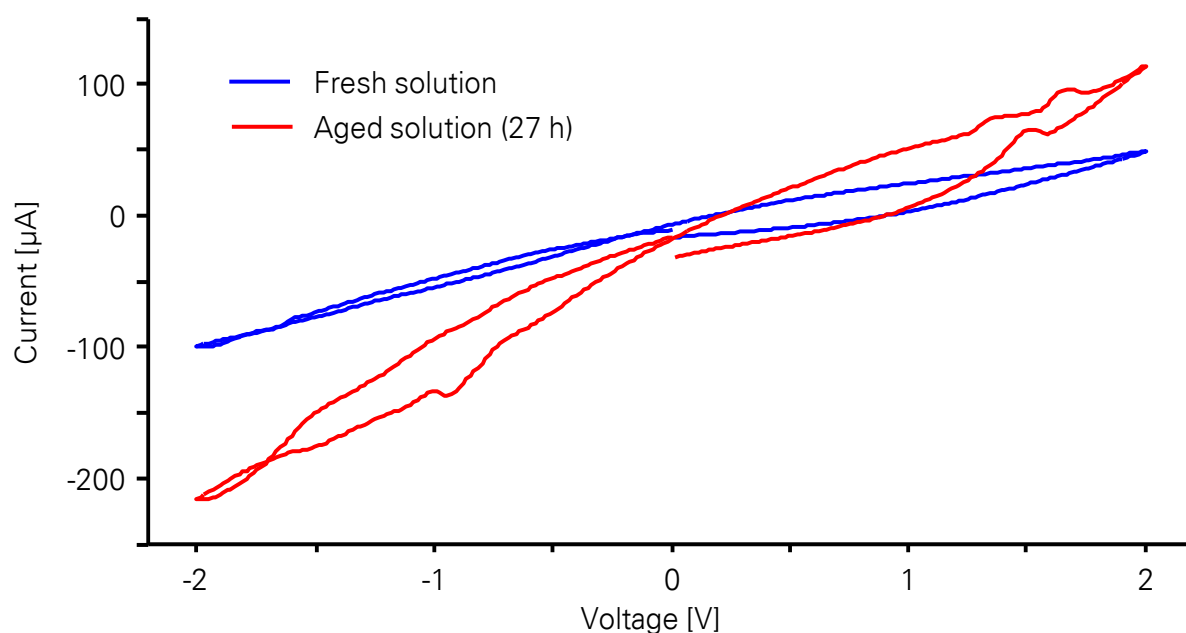


Figure 4-2. Cyclic voltammetry of 10 μM K_2PtCl_4 at room temperature. Scan rate is 30 mV/s. Both fresh and aged solution show nearly Ohmic behavior.

Further experiments offer clues to which extent clusters participate in the wire-forming process. Figure 4-11e in Subsection 4.2.4 reveals nanowires with a constant diameter of 30 nm. The smooth surface of the nanowires indicates that clusters do not participate in the wire forming process, since the diameter of the clusters is on the order of the diameter of the nanowires. Instead, mainly the *cis*- PtCl_2 molecules in the solution are deemed to form the wire. Moreover, the growth velocities are comparable to those from wires grown under different conditions (but with the same solution) shown in Section 4.2. These wires exhibit a rough surface (*cf. e.g.* Figure 4-9) and a higher diameter, which would make cluster incorporation more feasible. If the dominant part of platinum species in the solution were clusters, the “smooth” wires would have grown much slower because much less wire-forming material would have been available. Consequently, the wire-forming species in the solution are mainly molecules.

Although the clusters in the solution apparently do not contribute significantly to the wire growth, they are subject to movement caused by DEP and can thus evoke higher fluid velocities than without their presence.⁵⁷

4.2 Growth Kinetics and Morphology of the Wires

The experiments of this section serve to validate the results achieved in Chapter 3. For this purpose, nanowires were grown between microelectrodes on a glass substrate. The growth velocity of the nanowires was measured under different conditions and compared to the theoretical results. In order to get a statistically relevant amount of data points, an interdigitated electrode design was used (*cf.* Figure 2-1), because at the sides of the fingers many wires grew within one experiment, which could be analyzed during one microscopy session. Each data point in the diagrams in this section represents the average and the standard deviation of at least five individual wires.

For each growth experiment, a 15 μL drop of solution was put on the interdigitated electrodes and an AC voltage $v(t) = V_p \sin(2\pi ft)$ with frequency $f = 100 \text{ kHz}$ and amplitude $V_p = 4 \text{ V}$ was applied, if not stated otherwise. The bulk concentration of *cis*-PtCl₂ in the solution was $c_\infty = 10 \mu\text{M}$ and the temperature of the substrate was $T = 298 \text{ K}$, if not stated otherwise. As a result, the nanowires grew between the fingers of the interdigitated electrodes.

The morphology investigations in this chapter contain observations concerning the wire diameter, as well as for the straightness of the wires. A more detailed discussion is given in Chapter 5. Here, predominantly the nucleation density of wires (number of wires per unit electrode length) and the formation of dendrites (side-branches occurring at the main stem of the wire) are investigated. Dendrites are believed to be a consequence of supersaturation.⁵⁸⁻⁶⁰ Supersaturation, or undercooling, is the difference between the electrochemical potentials $\Delta\tilde{\mu}$ of the liquid and the solid phase. For solidification from liquid, one can achieve supersaturation via three ways.^{61, 62} First, over the temperature difference $T - T_m$, where T is the ambient temperature and T_m the melting temperature of the solid. Second, over the logarithmic concentration ratio $\log(c/c_\infty)$, and third over the difference between the potential $v(\vec{x}, t)$ at the point \vec{x} and the time t and the equilibrium potential V_{eq} : $\Delta\tilde{\mu} = q(V(\vec{x}, t) - V_{\text{eq}})$ for charged molecules/complexes. For

neutral particles, the relevant quantity is the dielectrophoretic (DEP) energy $\alpha/2|E|^2$ (its derivative is the DEP force as in Equation (3-9)). The latter two parameters (concentration and potential) are also included in the formalism in Subsection 3.1.1, since their derivatives with respect to the spatial coordinate r change significantly. An increase in supersaturation also raises the Gibbs free energy of the system, which is energetically not favorable. In order to minimize the Gibbs free energy, crystals form and metal complexes in the liquid phase pass on to the solid phase.⁵⁸ In case of a very high supersaturation, enough energy is left to create more than one single solid/liquid interface, which is the formation of a dendrite. This supports the striving of the system for a rapid decrease in energy, first by creating the surface and second by an additional solid/liquid interface at which metal complexes pass from the liquid to the liquid phase.⁶³ To summarize, it is expected that the higher the supersaturation, the more side-branches occur.

The growth of a nanowire from one electrode to the other one comprises two stages: first, the random deposition of small metal grains at the electrodes which results in a field enhancement and causes a greater DEP force⁶⁴ and, second, the growth of the wire. The first stage will briefly be denoted as nanowire nucleation, characterized by a certain nucleation time t_n . The remaining time is called growth time t_g . In the experiments, the time between switching on the voltage and the sudden increase of current when a nanowire reaches the opposite electrode was measured, or when two nanowires, growing from opposite electrodes, meet each other. From this assembly time $t_a = t_n + t_g$, an apparent nanowire growth velocity $v_g = \ell_{nw} / t_a$ was defined with ℓ_{nw} as length of the nanowires, measured in the SEM. For kinked wires, the traverse along the nanowire was measured.

In the case of microwires, wire growth can be observed by light microscopy. Ranjan *et al.* studied the growth of silver microwires and found that nucleation already occurred within 400 ms.⁶⁴ Since nanowires are hard to observe in situ, the wire growth was interrupted after different periods of time in order to obtain an estimate of the nucleation time. For a growth interrupt after 53 s, $v_g = 12.3 \pm 2.8$ nm/s and for 116 s the similar value $v_g = 11.0 \pm 6.3$ nm/s (temperature 298 K, voltage amplitude

$V_p = 6 \text{ V}$) was measured. Under the assumption of a negligible growth velocity during the nucleation time and a constant growth velocity afterwards,³³ the apparent growth velocity is used to calculate the nucleation time. It was found that the nucleation time is negligible compared to the growth time, $t_n \ll t_g$. Hence, $v_g = \ell_{nw} / t_a$ was used in the data evaluation to determine the growth velocities of the wires.

4.2.1 Temperature Dependence

Figure 4-3 displays the growth velocity of the nanowires in dependence on the substrate temperature. According to the theoretical analysis given in Section 3.1, a linear relationship exists between the wire growth velocity and the diffusion coefficient of platinum complexes in the diffusion-limited case. On the other hand, in the reaction-limited case, the wire growth velocity is proportional to the reaction rate k_r , describing the deposition of platinum complexes at the nanowire tip. The blue-plotted experimental data in Figure 4-3 for temperatures $T > 301 \text{ K}$ (green area) were fitted to the formula $v_g(T) = a_1 D(T)$, where a_1 (707 m^{-1}) is the fit parameter and D is the diffusion coefficient according to Equation (3-27). In the low temperature regime ($T < 301 \text{ K}$, red area), the measured data were fitted according to

$$v_g(T) = a_2 \exp\left(\frac{-a_3}{k_B T}\right), \quad (4-1)$$

where the first fit parameter a_2 ($2.68 \cdot 10^{22} \text{ m/s}$) is equal to the product of reaction rate constant, maximum surface concentration and the volume of a platinum atom $\hat{k}_r c_{\max} V_{\text{Pt}}$ (cf. Equations (3-26) and (3-28)). The second fit parameter a_3 is equal to 1.8 eV (in the range from 289 K to 301 K), which is a reasonable value for the activation energy E_A . The kink at 301 K is the point at which the concentration at the surface of the nanowire tip exceeds the maximum concentration c_{\max} (due to full surface coverage). Mathematically, this corresponds to switching from Equation (3-19) to Equation (3-25) to describe the concentration profile. The simulated data in Figure 4-3 were calculated with the simulation parameters in Table 3-1. The maximum surface concentration at the nanowire tip was chosen to be

$c_{\max} = 10 \mu\text{m}$. It was chosen that low because an analysis of the experimentally measured growth velocity yields that only a small fraction of the available reaction sites at the nanowire tip contribute to the nanowire growth. By way of example, the growth velocity of a wire grown at 100 kHz is $\sim 10 \text{ nm/s}$ and has a diameter of $\sim 60 \text{ nm}$. The available reaction sites at the nanowire tip can be calculated by dividing the area of a half-sphere by $V_{\text{Pt}}^{2/3}$, yielding around 90,000 reaction sites. Taking into account that the wire has a rough surface (as it is shown in Section 5.2), the surface of the nanowire tip is likely to be much larger than simply the area of a half-sphere. Thus, even more reaction sites are available. In one period however, for the given frequency and growth velocity, only around 16 platinum atoms deposit at the wire. It is feasible that a chlorine layer adsorbed at the nanowire prevents the deposition of more metal complexes.

The data in the diagram reveal that experimental data and simulated data in the diffusion-limited region (*i.e.* at $T = 316 \text{ K}$) differ by a factor of ~ 3 . To provide an additional context, the experimental data from Bhatt *et al.* were analyzed, who conducted similar experiments with gold clusters at a much higher concentration.³³ The extracted growth velocities of his microwires are in the range of $0.7 \mu\text{m/s}$ to $7.7 \mu\text{m/s}$ for various voltages and AC frequencies. The theoretically predicted growth velocity according to the diffusion-limited model (which is an upper bound for the growth velocity) for a cluster diameter of 13.5 nm and a concentration of $2.23 \cdot 10^{19} \text{ m}^{-3}$ at $V_p = 44 \text{ V}$ is 2.5 nm/s and thereby a factor of the order 1000 slower than the experimental values. Accounting electrokinetic fluid motion as described in different work by Bhatt *et al.* and also by Gierhart *et al.* could solve this contradiction.^{35, 65} The fluid motion in question is driven by the transfer of momentum from the dielectrophoretically accelerated particles (among them the nanoclusters shown in Subsection 4.1.1) to the surrounding solution, as well as AC electroosmosis due to the presence of K^+ and Cl^- ions, especially at the nanowire tip. Both processes increase the amount of particles transported to the wire tip and thus the growth velocity. Increasing the flux density also introduces the kink seen in the experiments, indicating the transient from reaction limitation to diffusion limitation

(cf. Figure 3-3). The theoretical model would then be very close to the measured values.

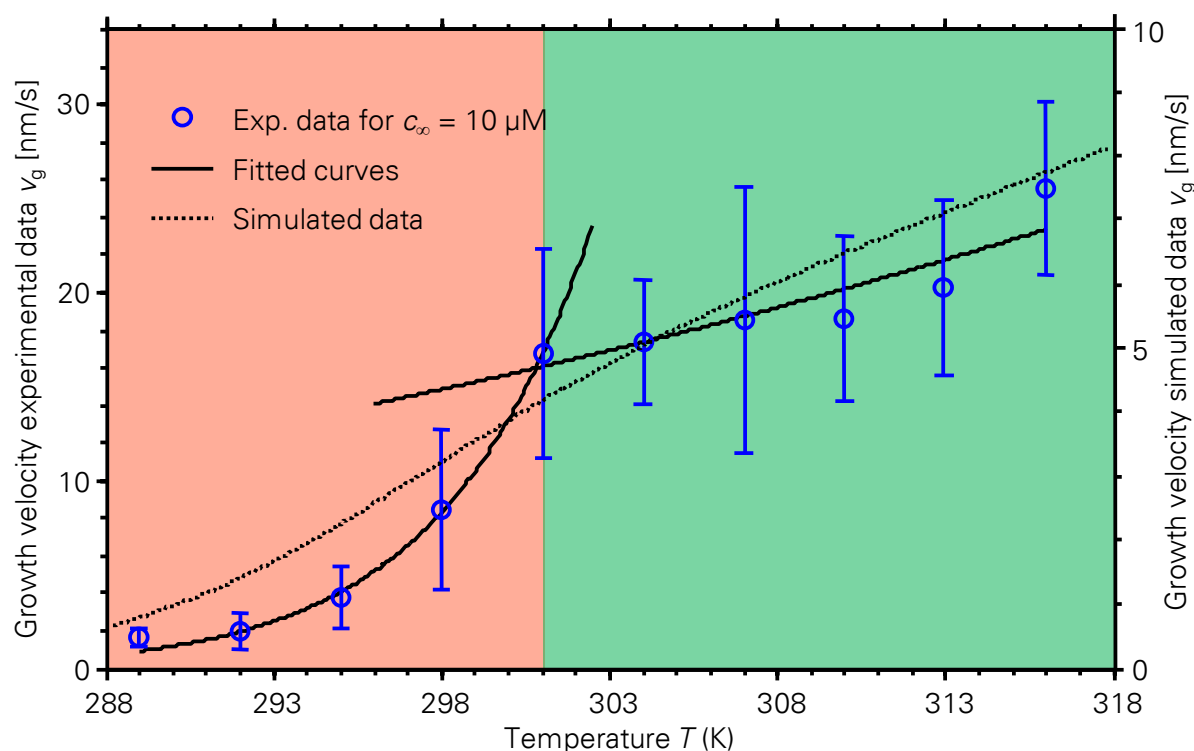


Figure 4-3. Growth velocity of nanowires in dependence on the temperature. Experimental data blue, fit to reaction rate k_r and diffusion coefficient D continuous line, and simulated data dotted line. Red area corresponds to reaction limitation, green area to diffusion limitation.

The measurements shown in Figure 4-3 suggest a change in the rate-limiting process at about 301 K. To explain this temperature behavior, it is proposed that at high temperatures the diffusion of platinum complexes to the nanowire tip is rate-limiting, whereas at low temperatures (<301 K) the deposition reaction of platinum at the tip becomes the rate-limiting process. The deposition process of *cis*-PtCl₂ is not fast enough to deposit all arriving particles immediately. Hence, below 301 K the growth process becomes reaction-limited. The detailed atomistic mechanism of the deposition reaction is presently unknown, but there are several possible mechanisms that might control the deposition rate.

First, a finite tip surface coverage is considered. Each adsorbed *cis*-PtCl₂ covers a certain area of the nanowire tip, limiting the total number of complexes reduced per time. For low temperatures, the *cis*-PtCl₂ reduction rate is smaller and therefore

lowers the growth velocity. The hydration shell of the complexes additionally increases the space consumption. Therefore, the temperature-dependent hydration shell thickness also has an influence on the deposition rate as it was already proposed by Ozturk *et al.*³⁴ Second, adsorption layers on the Pt surface presumably hinder the deposition of Pt, as for example a Cl surface coverage.⁶⁶ Cl desorption, supported by high electric fields, is probably a precondition for further Pt deposition. This could also be one reason why Pt is only deposited at the wire tip, but not along the long wire cylinder surface, in contrast to theory, where growth should occur everywhere along the wire surface. Obviously, there is a certain threshold of the electric field, below which Pt deposition practically does not occur.

Figure 4-4c displays wires grown at 316 K, which do not show any changes to 298 K (panel b) concerning wire density. On the contrary, for low temperatures the nanowire density along the electrodes decreases dramatically; at the electrode in Figure 4-4a, the next nanowire was found over 10 μm apart. The low density is attributed to a lower nucleation rate at lower temperatures. This observation indicates that the initial nanowire formation depends strongly on temperature. Thus, the corresponding activation energies are comparatively high. If Cl adsorption (as discussed above) affects the initial wire formation, then the reported desorption energy of $E_{\text{des}} = 2.4 \text{ eV}$ for Cl desorption from Pt(111) in vacuum supports this suggestion.⁶⁶ The corresponding Arrhenius factor $\exp(-E_{\text{des}}/k_{\text{B}}T)$ changes by more than 3000 from 289 K to 303 K. However, in aqueous environment some modifications should apply. The wires' diameters show fluctuations from 40 nm to 150 nm, but no correlation with the temperature could be found. The number of side-branches does not change considerably with higher temperature, which is in accordance with the low change in supersaturation proportional to $T - T_{\text{m}}$.

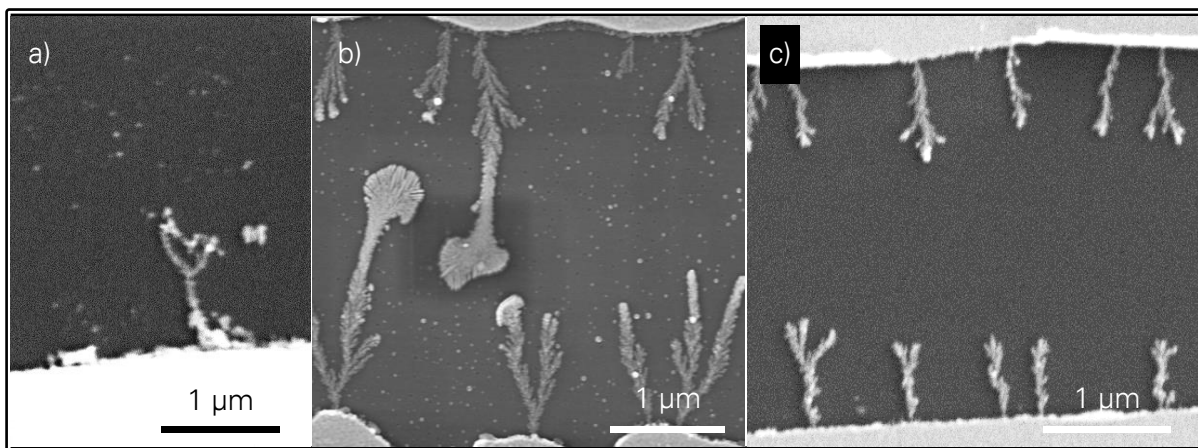


Figure 4-4. Nanowires grown at different substrate temperatures. (a) $T = 289$ K. (b) $T = 298$ K. (c) $T = 316$ K. Low temperatures decrease nucleation density.

4.2.2 Concentration Dependence

As mentioned in Section 3.2, for K_2PtCl_4 concentrations higher than $10\text{ }\mu\text{M}$, it is not possible to achieve predominantly neutral complexes in the solution. Therefore, ion exchangers were used to filter out any charged components. According to the set of differential equations (3-30), the fraction of *cis*- $PtCl_2$ in the solution was determined. The *cis*- $PtCl_2$ concentration resulting from this procedure is denoted c_∞ . Figure 4-5 and Figure 4-6 show the measured growth velocities as a function of the platinum concentration c_∞ at the temperatures 298 K and 316 K. The fit curves reveal a linear relationship for low concentrations at both temperatures. However, at higher concentration ($>88\text{ }\mu\text{M}$), the curve at 298 K exhibits a clear plateau. At first glance it seems that the linear part of the curve in Figure 4-5 corresponds to the diffusion-limited region, and the following plateau to the reaction-limited region. However, Figure 4-3 suggests that the reaction kinetics at $T = 298$ K and $c_\infty = 10\text{ }\mu\text{M}$ is reaction-limited. Additionally, the slopes of the velocity curves v_g were analyzed in Figure 4-5 and Figure 4-6 for low concentrations. In the diffusion-limited regime, the slope depends only on the diffusion coefficient $D(T)$ (cf. Equation (3-22) for high reaction rates k_r). The ratio of the diffusion coefficients is $D(316\text{ K})/D(298\text{ K}) = 1.5$, whereas the observed slopes differ by a factor of 4. This means the growth velocity at 298 K is slower than it would be in a diffusion-limited case. Hence, the reaction must be the slowest step in the process chain, *i.e.* the process is reaction-limited.

Increasing the concentration of K_2PtCl_4 , the concentrations of cis-PtCl_2 as well as of K^+ rise. The rate constant of electron transfer between redox-couples in solution depends strongly on the addition of electrolytes,^{67, 68} which was also shown for reactions at electrodes.⁶⁹ Peter *et al.* observed that for certain cations there is a saturation concentration, above which the reaction rate constant \hat{k}_r does not increase anymore with the concentration of the electrolyte.⁷⁰ To find out whether catalysis by K^+ is relevant in this study, an additional experiment with extra KCl was conducted. At a cis-PtCl_2 concentration of $46\text{ }\mu\text{M}$ (which is in the linear region) further KCl was added to an overall K^+ concentration of $400\text{ }\mu\text{M}$ (red data in Figure 4-5). The resulting nanowire growth velocity of $v_g = 43 \pm 8\text{ nm/s}$ is on the plateau level and shows clearly the catalytic influence of K^+ on the reduction rate. Exceeding a certain cis-PtCl_2 concentration, the K^+ -effect saturates and the deposition rate and thus the nanowire growth velocity do not increase any further.

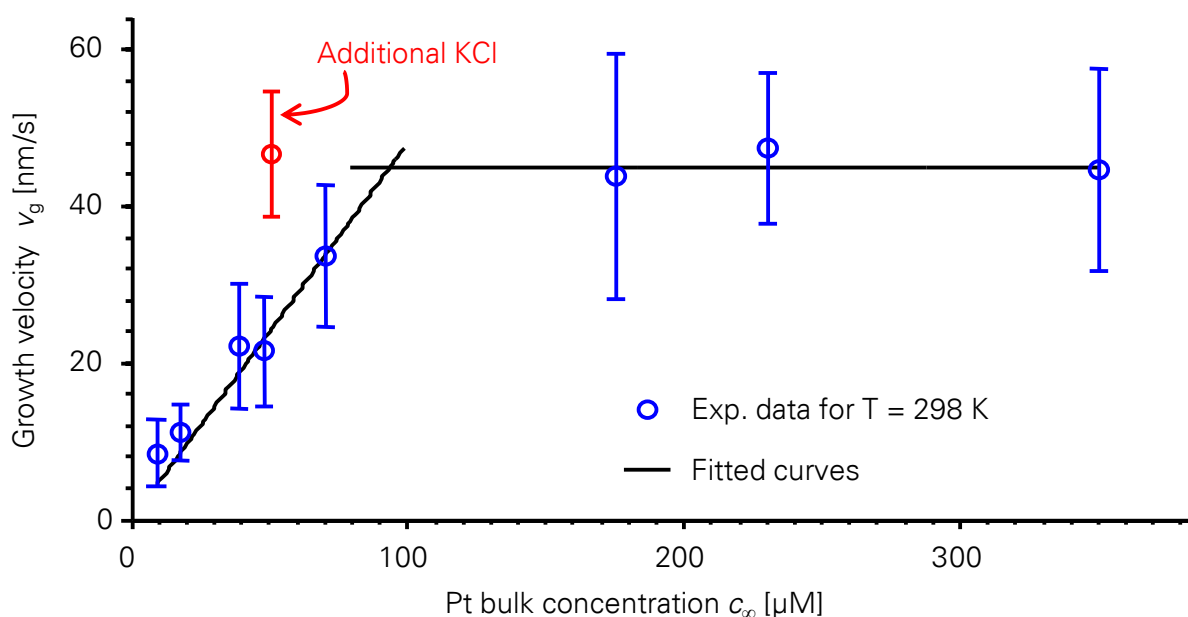


Figure 4-5. Measured nanowire growth velocity as a function of the cis-PtCl_2 concentration at 298 K. The lines are a linear fit through the origin and a fitted constant for above $100\text{ }\mu\text{M}$.

At 316 K and for platinum concentrations above $100\text{ }\mu\text{M}$, the nanowire growth times are in the range of only a few seconds. Kawasaki *et al.* observed nucleation times of approximately 1 s for nanowires grown from an aqueous H_2PtCl_6 solution,³⁹ and Ranjan *et al.* observed nucleation times of $\sim 400\text{ ms}$ for Ag microwires.⁶⁴ Since the nucleation time is already on the order of the growth time, precise measurement of

the growth velocity at both high temperature and high concentration, are impossible in the present geometry of the experiment. In the high temperature and low concentration region, the diffusion of *cis*-PtCl₂ to the nanowire tip is the growth-rate limiting process. In agreement with the theoretical model (*cf.* Equations (3-22) for the flux and Equation (3-23) for the growth velocity), the measured data illustrate that the wire growth velocity is proportional to the *cis*-PtCl₂ concentration and its diffusion constant in water (see Figure 4-6).

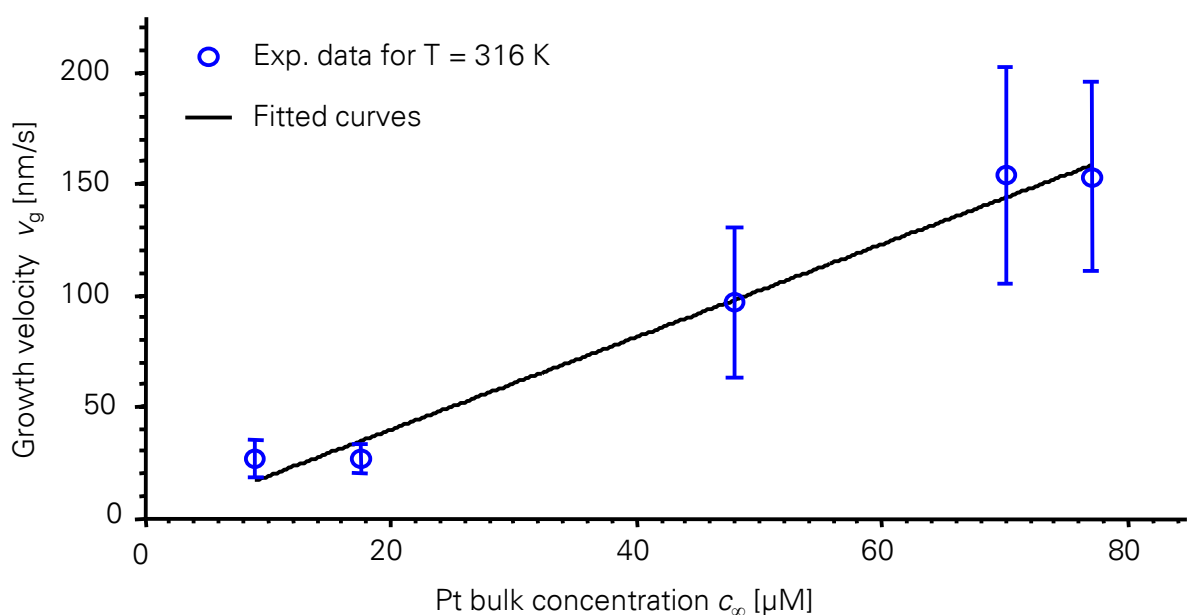


Figure 4-6. Measured nanowire growth velocity as a function of the *cis*-PtCl₂ concentration at 316 K. The line is a linear fit through the coordinate origin.

Increasing the *cis*-PtCl₂ concentration did not change the wire density along the electrode significantly. The diameter shows no considerable changes for low concentrations ($c_{\infty} = 18 \mu\text{M}$ and $c_{\infty} = 178 \mu\text{M}$, see Figure 4-7a and b, respectively), however at higher concentrations ($c_{\infty} = 350 \mu\text{M}$, see panel c) there is a sudden increase of the diameter. This phenomenon is also observed for nanowires grown with directed electrochemical nanowire assembly (DENA), and is attributed to the changing reaction kinetics that will be explained in more detail in Subsection 5.1.1.

The formation of dendrites increases with the concentration (see also Figure 4-10), which can be attributed to the higher supersaturation for higher concentrations. By definition, every branch protruding from the main stem which is twice as long as the

diameter of the main stem, was considered as side-branch. According to this procedure, for every data point the amount of side-branches was counted at four wires and divided by the wire length. A precise measurement is not easy, since it is not always clear which is the main stem of the wire. Despite the missing accuracy of this method, it allows to make a diagnosis of trends. Figure 4-10 suggests that for high concentrations the amount of side-branches per wire length remains constant. This fact appears to be a consequence of the results presented in Figure 3-5. Here, the ratio of the concentration at the nanowire tip to the bulk concentration does not increase anymore beyond a certain bulk concentration. This ratio however, determines the degree of supersaturation (see Equation (3-3)). Since it is not possible to increase this ratio anymore, the supersaturation remains constant and the number of side-branches per wire length, too.

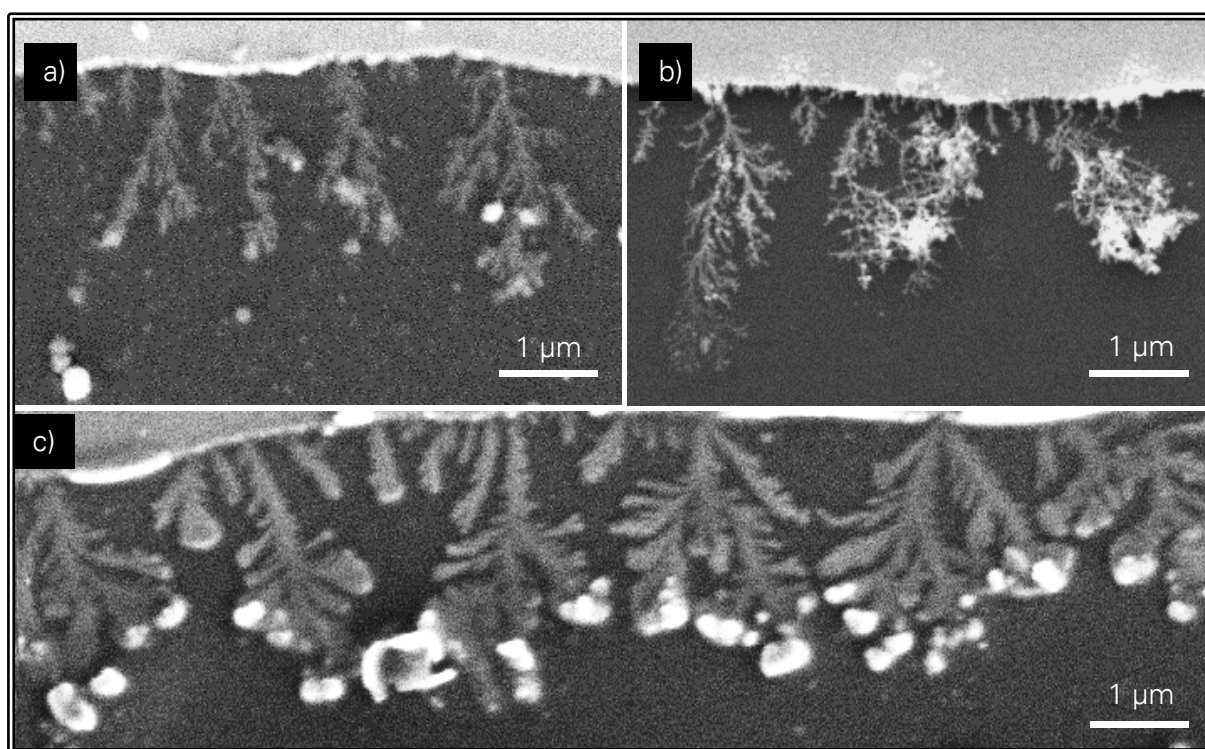


Figure 4-7. SEM-images of wires grown at different *cis*-PtCl₂-concentrations. (a) $c_{\infty} = 18 \mu\text{M}$, (b) $c_{\infty} = 175 \mu\text{M}$ and (c) $c_{\infty} = 350 \mu\text{M}$. The wires in panel c exhibit a higher diameter and more branches per wire length.

4.2.3 Dependence on Applied Voltage Amplitude

According to the model in Section 3.1.2, the applied voltage has little influence on the nanowire growth velocity v_g . Figure 4-8 shows the experimental data for the growth velocity in dependence on the applied peak voltage V_p .

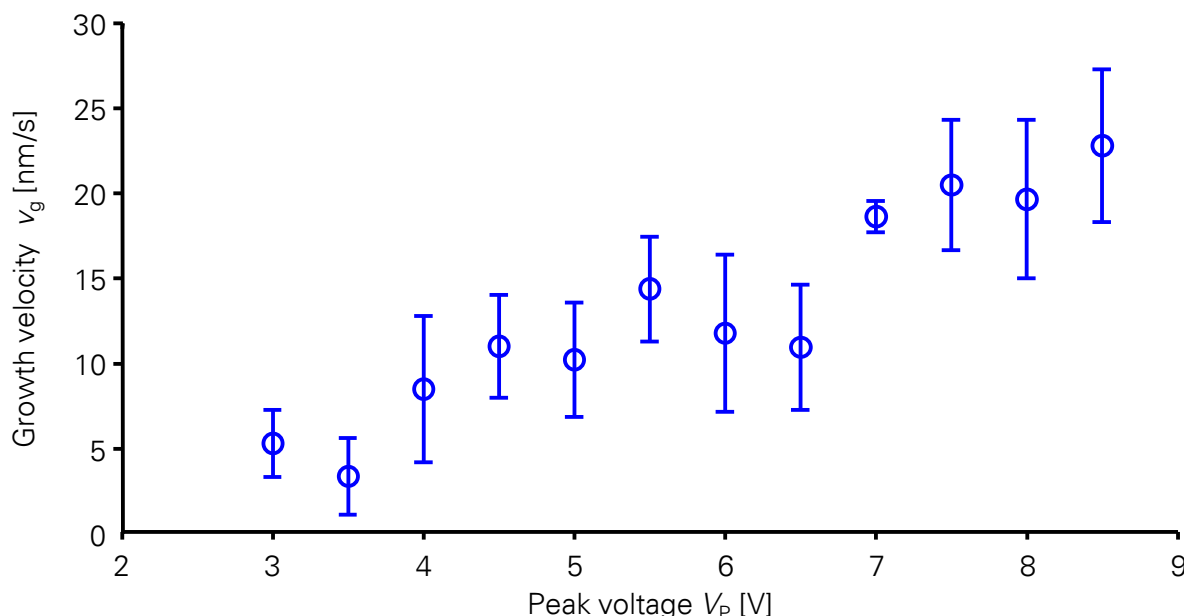


Figure 4-8. Nanowire growth velocity in dependence on the peak voltage.

Several observations can be drawn from the experimental data. First, the voltage has a considerable influence on the growth velocity, in contrast to theoretical predictions. This can be explained with an elevated reaction rate by raising the applied voltage,⁶² which was not incorporated into the model. Plus, with reference to the catalytic influence of the K^+ ions described in Subsection 4.2.2, it is conceivable that the ion flow around the nanowire tip increases with the applied voltage.^{71, 72} Thus, the local concentration of K^+ at the nanowire tip is increased during the negative half-wave when reduction takes place, which in turn can increase the reduction rate. Second, referring to the temperature dependence (Figure 4-3) and the concentration dependence of the growth velocity (see Figure 4-5), the experiments were clearly conducted in the reaction-limited region. That however means that even if the reaction rate would be increased infinitely, the growth velocity must not be higher than in the diffusion-limited case. By following the fit line in Figure 4-3, this upper limit is ~ 15 nm/s (substrate temperature 298 K), which is clearly exceeded at

voltages higher than $V_p = 7\text{ V}$. As proposed already in Subsection 4.2.1, electrokinetic fluid motion may justify this effect. A higher voltage increases the electric field, which in turn increases the fluid velocity. This has an impact on the particle flux density towards the nanowire tip, which accounts for a higher growth velocity.

The SEM-images in Figure 4-9 show wires grown at different voltages and reveal that the morphology of the wires clearly exhibits a higher degree of branching, the higher the applied voltage is. This corresponds to a higher supersaturation at higher voltages.

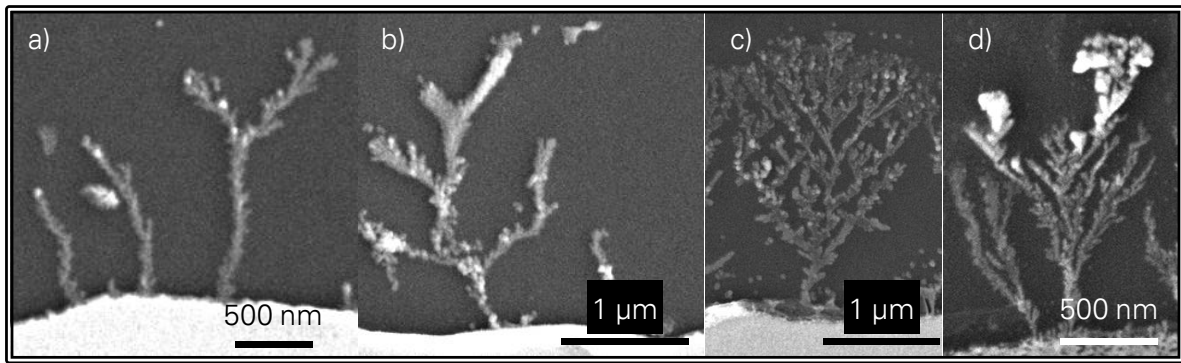


Figure 4-9. Nanowire morphology for different peak voltages applied to the microelectrodes. (a) $V_p = 5\text{ V}$, (b) $V_p = 6\text{ V}$, (c) $V_p = 7\text{ V}$ and (d) $V_p = 8\text{ V}$. The higher the applied voltage, the more branching occurs.

Unlike for the bulk concentration, there is no threshold at which the supersaturation cannot be increased anymore (*cf.* Figure 3-4). Therefore, the number of side-branches also continues to grow, as the measured data in Figure 4-10 suggest. These observations are in accordance with experimental results for both DC-driven crystal growth⁷³ and DENA-grown wires.³⁹ Remarkably, the number of side-branches increases at those locations, where two wires contact each other or a wire contacts the opposing electrode. This is attributed to local electric field enhancement and is discussed in detail in Chapter 5. The nucleation density undergoes a considerable increase from $V_p = 4\text{ V} \dots 8\text{ V}$. It is assumed that a chlorine layer covers the gold microelectrode, which only desorbs under the expense of energy. Potassium is not considered as ad-layer here, since it is not known that potassium is able to adsorb on

noble metal surface, in contrast to chlorine.⁷⁴ This energy can be provided by the applied external voltage, therefore at high voltages the nucleation density increases.

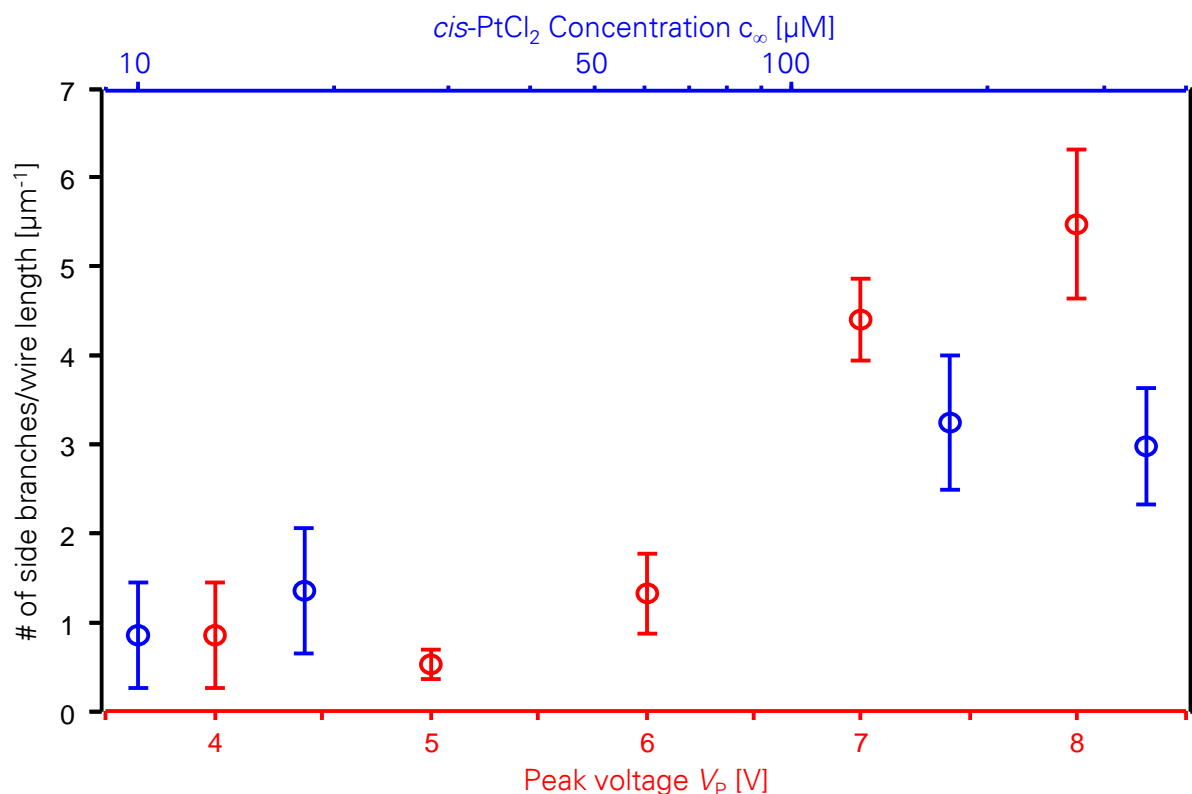


Figure 4-10. Number of side-branches at the nanowires per nanowire length in dependence on the bulk concentration (blue data) and the applied voltage (red data).

4.2.4 Other Signal Variations

This subsection presents results concerning only the morphology of the wires. The parameters varied here were not included into the model in Section 3.1, therefore no quantitative analysis was conducted.

4.2.4.1 Frequency Dependence

Figure 4-11 displays nanowires grown with sine signals at different frequencies from 10 kHz to 10 MHz. Below 10 kHz, the electrodes dissolve due to electrolysis. The morphology of the wires changes drastically.

First, the higher the frequency of the applied voltage, the curlier wires appear. Whereas for 10 kHz (panel a) and 100 kHz (see Figure 4-4b) the wires grow in a comparatively straight manner, the wires grown at frequencies equal to or greater than 1 MHz (*cf.* panel c-e) exhibit curly main and side-branches. This effect can be

based on composition of the solution, containing predominantly neutral complexes. Regardless of the polarity of the applied voltage, those complexes get attracted towards the nanowire surface by the DEP force. Deposition however, only comes about in the negative half-wave. In the positive half-wave, complexes which are already at the nanowire surface can still move along the wire towards the point of the highest electric field energy gradient $\nabla |\vec{E}|^2$, to which the DEP force is proportional. Thus, at low frequencies the complexes are given more time to travel to the nanowire tip (where $\nabla |\vec{E}|^2$ is highest), which results in a more directed growth. At high frequencies, the travel time along the wire might be too short to arrive at the nanowire tip, which leads to deposition at different locations of the wire than its tip.

The second observation concerns the wire diameter, which fluctuates in the same wire for low frequencies, whereas above 1 MHz, the diameter remains constant (*cf.* Figure 4-11e). The maximum measured diameters at 100 kHz are ~150 nm and decrease to ~30 nm at 10 MHz. The theory of dendritic solidification provides the rationale for this technologically important trend and is extensively discussed in Section 5.1.

Third, the nucleation density decreases with increasing frequency, which is attributed to the formation of a chlorine layer at the gold microelectrodes. In the negative half-wave, the chlorine ions are repelled from the electrode. In the positive half-wave, both platinum complexes and chlorine get attracted and the latter adsorbs at the electrode surface. Depending on the duration of the negative half-wave, the chlorine ions travel a certain distance into the solution, while the neutral platinum complexes get reduced and deposit at the electrode surface. If the duration of the negative half-wave is very short (that is, at high frequencies), the chlorine ions travel only a short distance and the chlorine layer at the electrode barely resolves, hindering the nucleation of the nanowires. Accordingly, the applied voltage had to be raised to $V_p = 5$ V, otherwise no growth occurred.

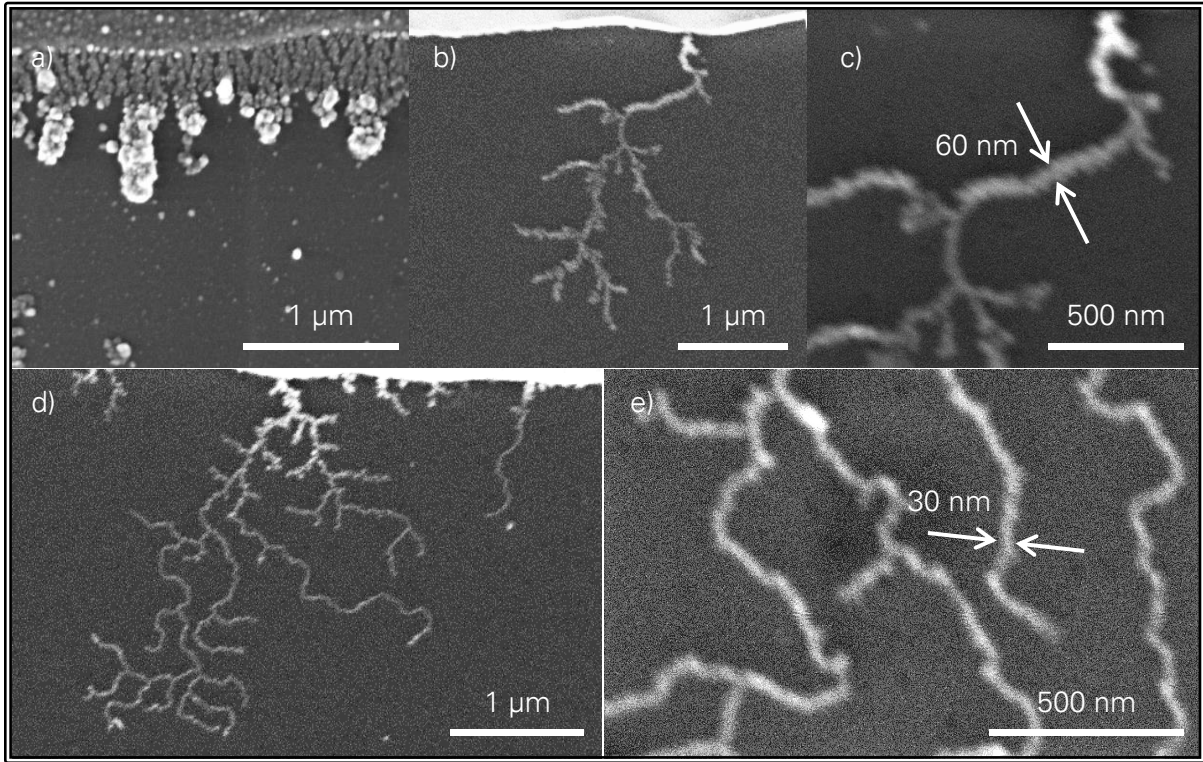


Figure 4-11. Nanowires grown at different frequencies. (a) $f = 10$ kHz, (b)+(c) $f = 1$ MHz, (d)+(e) $f = 10$ MHz. The diameter and the nucleation density decrease with increasing frequency.

4.2.4.2 Offset and Square-Shaped Voltage

Further signal variations include the application of an offset voltage of the form $v(t) = V_o + V_p \sin(2\pi ft)$ (Figure 4-12a and b) and a square-shaped voltage according to

$$v(t) = V_p \left(\sigma(2\pi ft) + 2 \sum_{i=1}^{\infty} (-1)^i \sigma(2\pi f(t - i)) \right), \text{ where } \sigma(t) \text{ is the Heaviside-function (Figure 4-12c and d).}$$

For a peak voltage of $V_p = 5$ V, an offset voltage $V_o = 1$ V was applied. Characteristically, the wires grew only from one electrode to the other (no growth from both sides) and branching was significantly reduced (*cf.* Figure 4-12a and b). Both phenomena are assumed to be caused by the presence of potassium and chlorine in the solution. The growth was initiated at the electrode which was not grounded. According to the equivalent circuit shown in Figure 2-3b, a sine with a positive offset voltage from the function generator results in a sine with a negative offset voltage at the solution. Over the major part of the period a negative potential

is applied to the solution, which causes the electrolyte to behave asymmetric. The electrode which is not grounded attracts potassium for a longer time than the grounded electrode and repels chlorine at the same time. Presumably, this results in a higher accumulation of potassium ions at the non-ground electrode and a low amount of chlorine ions adsorbing to the electrode. At the ground electrode, a dense chlorine ad-layer exists in addition to a little amount of potassium ions. As discussed in Subsection 4.2.1, a chlorine ad-layer on the electrodes hinders the nucleation and in Subsection 4.2.2, it became obvious that potassium ions promote the reduction of metal complexes. This explains why the wires only grow from the non-ground electrode to the ground-electrode. The suppression of the branching occurs due to the higher concentration of potassium ions around the nanowire tip. This leads to a catalytically enhanced deposition rate of platinum complexes at the nanowire tip. Moreover, the lower density of adsorbed chlorine ions reveals more reaction sites. Both helps to reduce the supersaturation considerably. Thus, the Gibb's free energy is not high enough to create a new surface (which would in turn reduce the supersaturation) and no new branch is formed. This physical picture is supported by the observation that branching starts again at $V_0 = 2$ V. Here, the increase in supersaturation caused by the potential increase, surpasses the reduction of supersaturation caused by the increase of the K^+ -ion concentration (the effect saturates at a certain point, *cf.* Subsection 4.2.2). With branches forming again, an optimum range for the offset voltage is provided between 0.5 V and 1.5 V.

Applying a square-shaped voltage with $V_p = 5$ V and a frequency of $f = 1$ MHz to the microelectrodes, produces wires with branching at angles of 45° , as shown in Figure 4-12c and d (the yellow lines are guide to the eye). The parallel occurrence of branches hints to a certain crystallographic order, possibly face-centered cubic, which is common for platinum. This is linked to the rapid voltage increase occurring in a square-shaped wave and Section 5.2 provides a detailed investigation of this behavior using transmission electron microscopy (TEM). However, neither the branches nor the main wires grow completely straight but show curves, indicating defects in the structure of the nanowires.

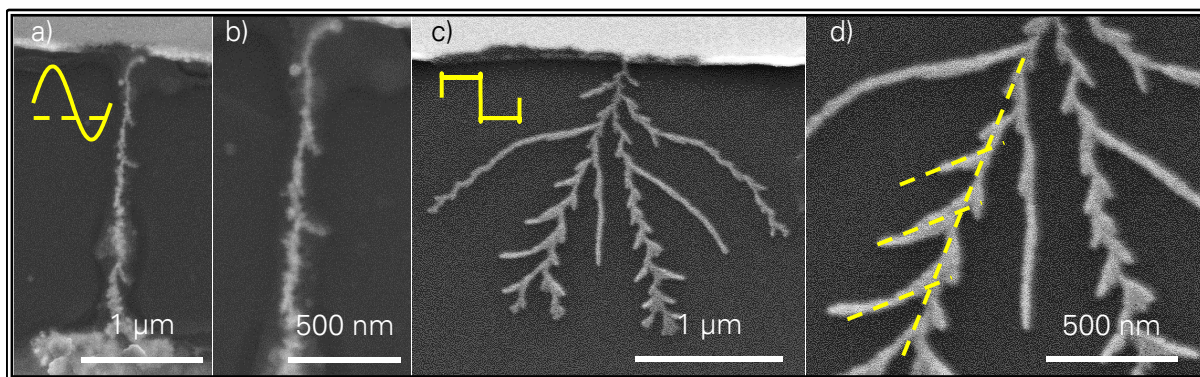


Figure 4-12. Nanowires grown with signals shaped differently than sine. (a) Offset voltage $V_0 = 1$ V. (b) Detail of the wire shown in panel a. Wires grow only from one side. (c) Square voltage. (d) Detail of the wire shown in panel c. Branches occur within an angle of 45° from the main wire (yellow lines are guide to the eye).

In this section the main focus was on the cause of branching, which was found to be closely related to the reaction kinetics of the deposition at the nanowire tip. The following chapter is on reducing the diameter of the wires and on necessary conditions to achieve straight wires.

5 Nanowire Growth with DENA

This chapter treats the nanowire growth from a solution containing charged metal complexes or charged clusters: directed electrochemical nanowire assembly (DENA). Whereas DEP-grown wires are often achieved with a voltage possessing a sine wave form, most DENA experiments rely on the application of a square-shaped alternating (AC) voltage.^{29, 34, 45, 64, 75} The wires are grown from aqueous H_2PtCl_6 solution on a SiO_2 substrate with 300 nm oxide layer or on a Si_3N_4 membrane. Since this chapter in particular addresses the fabrication of straight wires, it is imperative to exclude any influences coming from impurities on the substrate. Thus, $\text{SiO}_2/\text{Si}_3\text{N}_4$ was chosen due to their low surface roughness and the resulting cleanness. The wires are characterized with scanning electron microscopy and transmission electron microscopy (SEM and TEM, respectively).

5.1 Effect of Setup Parameters on Morphology

This section contains a study on the growth of ultrathin, straight and unbranched platinum nanowires with minimum diameter of 15 nm and length in micrometer range. The influence of the concentration of the platinum-containing acid and the frequency of the applied voltage on the diameter of the nanowires is discussed. As pointed out in Section 3.1, the concepts of diffusion limitation and reaction limitation also apply for directed electrochemical nanowire assembly (DENA). On grounds of the theory of dendritic solidification, the analysis in Chapter 3 is able to explain the observations presented in this chapter. A method to contact these straight, ultrathin metal wires is presented, since the conventional method, that is growing from electrode to electrode, is not viable for such wires for reasons discussed in the respective sections. It is further demonstrated that the electric field profile in the vicinity of the growing wires and the shape of the applied voltage dramatically influence the morphology of the nanowires.

5.1.1 Concentration and Frequency Dependence

The growth of the platinum nanowires was carried out following a procedure initially demonstrated by Kawasaki *et al.*¹⁸ However, a dilute 200 μM aqueous solution of

hexachloroplatinic acid (H_2PtCl_6) was employed, which is substantially lower than previously reported concentrations. In the experiments presented here, an electrode geometry where working and counter electrode oppose each other tip-to-tip was used (see more details in Section 2.1). Figure 5-1 displays the scanning electron microscopy images of thin and unbranched wires, which can be reproducibly fabricated applying an AC square-shaped signal to the electrodes in the frequency range between 100 kHz and 1 MHz at $V_{\text{RMS}} = 9$ V. The resulting diameters of the grown Pt nanowires decreased from 60 nm at lower frequencies, down to 15 nm at higher frequencies. This trend is in qualitative agreement with previous works reporting on nanowire growth in an AC electric field.^{34, 39} Ultimately, thin nanowires of about 15 nm in diameter could be obtained by applying a square-shaped AC voltage at 1 MHz, which is a factor of ~ 20 thinner than previously reported values.³⁹

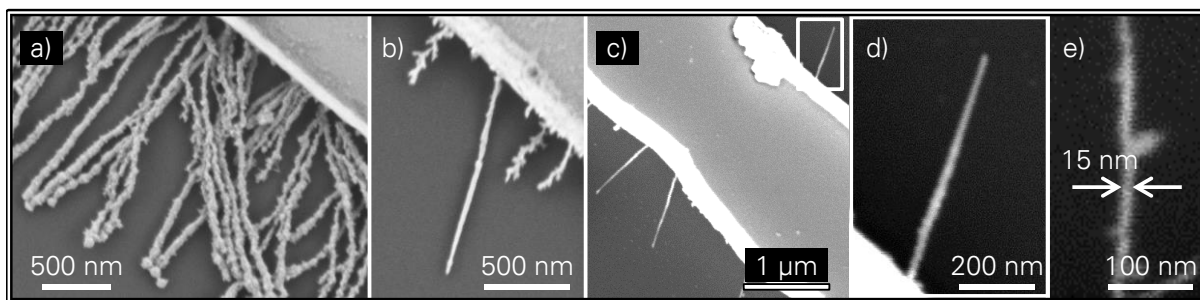


Figure 5-1. SEM-images of Pt nanowires grown from acidic solution at different frequencies with different corresponding diameters: (a) 60 nm at 100 kHz, (b) 30 nm at 300 kHz, (c), (d) 20 nm at 500 kHz (panel d is the magnification of the white square in panel c) and (e) 15 nm at 1 MHz. Growth of the wires starts at lithographical electrodes immersed in solution.

Since low concentrations of hexachloroplatinic acid were used, it is proposed that the mechanism of the nanowire assembly in these experiments undergoes the transition from reaction-limited regime to diffusion-limited regime, as illustrated in Figure 3-5. In dendritic solidification theory, the diameter d_w of the grain, solidified from the liquid, depends on several factors: $d_w = 2\sqrt{2DtSt}$, where D is the diffusion coefficient of the charged particles in solution, St is the Stefan-number (a measure for the degree of undercooling of a liquid), and t is the time of deposition.⁷⁶ The equation can be rewritten as:

$$d_w = \frac{2\sqrt{2DSt}}{\sqrt{f}}, \quad (5-1)$$

where f is the frequency of the applied voltage. Note that with increasing frequency f , the wire diameter d_w decreases, in accordance with the experimental observations. This happens because the platinum deposition only takes place during the negative half-wave of the applied voltage and the solidification front of the wire has only limited time to grow. In the positive half-wave, accumulation of the platinum species around the nanowire takes place. As a consequence, at each beginning of the negative half-wave the same concentration profile around the nanowire tip appears, which results in the same radius of the new solidification front, *i.e.* the nanowire tip.^{76, 77} The diffusion coefficient D can be calculated from the Stokes-

Einstein equation $D = \frac{k_B T}{3\pi\eta d_p}$, where k_B is the Boltzmann constant, T is the

temperature, η is the viscosity of the liquid at room temperature, and d_p is the particle diameter. The diameter of a PtCl_6^{2-} ion including its hydrate shell is $d_p \doteq 0.8 \text{ nm}$.⁵¹ Since the water molecules are much smaller than the dissolved ions, the laws for macroscopic friction may be applied in good approximation.⁷⁸ The viscosity η of water at room temperature can be estimated to be $\eta \doteq 1 \text{ mPas}$, as long as the solution contains predominantly water (down to a fraction of about 90 wt.%), which is a condition well met in DENA experiments.⁴⁷ Inserting these values, one estimates the diffusion coefficient of charged species in solution as $D = 6 \cdot 10^{-10} \text{ m}^2/\text{s}$. The Stefan-number St in turn depends on the bulk concentration of wire-forming species in solution c_∞ , the interfacial concentration of wire-forming species at the liquid interface c_0 , and the partition coefficient k : $St = \frac{1 - c_\infty / c_0}{1 - k}$. The

partition coefficient k represents the ratio of the concentration of wire-forming species at the solid interface to the concentration of wire-forming species at the solute interface c_0 . It is usually constant and can take values between 0 and 1. The ratio of the bulk concentration to the interfacial concentration at the liquid interface $\alpha := c_\infty / c_0$ is strongly dependent on the reaction kinetics of the nanowire growth. In

the case of very high bulk concentrations c_∞ , the reaction at the tip surface is slow compared to the flux of arriving metal complexes, which results in their accumulation at the tip surface (reaction-limited case, see Figure 3-4b). A small value of α results in a high Stefan-number and thus a larger diameter of the nanowires. In contrast, a lower bulk concentrations of the charged species c_∞ decreases the accumulation of the metal complexes, and at a certain point brings α close to 1. This considerably decreases the Stefan-number St , which corresponds to growth kinetics between reaction limitation and diffusion limitation. It is assumed that in the presented experiments c_0 and c_∞ are in the same order of magnitude, which leads to a reduction of the diameter of the assembled nanowires. Figure 5-2 displays measured data of the nanowire diameter versus frequency of the applied AC voltage (red data) grown at a concentration of 200 μM solution of chloroplatinic acid. Each data point represents the average and its standard deviation from six values in total, taken from three different wires grown at the same conditions. The red solid line displays a fit to Equation (5-1), and with the above calculated diffusion coefficient D , a Stefan-number of $St = 0.064$ results. The ratio of the bulk concentration to the interfacial concentration at the liquid interface α is large ($\alpha \rightarrow 1$), which means that the platinum complexes accumulate around the nanowire's tip, just exceeding the bulk concentration. This occurs during the transition from reaction-limitation to diffusion-limitation, as discussed above. This statement is supported by a comparison of the diameters of the nanowires achieved in these experiments with literature data (and also by the DEP experiments in Section 4.2.2).³⁹ The general trend is that wires grown at very low bulk concentrations, are thinner than those grown at high bulk concentrations. However, at high bulk concentrations, no dependence of the nanowire radius on the concentration has been reported.^{29, 33, 34} Obviously, at high bulk concentrations, the ratio $\alpha \rightarrow 0$ and thus the diameter does not change substantially, once the reaction-limited regime is reached. The behavior of the Stefan-number in between these two kinetically different regimes is more complex; the normally constant partition coefficient k can increase at high growth velocities, which in turn increases with the bulk concentration.⁷⁹ This phenomenon requires

further analysis, therefore the dotted blue line in Figure 5-2 is only a guide to the eye, yet appropriate as a qualitative statement.

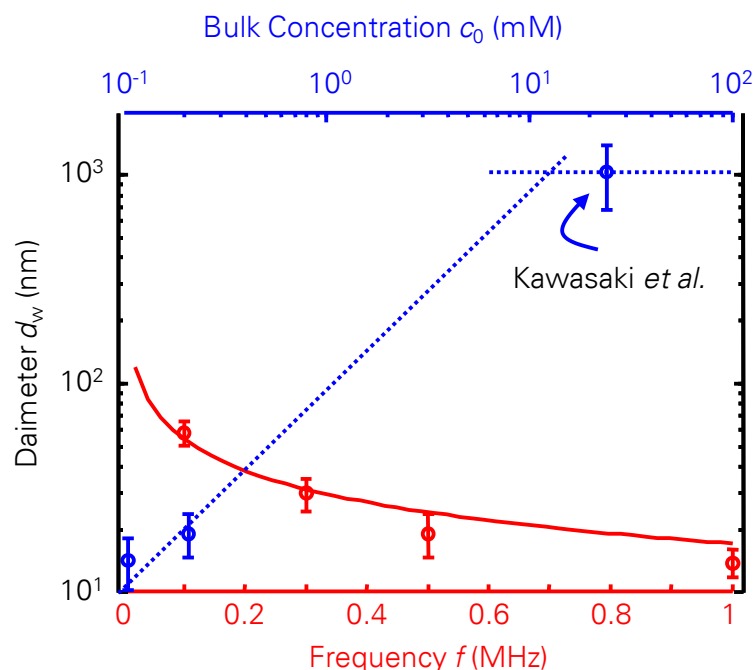


Figure 5-2. Dependence of the nanowire diameter on frequency and concentration. The red solid line is a fit to the measured data and the blue dotted line is a guide to the eye. The data point at 24 mM is taken from Kawasaki *et al.*³⁹

Figure 5-1 shows that thin, straight and unbranched nanowires can be grown at the sides of the electrodes. The side-growth can be activated by control of the nucleation density, *i.e.* the number of wire nucleation centers per unit electrode length, which in turn is influenced by various factors. First, geometrical inhomogeneities of the electrode, at which a high electric field occurs, can facilitate the reduction of metal complexes. Second, the concentration of platinum containing complexes in aqueous solution also changes the nucleation density (*cf.* also Subsection 4.2.2). Finally, an increase of the magnitude of the applied voltage leads to higher nucleation density. Moreover, the applied voltage also has influence on the extent of the nanowire branching (*cf.* Subsection 4.2.3).³⁹ By carefully balancing these three aforementioned parameters, straight wires at the side of the electrodes start to grow. After careful adjustment of the nanowires growth conditions, an optimal peak voltage of 8 V_p-9 V_p at a concentration of 200 μ M was found. To rule

out any influence on straightness and branching coming from either the substrate (e.g. by surface roughness) or the electrode material (different lattice constants at the contact site) the same experiments were conducted for a different substrate (glass instead of SiO_2) and/or a different electrode material (Pt instead of Au), yet, the same results were achieved.

A physical model for the growth of nanowires is presented in Figure 5-3. Since the used solution is acidic ($\text{pH} \sim 3.38$), the majority of the platinum complexes in the solution are PtCl_6^{2-} , $\text{PtCl}_5(\text{H}_2\text{O})^-$ and $\text{PtCl}_5(\text{OH})^{2-}$, which are negatively charged.⁴¹ TEM investigations of the solution revealed no clusters. The growth process in the AC field comprises two phases: in the positive half-wave (*cf.* Figure 5-3a), the negatively charged metal complexes are attracted and accumulate around the tip. In the negative half-wave (see Figure 5-3b), the complexes are repelled and reduced. Reduction only takes place for those complexes which are still in close vicinity to the nanowire tip, when the reduction potential is reached. For a low initial voltage/time slope (increase rate of the voltage at the rising edge of the signal), the complexes are too far off the tip when the reduction potential is reached. For a high slope, the reduction potential is reached when still some complexes are at the tip and reduction takes place. Thus, a high initial voltage/time slope is indispensable for growth.

The described model is in qualitative agreement with previously reported results: growth of the nanowires in an $\text{In}(\text{CH}_3\text{COO})_3$ solution, with an applied sine wave (low initial slope) was only possible at very high voltages ($>20 \text{ V}_p$ @ 1 MHz).⁷⁵ In own experiments again with H_2PtCl_6 no growth was observed applying a sine wave at 500 kHz, but growth was observed at 10 MHz (always at 9 V_p). A high-frequency sine possesses a high initial voltage/time slope, too, therefore nucleation took place. Experiments performed with an applied AC square-shaped signal (high initial slope) resulted in successful nanowire assembly in a wide frequency range (down to 10 kHz).

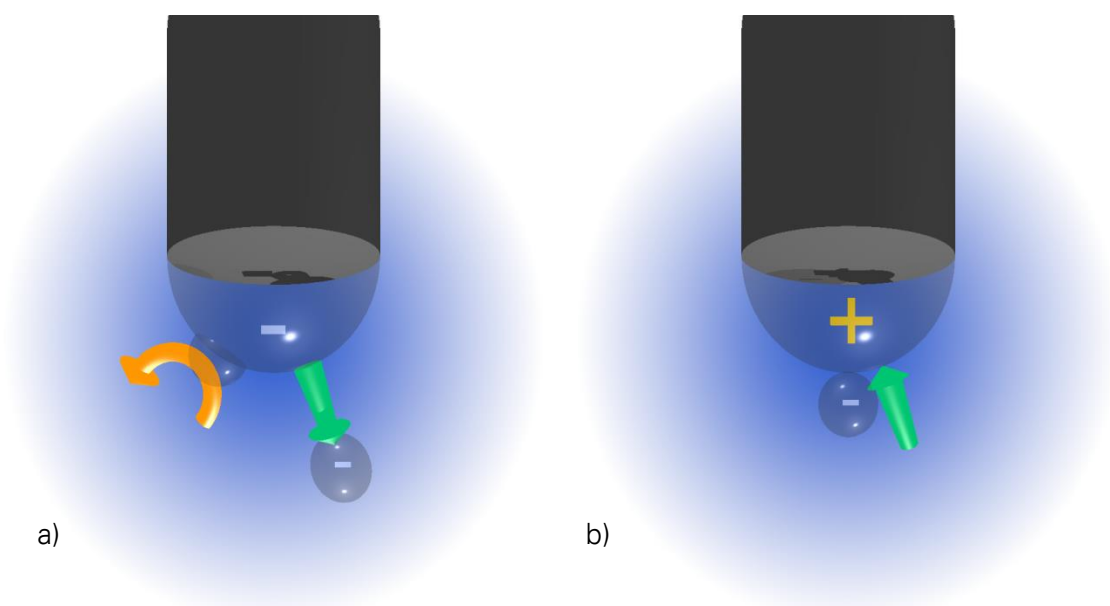


Figure 5-3. Schematics of the nanowire growth process. (a) Attraction of negatively charged metal complexes, (b) repulsion (green arrow) and reduction (orange arrow) of metal complexes. A high potential/time slope is prerequisite to growth.

It is striking that for nanowires grown with dielectrophoresis, a high frequency invokes curls in the nanowire (see Figure 4-11), in contrast to the experiments shown in this section. This difference is attributed to the differently charged metallic objects in the solution. In case of neutral complexes, deposition can take place at any location of the growing wire, since in the positive half-wave the metal species can move along the wire (although the dominant part will still be deposited at the wire tip). This does not apply to charged species; those get repelled at the sides before the reduction potential is reached. Thus, only straight growth occurs.

5.1.2 Electric Field Impact on the Morphology

Connecting the wires to the circuit can be conventionally performed by growing nanowires between the electrodes. However, this process can lead to a number of undesirable effects. First, upon contact the current through the wire suddenly increases and can burn the wire. For thicker wires this could be overcome by monitoring the current through the electrodes and switching off the voltage source upon increase. Second, the wire morphology is strongly dependent on the electric field surrounding the nanowire. Figure 5-4a shows the ground electrode (starting point of the growth) and an electrode with floating potential next to it (floating

electrode). The wires directed into the free space, *i.e.* with no opposing electrode grow straight and without branches. The wires directed towards the floating electrode reveal a more curved geometry. In order to understand the electric field impact on the nanowires' morphology a FEM simulation with COMSOL simulation was performed, solving the 2D-Poisson equation. Figure 5-4b shows the results of a 2D-simulation of the electrode geometry with two wires with 20 nm in diameter and 1 μm in length. The wires emerge from the ground electrode, where one is directed towards the floating electrode and the other one towards free space (as in panel a). Another electrode opposite to the tip of the ground electrode carries a voltage of 10 V (not in the Figure). The full electrode geometry can be seen in Section 2.1 and is the same as in the experiment in panel a. As boundary condition at the edge of the floating electrode served the 2D-Maxwell law for electrical flux $\int_S \rho_s dS = q_0$, where S is the electrode surface, ρ_s the charge density and q_0 the charge of the electrode. The tips of the two wires exhibit the highest electric field. However, the field at the tip of the wire pointing towards the floating electrode is approximately one order of magnitude higher than at the tip of the other wire. This result is interpreted as the consequence of the charge accumulation at the edge of the floating electrode due to the external field. This causes electrical induction and raises the electric field in between the two electrodes. The global field enhancement is reduced when moving the electrodes further away from each other, which leads to straighter wires. Furthermore, the electric field can be decreased by reducing the magnitude of the applied voltage. However, the nucleation density then decreases until no wires grow at the threshold potential, which is different from the reduction potential and explained in more detail by *e.g.* Ranjan or Lumsdon.^{45, 64} In the presented experiments the threshold voltage is at 7 V_p , which is too high to achieve completely straight wire growth for narrow gaps (<1.5 μm).

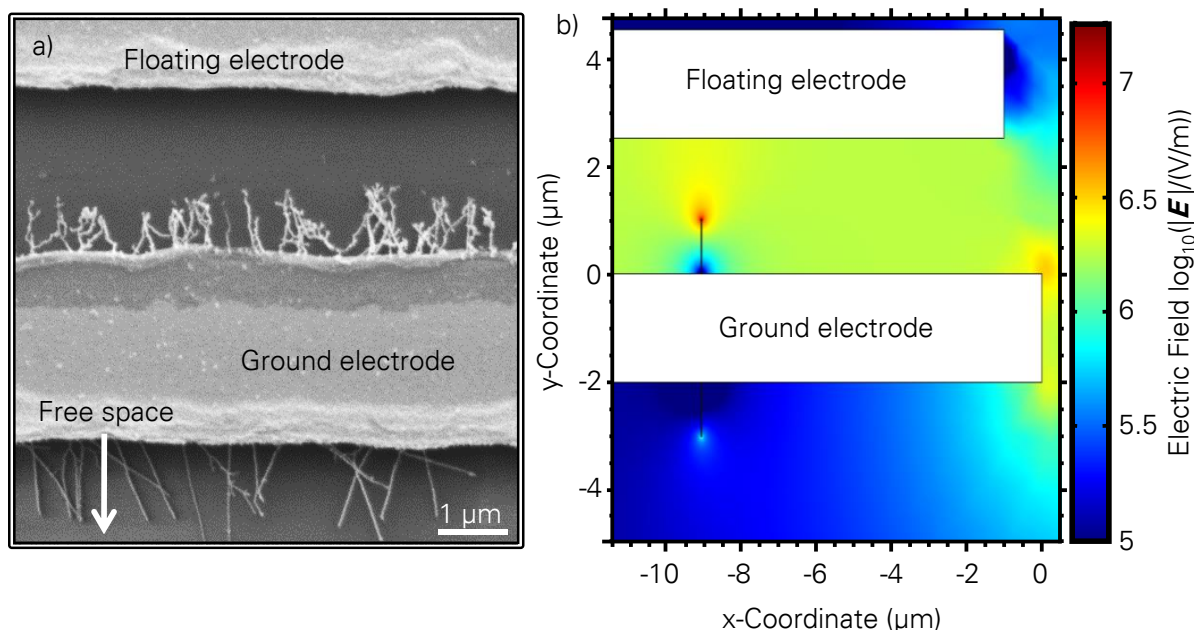


Figure 5-4. Dependence of nanowire morphology on surrounding electric field. (a) Nanowires growing towards free space exhibit straighter growth than when growing towards another electrode. (b) COMSOL simulation of the electric field at the electrode geometry and nanowires of 20 nm thickness. One wire points towards an electrode with floating potential and another one to free space. The potential of the working electrode (not shown here, see Section 2.1 for the design) opposing the ground electrode was set to $V = 10$ V. The different lengths of the electrodes serve to ensure that only side-grown wires contact.

It is important to note that a high electric field does not guide the wire but rather disturbs its deterministic one-dimensional growth. A high electric field causes high supersaturation, since the potential difference from the wire to the platinum species in the solution is the line integral over the electric field, which causes branching on the one hand. On the other hand, as it will be discussed in Subsection 5.2.3, the tunneling of electrons from the wire to the platinum species in the solution is essential for deposition. Global field enhancement as in Figure 5-4b enables tunneling from other parts of the wire than the tip and also subsequent deposition at these sites. Furthermore, the impact of the electric field is found to be crucial for the morphology of ultrathin nanowires, because small curvatures exhibit large electric fields and small defects in the wire structure can disturb the wire's straightness more easily. Such findings were also presented in Subsection 4.2.3, where branching considerably increased at places where a nanowire connects to a second nanowire or the opposing electrode, since at these places a high electric field exists.

5.1.3 Contacting the Nanowires

To contact thin nanowires, like those shown in Figure 5-1, it is desirable to neither melt the wires nor to impede their straightness. Due to the above mentioned issues for thin wires, this cannot be achieved with a simple two-electrode design. This problem can be solved using two-step lithography, as it is illustrated in Figure 5-5.

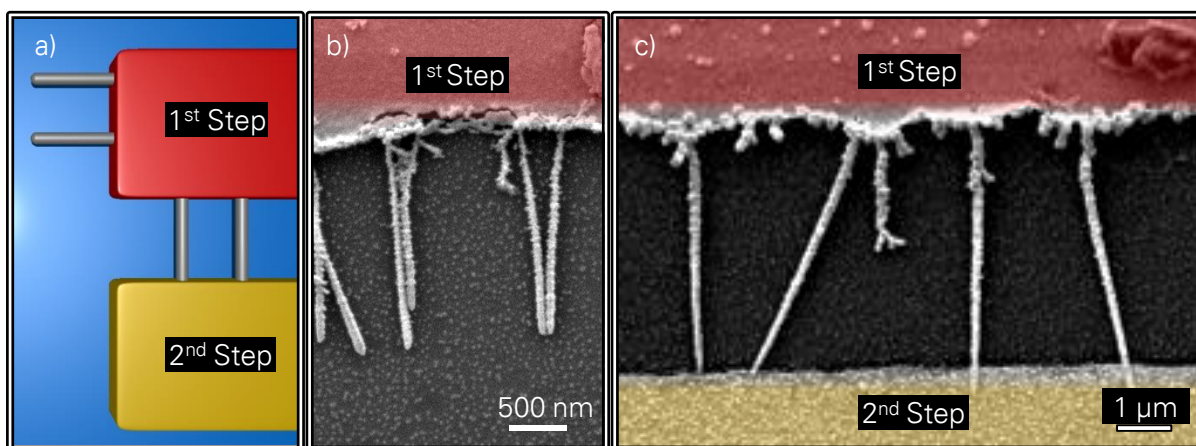


Figure 5-5. Contacting of straight, thin wires. (a) Scheme for contacting ultrathin, straight nanowires. After the first lithography step, the wires are grown at both sides. The second lithography step serves to contact the side-grown wires. (b) SEM-images after the first lithography step. (c) Image of contacted, straight nanowires after second lithography step. Geometrical inhomogeneities in the electrode design were used to initiate wire growth at defined places.

First, nanowires were grown at the sides of two gold electrodes, one of which is ground and the other one carries a potential (see Figure 5-5b). In this case the growth time of the nanowires was about 5 minutes. The length of the wires depends on the growth time and the growth velocity. The latter in turn depends on several parameters, such as metal concentration, concentration of electrolytes, solution age, temperature of the substrate and frequency of the applied signal (see Chapters 3 and 4).³⁴ When the growth process is finished, a second lithography step was performed to contact the nanowires. The alignment was done using a scanning laser lithography setup; however the method can be also applied to UV or e-beam based techniques. Figure 5-5c shows straight wires, contacted by two electrodes. Note that the wires had to undergo the full lithography process again without being damaged, which hints to an enormous mechanical stability. The thickness of the microfabricated gold electrode is 17 nm and hence it lies in the same order of

magnitude as the diameter of the wires. This causes the evaporated gold layer to be locally deformed while covering the wire tips, as shown in Figure 5-5c. Furthermore it is worth noting the curvatures in the edges of the upper electrode. These are geometrical inhomogeneities built into the lithography design. As mentioned above, it is possible to define wire nucleation points with these electrode asperities. Furthermore, voltage amplitude and concentration of chloroplatinic acid have to be chosen accordingly, to optimize the growth process.

5.1.4 Wave Form Variation

The experiments in this subsection were conducted at room temperature with a bulk concentration of 200 μM , applying a constant root-mean-square of the applied AC voltage ($V_{\text{RMS}} = 7 \text{ V}$), and a constant frequency of the signal ($f = 500 \text{ kHz}$). In order to investigate the effect of the wave form of the applied electrical signal on the resulting nanostructures, a truncated Fourier series expansion for a square-shaped signal was applied:

$$v(t) = 2V_{\text{RMS}} \frac{\sum_{i=0}^N \frac{\sin(\omega t(2i+1))}{2i+1}}{\sqrt{\sum_{i=0}^N \frac{2}{(2i+1)^2}}}, \quad (5-2)$$

Herein, N denotes the number of Fourier components, $v(t)$ is the time-dependent voltage, V_{RMS} is the root-mean-square of the voltage, $\omega = 2\pi f$ is the angular frequency, and t is the time.

Figure 5-6 shows a series of scanning electron microscopy images, illustrating the evolution of the morphology of the nanowires as a function of the signal shape of the applied AC voltage. The corresponding insets in Figure 5-6 display the wave forms of the applied electrical signal and their number of Fourier components N . No growth was observed for $N = 1$ (only fundamental frequency), in accordance with results reported by Thapa *et al.*⁷⁵ Observable growth of the wires occurs upon the application of an AC signal consisting of two Fourier components ($N = 2$), as demonstrated in Figure 5-6a. $N = 2$ corresponds to an initial voltage/time slope of $8.3 \cdot 10^7 \text{ V/s}$, which was defined as the increase rate of the voltage at the rising edge

of the signal. Nanostructures with predominantly highly branched morphology were obtained in this case. Increasing the number of Fourier components yields straighter wires, as shown in Figure 5-6b and c for three (initial voltage/time slope: $1.1 \cdot 10^8$ V/s) and five Fourier components ($1.6 \cdot 10^8$ V/s) constituting the signals, respectively. Finally, the application of a square-shaped signal ($3.5 \cdot 10^8$ V/s, device limitation) results in the appearance of straight and unbranched wires (panel d). These observations are supported by analyzing the fractal dimension of the wires grown at different conditions, which decreases from 1.65 for $N = 2$ to 1.24 for $N \rightarrow \infty$ (see Appendix for details).

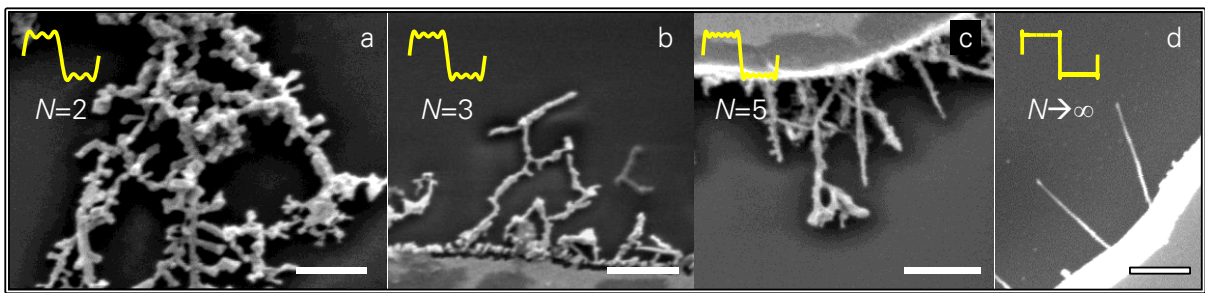


Figure 5-6. SEM-images of the evolution of morphology according to the wave form. The range reaches from (a) dendrites grown with the superposition of two sine waves over (b) wire-like structures grown with the superposition of three sine waves and (c) five sine waves, to (d) completely straight wires with a square-shaped voltage. Scalebars are 500 nm.

In the following, it is shown that such deterministic tunability of the morphology of the platinum nanowires can be attributed to the variable initial voltage/time slope of the applied signal. The root-mean square applied voltage V_{RMS} over the solution was kept constant for all experiments in Figure 5-6 and thus cannot be the cause for the morphology change. A crystallographic analysis using TEM can provide a physical explanation for this phenomenon.

Since the electric field of the opposing electrodes can affect the straightness of the wires (*cf.* Subsection 5.1.2), the TEM investigations were limited to wires growing at the side of the microelectrodes.

5.2 TEM Investigations of Nanowires

Corresponding to the number of Fourier components, the morphology of the nanowires reaches from dendritic patterns to straight wires. The transmission

electro microscopy (TEM) investigations in this section reveal that clusters constitute the wire. Surprisingly, it is observed that corresponding to the number of Fourier components, the orientation of the crystallites constituting the nanowires can be tuned from random to oriented along the [111]-direction. A simple qualitative model, which allows to explain this intriguing observation, is put forth. The electrode fabrication and TEM investigations were done by U. Wiesenhütter, Helmholtz Forschungszentrum Dresden-Rossendorf.

In another TEM investigation, a lamella including a part of the microelectrode and a wire was cut out using a focused ion beam. TEM images could be taken from a cross-section of the electrode. The sample preparation was performed by Y. Ritz, IZFP Dresden. The TEM images were taken by U. Mühle, IZFP Dresden.

5.2.1 Presence of Clusters in Platinum Nanowires

For the TEM investigations, the nanowires were directly grown at electrodes on a 50 nm thin Si_3Ni_4 membrane (see Section 2.1 for further details). These substrates could be directly investigated using TEM without intermediate preparation steps, which might cause damage to the wires. Figure 5-7 displays the morphology of the nanowires in more detail. A wire grown with an applied AC signal with two Fourier components ($N = 2$, see panel a) reveals directed growth, is clearly dendritic and has a large diameter of up to 100 nm. However, applying a square-shaped AC potential to the electrode, straight and unbranched wires with a diameter of around 20 nm formed (Figure 5-7b). The straight and unbranched morphology of the wires grown with a square-shaped signal would suggest monocrystallinity. In addition, Kawasaki *et al.* reported on the appearance of side-wires branching off in crystallographic directions in similar experiments, hinting to a global crystallographic order.³⁹ However, as one can see in the TEM-image in panel c (zoom of panel b), the wire does not consist of a coherent bulk material, but is polycrystalline and represents a pattern containing closely packed clusters with diameters around 2-5 nm. Note that the acidic solution at this concentration consists only of the negatively charged platinum complexes PtCl_6^{2-} , $\text{PtCl}_5(\text{H}_2\text{O})^-$ and $\text{PtCl}_5(\text{OH})^{2-}$.⁴¹ Various cluster-forming mechanisms for aqueous platinum solutions have been reported.

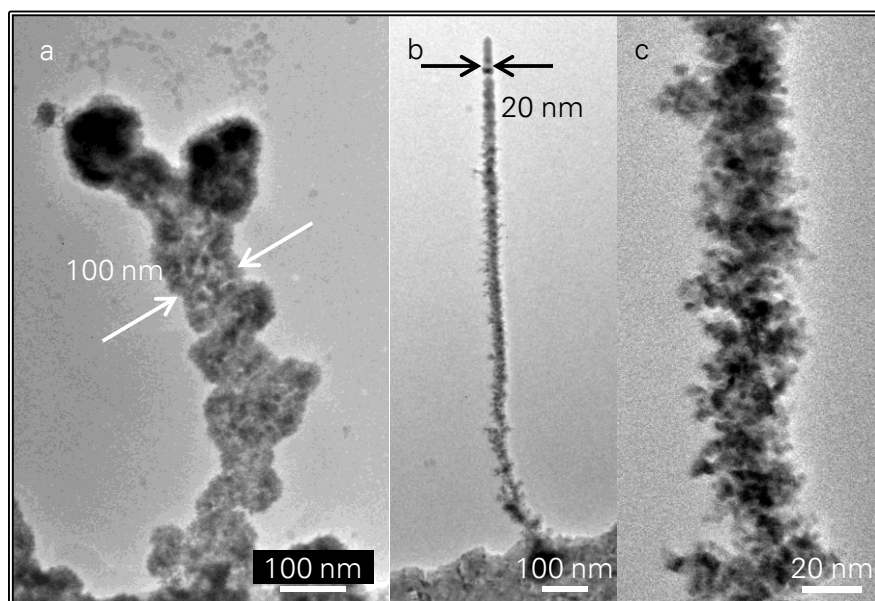


Figure 5-7. TEM image of Pt nanowires grown at the sides of the gold microelectrodes. (a) Dendritic wire grown with number of Fourier components $N = 2$. (b) Straight wire grown with square-shaped voltage. (c) A detail of the wire grown in panel b.

First, hydrogen produced by hydrolysis at the electrodes can lead to reduction of the metal complexes in the aqueous H_2PtCl_6 solution and subsequent cluster formation.⁵⁵ Second, a UV-induced cluster formation process in aqueous H_2PtCl_6 solution is also feasible (see also Subsection 4.1.1).^{55, 80} Third, an auto-catalyzing cluster formation process for aqueous K_2PtCl_4 solutions can take place in the presence of an electron donor starting the reaction.⁵⁶ Here, the electrons could be provided by tunneling from the electrode tip. Last, ballistic deposition of metal complexes is also known to form voids and cluster-like structures in aqueous solution.⁸¹

5.2.2 Lattice Orientation of the Clusters in the Nanowire

In order to investigate the crystalline structure of the grown nanowires, the orientation of the platinum nanoclusters within the wire was analyzed and the Fourier transform of the obtained TEM images was conducted. Figure 5-8 displays a close-up image of the wire in Figure 5-7a, which was grown applying a signal consisting of two Fourier components ($N = 2$). The crystalline orientations of the platinum nanoclusters were investigated in different locations of the nanowires.

Figure 5-8c-e displays the (111)-lattice planes of the nanoclusters. Obviously, the orientation of the planes of the nanoclusters remains only locally constant and can differ after a few nanometers within the wire. In Figure 5-8b the Fourier transform (FT) of panel a exhibits a nearly ring-like structure. The reflections can be assigned to the (111)-lattice planes of platinum, which have a lattice spacing of $d_{111} = 0.226$ nm. The ring-sections indicate that the wire is polycrystalline, confirming the different orientations of the (111)-lattice planes found in the high resolution images. The inset in panel a is a scheme of platinum clusters, sketched by way of example for an octahedron, since platinum clusters can have many shapes.⁸² Their faces do not touch each other, which is a plausible configuration for a wire consisting of multiply oriented clusters.

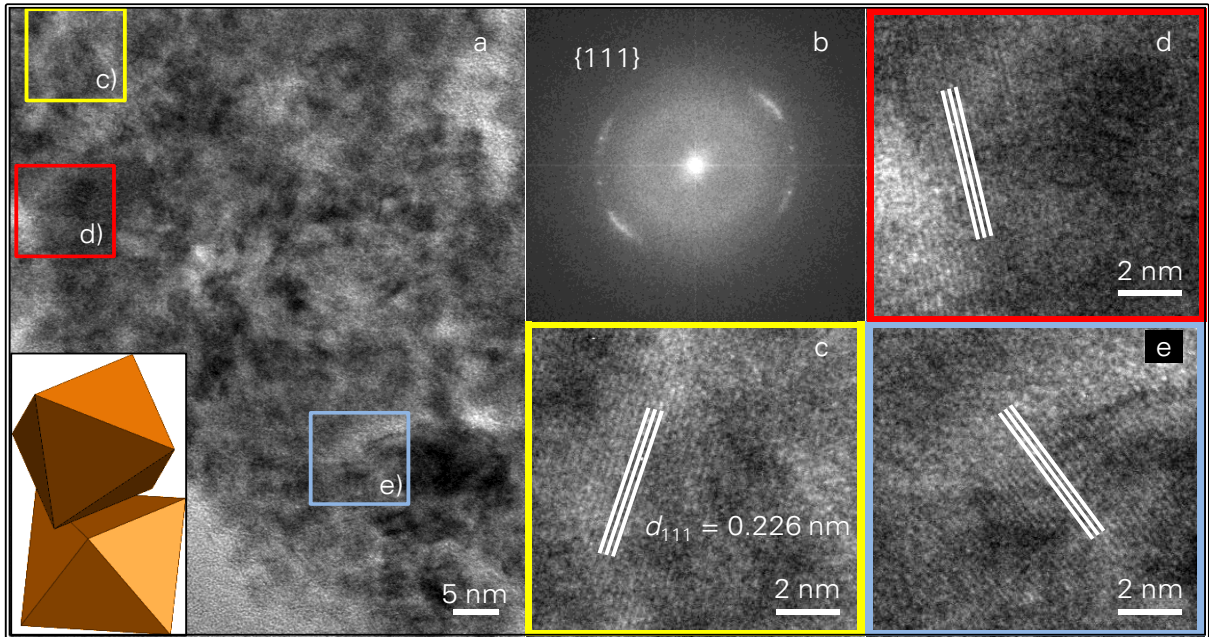


Figure 5-8. Investigation of clusters of the wire in Figure 5-7a. (a) Detailed TEM image. The rectangular sections represent the detail images in panels c-e. The inset shows misaligned octahedrons as example for the orientation of clusters in the wire. (b) The FT of panel a shows ring sections, indicating polycrystallinity of the wire and a random orientation of the clusters incorporated in the wire. (c-e) (111)-lattice planes of the nanoclusters from the sections in panel a. White stripes are guide to the eye. The orientation of the planes differs immensely (angle between (111)-crystal planes in panels c and e: 52°).

Detailed images of the wire in Figure 5-7b and c are depicted in Figure 5-9. In contrast to the wire investigated in Figure 5-8 equal orientations of the planes were found all over the wire, except for small deviations (e.g. compare panel c and e: 5°).

In this case, the FT of panel a shown in panel b reveals two spots in the axial coordinate of the wire. Due to the minor differences in the orientation of the (111)-lattice planes, these spots are slightly smeared. The reflections can again be attributed to the (111)-lattice planes, suggesting a common orientation of all clusters. In panels c-e sections of the wire in panel a are presented, where the (111)-lattice planes are shown in more detail. The inset in panel a suggests a configuration of octahedrons, which are stacked face-to-face.

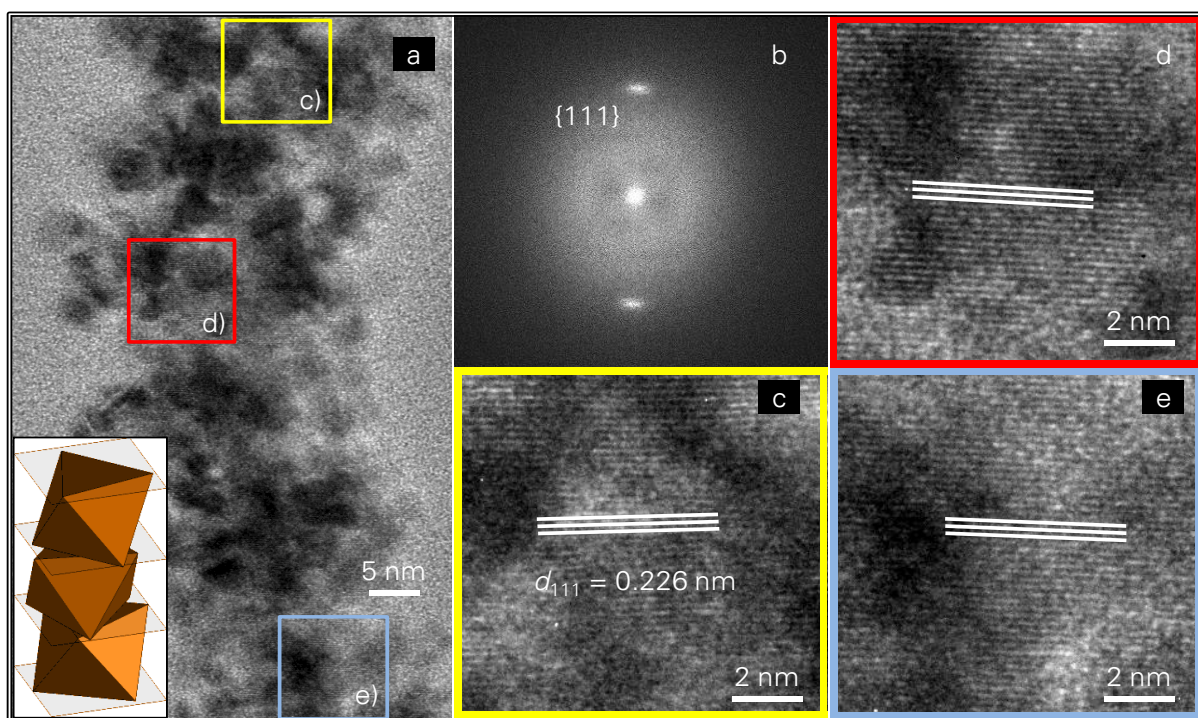


Figure 5-9. Investigation of clusters of the wire in Figure 5-7b and c. (a) Detailed TEM image. The rectangular sections represent the detail images in panels c-e. The inset schematically shows stacked octahedrons. (b) The FT of panel a shows two spots, indicating a single crystal orientation among all clusters incorporated in the nanowire. (c-e) (111)-lattice planes of the nanoclusters from the sections in panel a. White stripes are guide to the eye. All planes exhibit the same orientation (angle between (111)-crystal planes in panels c and d: 5°).

It remains to be explained why the application of a square wave to a K_2PtCl_4 solution does not bring the same results as in this section. The wires branched in crystallographic angles, however, branches and main wires were slightly curved (see Subsection 4.2.4). Interestingly, Kawasaki *et al.* also observed a transition from straight to curvy wires on addition of NaCl.³⁹ A possible reason for the curviness is the shape of the incorporated clusters in the wire. Salzemann *et al.* investigated the

fabrication of Pt-nanoclusters from H_2PtCl_6 , as it is also used in this study.⁸³ During the cluster formation process they investigate the influence of the addition of several gases. They showed that only under the addition of H_2 it was possible to achieve cubic clusters. In all other cases, the clusters were round or at least polygons of higher order. The shape of clusters is strongly dependent on the reaction kinetics of the cluster formation.^{84, 85} Since it was found that potassium strongly affects the reaction kinetics (*cf.* Section 4.2), it is plausible that the cluster shape can also be influenced by the presence of anions like potassium or sodium. The assembly of the produced shapes might easily be responsible for curvy morphologies.

Hence, the fabrication of such wires demands extremely pure conditions, since the nanowire morphology is very sensitive to impurities in the experiment environment.

5.2.3 Influence of the Waveform on the Crystallinity and Morphology

In order to explain the correlation between the waveform of the applied AC voltage and the morphology and crystalline structure of the wires presented in Figure 5-6 to Figure 5-9, further investigations at prominent sites of the wires were made.

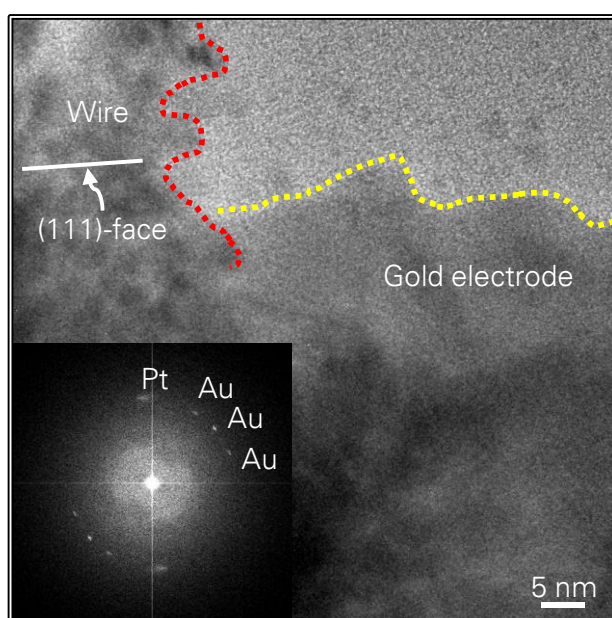


Figure 5-10. Wire in Figure 5-7b at the interface to the gold electrode. The FT in the inset shows one Pt reflex from the monocrystalline wire and three Au reflections from the polycrystalline electrode.

The TEM-image in Figure 5-10 shows the straight wire in Figure 5-7b at the interface to the gold electrode. The FT in the inset displays the (111)-reflections in accordance with Figure 5-9b and three reflections which originate from the gold electrodes. The three gold reflections of the same lattice spacing show that the electrode consists of many grains, and thus is polycrystalline. This proves that the wires do not grow epitaxially onto the electrode.

Figure 5-11 shows a kinked wire grown under the same conditions and in the same experiment as the wire in Figure 5-7b. The zoomed images reveal that the orientation of the (111)-crystal planes of the clusters does not depend on the growth direction of the nanowire, since the orientations before and behind the kink are equal (*cf.* panels d and e). The FT in panel c supports this statement, showing only two reflexions which stem from the (111)-crystal planes.

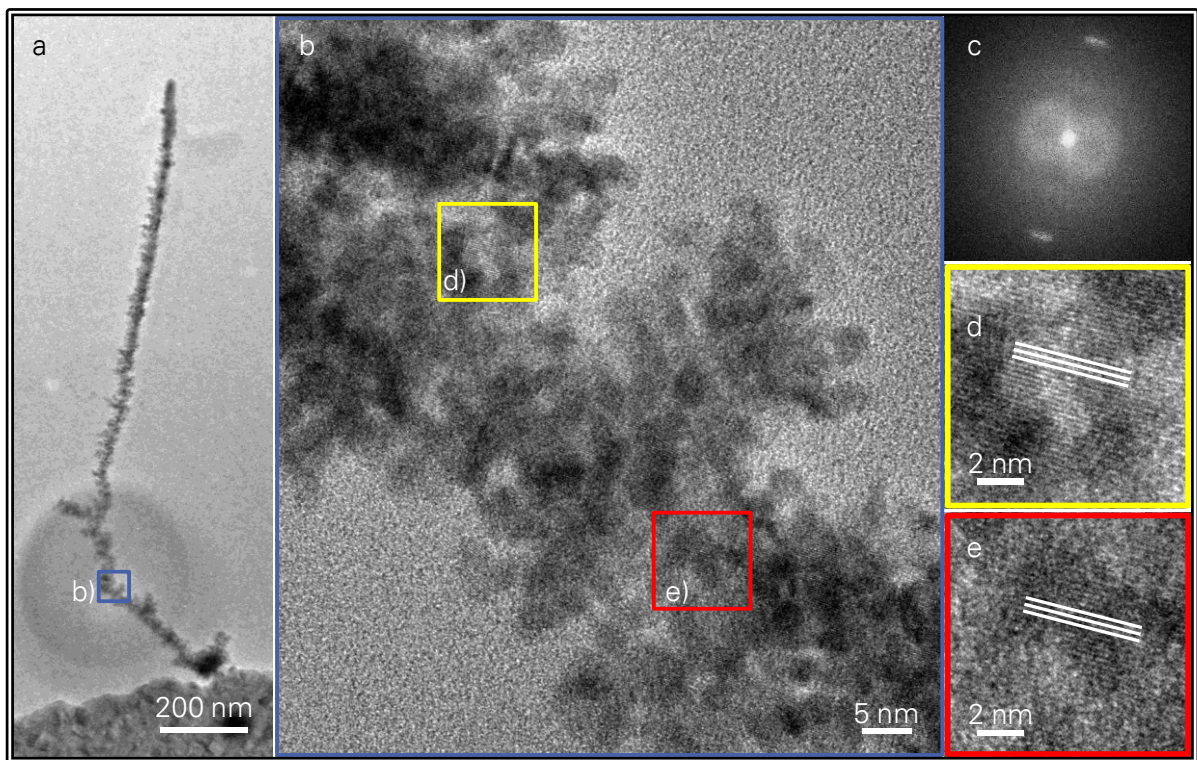


Figure 5-11. Investigation of a kinked wire grown with square-shaped voltage. (a) Overview. (b) Close-up image of the kink. (c) FT of panel b reveals oriented (111)-crystal planes. (d+e) crystal planes of the nanoclusters in the wire before and behind the kink. White stripes are guide to eye.

Two mechanisms are deemed responsible for the orientation of the nanoclusters within the wire. The first mechanism is based on the high affinity of the chlorine in

the solution to attach to platinum facets.⁶⁶ It is thus likely that the clusters are covered with anions, which could lead to an overall negative charge of the cluster. Moreover, the chlorine adsorption layer presumably inhibits the attachment to the growing wire. The DEP force attracts the polarizable clusters at any time, independent of the polarity of the electrode. However, for a charged cluster, the Coulomb force causes attraction as well as repulsion of the cluster over a period, respectively. In the case that the Coulomb force is dominant, the following mechanism of cluster incorporation could apply. At the end of the positive half period, the clusters which were in the vicinity of the wire tip have attached to the tip. Switching rapidly to negative polarity, for instance by applying a square-shaped voltage, allows electrons to tunnel from the wire tip to the cluster. These additional negative charges enhance the chlorine ion desorption, which is thought to be crucial for the cluster deposition (this is also corroborated by the observations in Section 4.2). On the contrary, if the voltage polarity changes slowly, *e.g.* with a sine function, the clusters start drifting away from the electrode due to Coulomb repulsion. When the critical voltage for tunneling is reached, the clusters are already too far from the wire tip (see Subsection 5.1.1). Consequently, the chlorine ion desorption and thus cluster incorporation does not take place. The faster the voltage increases, *i.e.* the more Fourier components are summed up according to Equation (5-2), the more electrons tunnel to the cluster, since the tunneling current depends strongly on the applied voltage.⁸⁶ An increased amount of chlorine ions desorb from the nanoclusters, facilitating cluster incorporation at the wire tip. Consequently, for a comparatively slow voltage increase (low N in Equation (5-2)), not all facets are free of chlorine and the clusters could bind to the wire tip also with facets other than (111).

The rotation of the clusters before finally binding to the tip is proposed to be the second mechanism being responsible for the change in nanocluster orientation. Apparently the clusters stack face-to-face, as illustrated in the inset of Figure 5-9a, and produce the observed long range crystallographic patterns. At first, the attracted clusters arrive with an arbitrary orientation at the wire surface. If the cluster touches the wire surface with a corner or an edge, it is blocked mechanically. Then, a torque

is built up by the attracting force, which starts to tilt the cluster, until a mechanically stable and energetically favorable orientation (usually face-to-face) is reached. The torque responsible for orientation is proportional to the electric field, which is why the wires with smaller diameters (higher M) show a better orientation pattern. Both mechanisms could account for the section-wise monocrystallinity, observed in the panels c-e in Figure 5-8. Furthermore, partial melting and recrystallisation of the clusters is assumed to take place. Järvi *et al.* have shown that clusters upon deposition can melt completely or partially due to the surface energy set free upon deposition on a substrate and then recrystallize epitaxially or distort.^{87, 88}

To conclude, it is crucial to keep the local electric field in the vicinity of the nanowire within certain conditions, which allows straight and unbranched nanowire growth. This optimum process window depends on:

- the voltage amplitude. If a certain threshold is exceeded, branching occurs due to high supersaturation.
- the voltage shape. The chlorine ion shell around the platinum species in the solution has to be removed completely before attachment, which requires a high initial voltage/time slope.
- the electrode geometry. It must be designed in a way that electric induction does not increase the global electric field around the nanowire, thus enabling deposition at other sites than the tip.

For each circuit design, these parameters have to be evaluated carefully in order to achieve the desired morphology of the wires.

5.2.4 Growth at Electrode Edges

This subsection treats the investigation of wires grown from edges of the metal electrodes. The edges were intentionally produced by fencing, *i.e.* the lift-off step during the microelectrode fabrication was done in such a way that at the electrode borders a steep edge was left. To achieve this, the gold-coated substrates were put for 30 min into NMP instead of 45 min (see Section 2.1 for more details). Nanowires grown from these steep edges at $f = 500$ kHz and $V_{\text{RMS}} = 9$ V from a 200 μM H_2PtCl_6

solution are shown in Figure 5-12. The SEM-image of the tilted substrate (panel a and b), exhibit edges with a height of approximately 200 nm as the result of this process. Remarkably, the nanowires start to grow at the top of these edges (since here the electric field and thus supersaturation is highest) and lead down to the substrate.

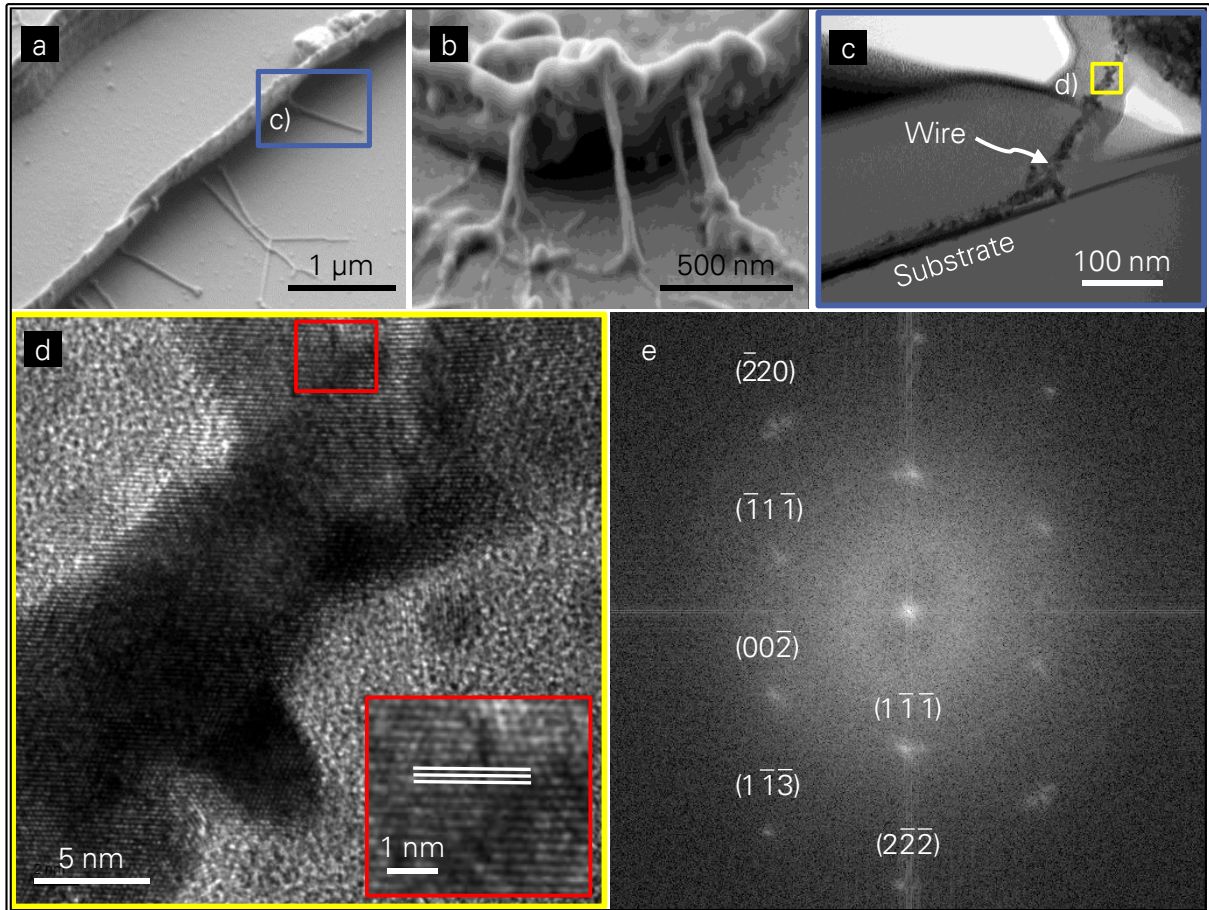


Figure 5-12. Nanowires growing down from an edge. (a, b) Tilted SEM-images of nanowires. (c) TEM-image of the marked nanowire in panel a. The paper plane is a cross-section of the electrode. (d) Nanowire detail marked in panel c. (e) Fourier-Transform of the detail in panel d. The diffraction pattern is that of an fcc-crystal shown from the $[110]$ -direction. The preparation of the sample was done by Y. Ritz, Fraunhofer IZFP Dresden. The TEM images were taken by U. Mühle, Fraunhofer IZFP Dresden.

For TEM-investigations, a focused ion beam was employed to cut out a 80-nm thin lamella of the sample. This lamella included a part of the microelectrode and the marked wire in panel a, and was attached to a TEM grid. Figure 5-12c displays a TEM image of the marked nanowire in panel a, with the paper plane being a cross-section of the electrode. The detail of this wire shown in panel d again reveals well-aligned

crystal planes (see also inset), supported by the FT of the whole image in panel e. The resulting diffraction pattern corresponds to that of a face-centered cubic (fcc) crystal shown from the [110]-direction. According to the diffraction pattern of the nanoclusters in the wire investigated in Figure 5-9 it remains unclear, whether the nanoclusters exhibit the same rotational orientation around the [111]-axis. In this case, however, it shows that all clusters in the wire possess the same orientation around each crystallographic axis.

With these experiments, it is shown that using electrochemical nanowire growth, monocrystalline three-dimensional interconnects for bottom-up nanocircuits can be fabricated.

6 Sensor Application

Apart from possible applications of the metal one-dimensional nanostructures for nanoelectronics, bottom-up grown wires can find niches in the field of biosensorics. In the following a concept is demonstrated, with which it is possible to detect and record impedance spectra of single polarizable nanoscaled particles, such as beads, or colloids. In particular, the presence and impedance of bacteria or larger viruses can be detected.

The measurements in this chapter were done by F. N. Gür and T. Janik, both Chair for Materials Science and Nanotechnology, Dresden.^{89, 90}

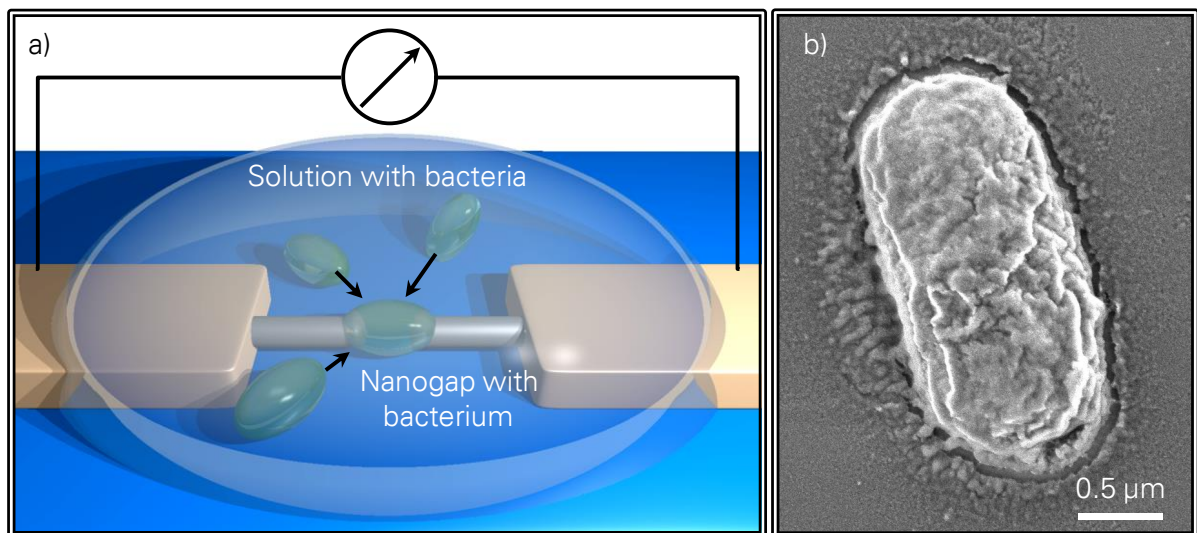


Figure 6-1. Setup of sensor concept employing electrochemically grown nanowires to measure the impedance of bacteria. (a) Polarizable particles move to the nanowire gap (indicated by the arrows). (b) SEM image of single *E. coli*.

Figure 6-1a illustrates the setup of a sensor suitable for the dielectrophoretic attraction and impedimetric detection of a single *E. coli* bacterium as displayed in the SEM image in Figure 6-1b. Platinum nanowires are grown between microelectrodes on a glass substrate as described in previous chapters. A high current, driven through the nanowire, melts it when a certain current density is exceeded and creates a nanoscaled gap. The particles are attracted to the gap by means of positive dielectrophoresis. According to the formula for the DEP force (see Equation (3-9)), the only prerequisite for attraction by DEP is that the polarizability α

of the particles must be higher than that of the surrounding fluid. The particles are attracted directly to the gap, since the electric field energy gradient and thus the DEP force is maximal at the nanowire tips (because of the small curvatures). Using a lock-in amplifier, the frequency response of objects covering the gap can be measured. Several advantages are inherent to this method.

- High sensitivity, since phase shifts can be measured with higher accuracy than amplitude shifts. The employed lock-in amplifier correlates the detection signal with a reference signal and thereby reduces the noise additionally (since noise is not correlated).
- Easy and cost-effective fabrication of the sensors. The microelectrodes are prepared with mask lithography, a standard industry process which is cost-optimized and fast (in the range of seconds). The subsequent nanowire growth occurs within seconds to minutes, depending on the growth conditions. Since the used method is bottom-up, very little material is needed.
- Suitability for low concentrations of particles and even single particles, since the analyte is attracted directly to the point of detection.
- Extremely small objects such as viruses can be detected, since the gap size is not limited by lithography resolution limits as in previous approaches.^{91, 92}

In this chapter, the recording of the frequency response and the resulting impedance spectrum of *E. coli* bacteria is presented.

6.1 Sensor Characterization

6.1.1 AC Characteristics of the Wires

The wires employed for sensing were grown from a 10 μM K_2PtCl_4 solution with a sine voltage of 10 V_p at a frequency of 100 kHz and a temperature of 316 K. Typically, the resulting wires show a straight, branched morphology with a diameter of ~ 200 nm (*cf.* Figure 6-3b). The equivalent circuit from Figure 2-3c is used to characterize the electrical behavior of the wire. The equation for the voltage measured at the lock-in amplifier is, according to the formula for a voltage divider

$$v_m(t) = \frac{Z_m}{Z_m + Z_p} v(t). \quad (6-1)$$

It is assumed that the wire acts as a resistor with an alternating current (AC) resistance R_w , which replaces Z_p in Equation (6-1). Z_m is the input impedance of the measurement device, in this case of the lock-in amplifier that has a parallel RC circuit:

$$Z_m = \frac{R_m}{j\omega R_m C_m + 1}. \quad (6-2)$$

Inserting Equation (6-2) into Equation (6-1) and setting $R_w = Z_p$ gives

$$v_m(t) = \frac{1}{j\omega R_w C_m + R_w / R_m + 1} v(t). \quad (6-3)$$

It is further assumed that $R_w \ll R_m$, which is reasonable because the resistor of the lock-in amplifier's input impedance is 10 M Ω . Then Equation (6-3) can be simplified to the frequency response of a low-pass RC filter

$$v_m(t) = \frac{1}{1 + j\omega R_w C_m}, \quad (6-4)$$

with the wire resistance R_w and the input capacitance C_m as its circuit elements, as illustrated in Figure 6-2a. A low-pass RC filter has a characteristic frequency response, *i.e.* the progression of amplitude and phase over the frequency.⁹³ The amplitude, given in dB = 20 log₁₀($v_{m,P} / V_P$) (with $v_{m,P}$ being the peak amplitude of the measured signal), proceeds at the zero-line and then decreases with a slope of 10 dB/decade. The point at which -3 dB is reached, is called the "cut-off frequency" f_c . The phase on the other hand is also equal to zero at first, however decreases until it reaches -90° and then stays stable. At the cut-off frequency f_c , the phase $\varphi = -45^\circ$.

Figure 6-2b shows the measured frequency response of the system lock-in amplifier/nanowire. The high initial slope of both amplitude and phase at around 10 Hz originates from the short measurement time constant used in this experiment (5/f). While the time constant is not long enough for 10 Hz – 11 Hz, the system

measures reliably above this frequency range. Both amplitude and phase proceed according to the low-pass RC filter response (mind the reverted y-axis for the phase). The cut-off frequency $f_c \approx 10$ kHz, marked with the green dashed line, varies for different wires. It is related to the capacitance of the lock-in and the resistance of the wire:⁹³

$$f_c = \frac{1}{2\pi R_w C_m} . \quad (6-5)$$

Inserting the cut-off frequency from Figure 6-2 and the input capacitance $C_m = 25$ pF, the resulting AC resistance of the wire is very high with $R_w = 637$ k Ω . Typical values for the DC resistance are between 1 k Ω and 3 k Ω , which is two orders of magnitude lower than the AC resistance. It is well known that due to the skin effect, the AC resistance is generally higher than the DC resistance.⁹⁴ The reason for this is the rapid decay of the electric field in a conductive material for high frequencies. Thus, the current in the conductor is limited to a thin layer at the conductor surface, which has the approximate thickness of the so-called skin-depth

$$\delta = \frac{1}{\sqrt{\pi f \mu \sigma}} . \quad (6-6)$$

Here, μ is the magnetic permeability (as the product of relative and vacuum permeability μ_r and μ_0) and σ the electrical conductivity of the material. Platinum as paramagnetic material has a relative permeability of ~ 1 and its conductivity is $\sim 10^8$ S/m. Inserting these values and the cut-off frequency 10 kHz, the resulting skin-depth is $\delta = 500$ μm . With a wire diameter of ~ 200 nm, this would mean that the electric field penetrates the wire completely and a change in resistance with increasing frequency is not explicable. However, when going to the nanometer scale, the diffusive scattering at the wire surface increases immensely and the mean free path of electrons is shorter than for bulk materials.^{95, 96} TEM investigations in Section 5.2 revealed that the electrochemically grown nanowires consist of small clusters in the size range of 2 nm – 5 nm. It is assumed that the wires grown from K_2PtCl_4 show a similar structure as the wires grown from H_2PtCl_6 . This means that

small clusters with a narrow size distribution are incorporated, yet not large ones (25 nm) as justified in Subsection 4.1.1. Due to diffusive scattering, grain boundaries have also a tremendous impact on the propagation of the electric field.^{97, 98} Moreover, downsizing platinum can cause ferromagnetism in the nanoclusters, as discussed on page 90. This can increase the magnetic permeability by several orders of magnitude, lowering the skin depth. Due to these facts, there might be a significant decrease in skin depth that already frequencies in the region of 100 kHz have a considerable effect on the AC resistance of the wire.

The frequency response of each grown wire has been checked before melting and only those which had a cut-off frequency of at least 100 kHz (resulting in an AC resistance of $R_w \leq 64 \text{ k}\Omega$) were used for sensing. Further investigations revealed that wires grown with a square-shaped voltage from a 10 μM K_2PtCl_4 solution, have a considerably higher percentage of wires with $f_c \geq 100 \text{ kHz}$. This is attributed to the crystallographic alignment of the constituting nanoclusters, as discussed in Section 5.2; the grain boundary scattering then decreases notably.⁹⁹

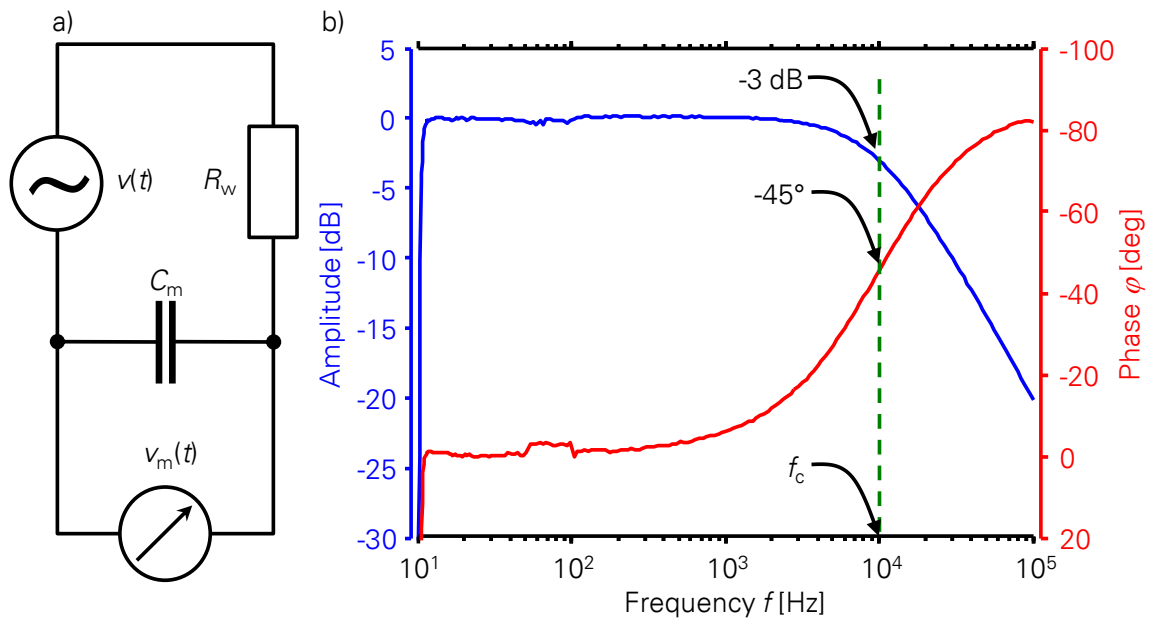


Figure 6-2. Electrical behavior of a typical nanowire. (a) Equivalent circuit of wire and lock-in amplifier. (b) Frequency response of the system lock-in amplifier/nanowire matches that of a low-pass RC filter. Note the reverted y-axis for the phase.

6.1.2 Gap Formation

After the nanowire growth, a DC voltage is applied to the wire in order to melt it and create the gap. The recorded I/V -curve of such a process is shown in Figure 6-3a. The current rises linearly with the voltage, which shows that the metal nanowires behave Ohmic. The DC resistance calculated from the slope of the curve is $\sim 1.3 \text{ k}\Omega$. At $I = 1.8 \text{ mA}$ the wire melts, which causes the sudden current drop. The current density $j = I/A$, with A as the area of the cross-section through the wire. Taking $\sim 75 \text{ nm}$ as the wire radius (*cf.* Figure 6-3b) and assuming a circular cross-section, a current density of $j = 1.0 \cdot 10^{11} \text{ A/m}^2$ results at the melting point.

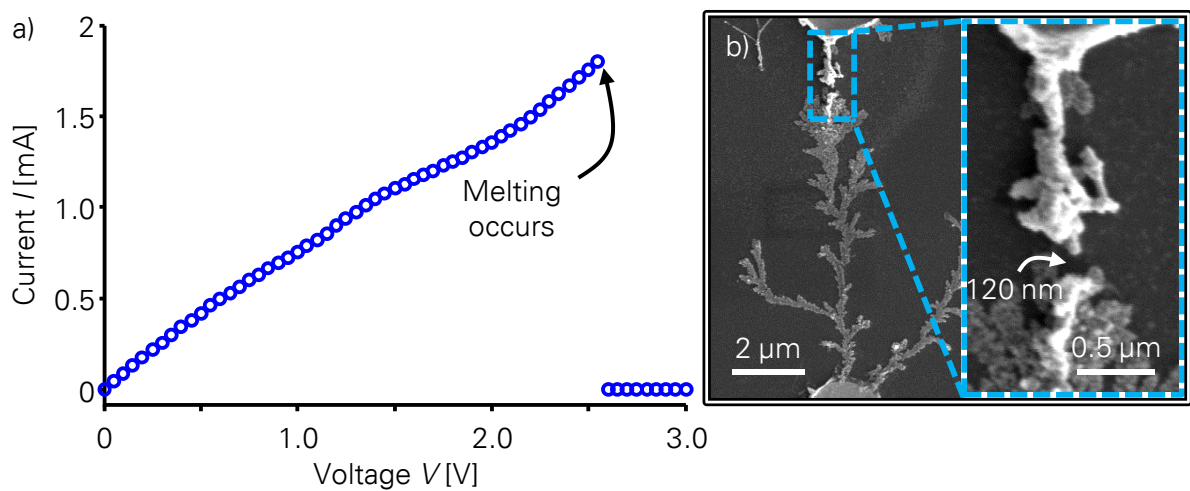


Figure 6-3. Creation of the gap for the sensor. (a) I/V -characteristics. The wire melts at $\sim 1.8 \text{ mA}$. (b) The created gap is 120 nm.

This value is rather high, comparing it to the DIN standard for the maximum current density in macroscopic wires for technical applications. For bulk copper cables (area of cross-section 1 mm^2 to 70 mm^2), the maximum allowed current density does not exceed $2 \cdot 10^7 \text{ A/m}^2$.¹⁰⁰ An increase of the maximum current density by several orders of magnitude for *e.g.* gold nanowires was observed in experiment, however mostly wires with diameters below 10 nm .^{101, 102} Zhang *et al.* identify the significant reduction of electromigration by the oriented crystalline structure in such small nanowires as the dominating mechanism behind this.¹⁰³ Electromigration occurs preferably at transitions from small grains to large grains in the wire, or vice-versa.¹⁰⁴ Since in the presented wires the cluster-size distribution is very narrow, the

formation of voids or “hillocks” (accumulations around the wire due to electromigration) can be confined to a minimum, leading to a higher maximum current density.

It is further assumed that melting in order to create the gap does not decrease the cut-off frequency, since an epitaxial recrystallization is probable.^{87, 88}

6.2 Measured Data

6.2.1 Electric Properties of *E. coli*

The data presented in this chapter provide an impedance spectrum of *E. coli*, which made it necessary to fix the bacterium in the nanowire gap and to remove all other disturbing influences. Therefore, after attraction, the sample was dried to remove the water, since water could contribute to the overall conductivity.⁹²

In the present experiments 0.5 μl of bacteria suspension with a concentration of 10^3 cells/ μl were pipetted on top of the electrodes with the grown nanowires. In order to attract the bacteria to the nanowire gap, it is necessary to apply an AC field with a frequency causing positive DEP (*cf.* Equation (3-11)). It was found that attraction works well with $V_p = 0.5$ V and $f = 100$ kHz, applied to the electrodes over 1 min at room temperature. Subsequent heating on the hotplate at 50° for 1 min caused the water to evaporate, however still to keep the organic components of the bacterium intact. The samples were then contacted with the tip-probing station for measurement as described in Section 2.2. Figure 6-4a shows trapped bacteria in between nanowire gaps.

After contacting the sample, a sinusoidal voltage with $V_p = 3$ V was applied and the frequency response was measured. To calculate the impedance of the bacteria, Equation (6-1) is employed again. By rearranging the equation, the impedance of the particle, *i.e.* the bacterium (or the gap without the bacterium), Z_p can be found with

$$Z_p = Z_m \left(\frac{V_p}{V_m} - 1 \right) \quad (6-7)$$

The according Nyquist plot of the impedance of both the gap with bacteria and without bacteria is shown in Figure 6-4b. The impedance before trapping (only the gap) of the *E. coli* starts to describe a semicircle, coming from high frequencies. However, below ~ 100 Hz, both reactance and resistance become very high (up to $200 \text{ G}\Omega$), therefore not all data points are displayed in the diagram. The impedance after trapping (gap with bacterium) is a semicircle over the full frequency range from 10 Hz to 100 kHz. If the real axis of the Nyquist plot intersects the center of the (thought) circle and the imaginary axis is at the edge of the (thought) circle like the data show, the measured data correspond to a parallel RC-equivalent circuit.^{105, 106} This is a reasonable result, since especially the cell wall of the bacteria is conductive to a certain extent^{107, 108} and the cytoplasm acts as dielectric material, causing a capacity. Therefore, the data were fit to the impedance of a parallel RC circuit as in Equation (6-2). As a result, the resistance of this equivalent circuit $R_{\text{eq}} = 52 \text{ G}\Omega$ and its capacitance $C_{\text{eq}} = 3.1 \text{ fF}$. The resistance is in good accordance with current measurements at dry *E. coli* conducted by Lu *et al.* A current of $2 \cdot 10^{-11} \text{ A}$ at a DC voltage of 1 V was measured over four *E. coli* cells, which corresponds to a resistance of $50 \text{ G}\Omega$,⁹² thus being on the same order of magnitude as the present result. The AC wire resistance of $\sim 60 \text{ k}\Omega$ is then negligible. The capacitance of the *E. coli* can be estimated according to the sphere capacitor model (see Section 3.1):

$$C = \frac{4\pi\epsilon_0 r_1 r_0}{r_1 - r_0} \quad (6-8)$$

The radius of the inner electrode r_0 is the nanowire radius with $\sim 75 \text{ nm}$, as in Section 6.1. The radius of the outer electrode, r_1 is the radius of the nanowire r_0 plus the size of the gap, which is estimated as $r_1 = r_0 + d \approx 200 \text{ nm}$. The capacitance of the bacterium comprises three parts: inner membrane, outer membrane and cytoplasm. Since in a cross-section of *E. coli* the cytoplasm covers the largest area and its relative permittivity is at least equal to that of the membrane parts, the cytoplasm is taken as the dominant contribution for the capacitance. The relative permittivity of the whole bacterium is thus taken as ~ 80 , according to reported values for the cytoplasm between 60 and 100.^{91, 109} This rather coarse estimate yields

a capacitance of 1.1 fF, being on the same order of magnitude as the fitted value for C_{eq} of 3.1 fF. Taking into account that the measured data recorded the spectrum of two *E. coli* (cf. Figure 6-4a) and that then, assuming each *E. coli* having the same electric properties, C_{eq} is double the value of the capacity of one *E. coli*, the calculated and the measured values are unexpectedly close.

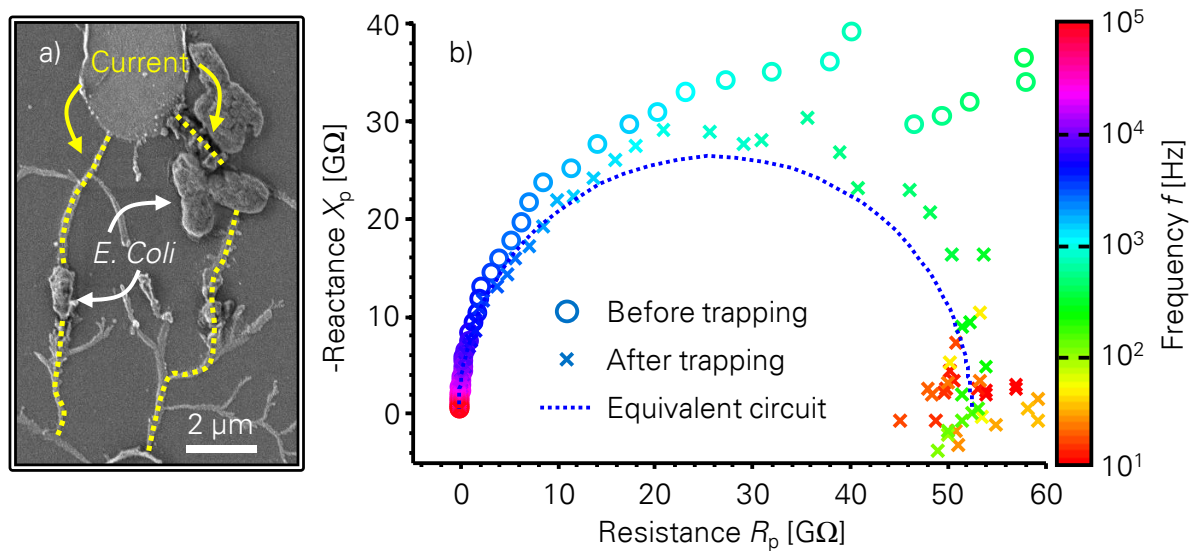


Figure 6-4. Trapped *E. coli* in a gap between nanowires. (a) SEM-image. Dotted lines indicate current path. (b) Nyquist plot of the impedance of the gap in panel a without bacterium (circles) and with bacterium (crosses). The dotted curve is a least-square fit to the impedance of the *E. coli* according to a parallel RC-circuit.

6.2.2 Sensitivity of the Nanowire-Based Sensor

The actual detection bases on the ratio of the impedance before the trapping of bacteria and after it. Figure 6-5 displays the reactance and the resistance over the frequency, which shows that the most sensitive frequency range is below 200 Hz. It is also noticeable that the ratio of the impedance of before to after trapping (hereafter “trapping ratio”) undergoes the most significant changes in the imaginary part. While the trapping ratio of the real part never exceeds 4, the trapping ratio of the imaginary part reaches 200 for only 2 *E. coli* cells, which is also demonstrated by the inset with a logarithmic y-axis. This underlines the fact that measuring the phase angle of the signal can fundamentally enhance the sensor performance. While the identified frequency range up to 200 Hz may well be valid for dry conditions, measurements in liquid can easily bring up different sensitive regions, since the

electric properties of the involved organic molecules (lipids, proteins) change considerably with the water content.^{110, 111}

Inserting R_{eq} and C_{eq} in Equation (6-5), the cut-off frequency of the equivalent circuit is $f_{c,eq} = 975$ Hz, where Figure 6-5 shows the maximum of the reactance. The inverse of this frequency is equal to the time constant of the equivalent circuit, being approximately 1 ms. This interval is the time needed to transfer charges from one end of the gap through the bacterium to the other, in order to reach ~63% of the applied voltage.⁹³ Reversing the polarity of the applied voltage after 1 ms, causes a high storage of electrical energy in the bacterium (=capacitor), which leads to a rise in the reactance and a decrease in the resistance.

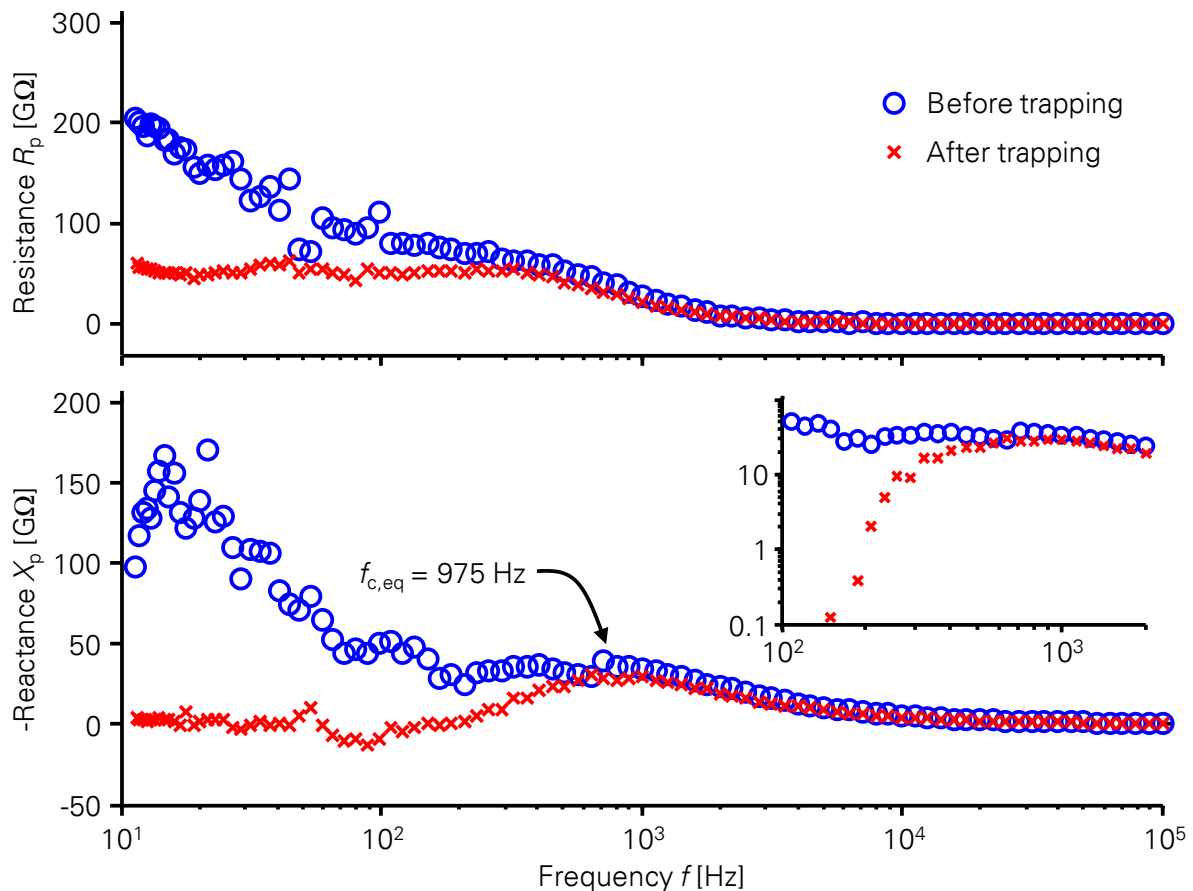


Figure 6-5. Sensor impedance versus frequency without bacterium (circles) and with bacterium (crosses). The reactance is maximal at the characteristic frequency f_{eq} . The inset shows a rapid increase of the imaginary part of the impedance after 200 Hz.

6.3 Future Perspective

The prototype results of the sensor concept presented in the previous section showed the high potential of the method. However, in order to obtain a proper product, a number of improvements and modifications must be applied.

Instead of dry measurements, a liquid environment is desirable, *e.g.* for monitoring tap water for pathogenic bacteria. To guarantee a continuous surveillance, integrating the sensor into a microfluidic setup is a suitable option (see Figure 6-6). With the prototype presented in the last section, it is only possible to detect one analyte at a time, although it can be reused by rinsing the gap. Adjusting the ratio of attraction voltage to fluid velocity in a way that the analytes become attracted, however do not attach, causes a signal change each time an analyte passes by. This opens up the possibility for a cell counter as further application.

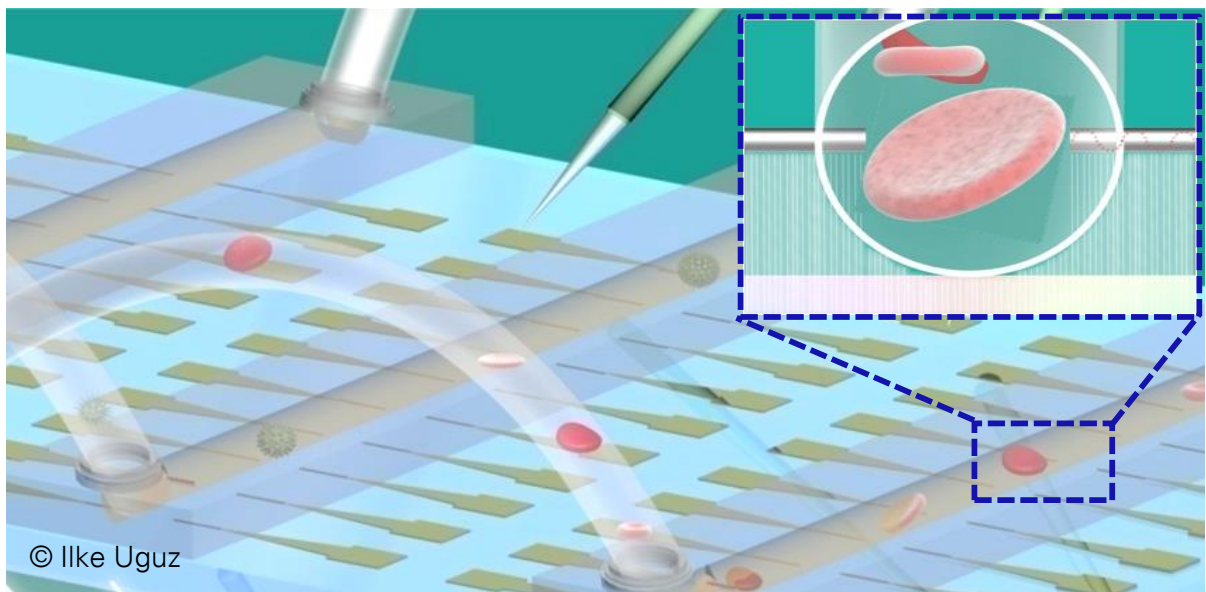


Figure 6-6. Concept figure of future sensor chip. Several microfluidic tubes transport the analyte over the nanoelectrodes for detection.

Moreover the present setup lacks selectivity and attracts all polarizable objects, if they are small enough to get attracted by the DEP force. In addition to functionalize the nanowires with antibodies or aptamers, there is also an elegant method to distinguish between analytes. Bunthawin *et al.* found out that for instance dead and living cells exhibit different signs of the real part of the Clausius-Mossotti factor at the same frequency, which decides about positive or negative DEP.¹¹² With several

pairs of nanowires operating at different frequencies, this “dielectrophoretic fingerprint” may be detected, thus making the sensor specific. Furthermore, it is necessary to establish a precise control of the gap size, which has been reported already during the growth phase of nanowires.¹¹³ With different gap sizes, a size-selective (“nanosieve”) detection can also take place, since a direct contact of the analyte yields a higher signal change than simply passing by.

7 Closing Remarks

7.1 Conclusion

The growth of ultrathin (down to 15 nm), straight and unbranched Pt nanowires, grown by the DENA process was demonstrated. The application of the electrochemically grown nanowires in an impedimetric sensor was shown. In detail, as output of the conducted work, the following important conclusions could be drawn.

The reaction kinetics of the nanowire growth has been investigated in experiment and in theory. Both the concentration profile of platinum species around the growing nanowire and the growth velocity of the wire are heavily influenced by the parameters bulk concentration, temperature and voltage. The influence of the latter on the growth velocity has only been shown experimentally. Depending on these setup parameters, the reaction kinetics of the deposition of platinum during growth is either reaction or diffusion-limited. The comparison of the growth velocity of the nanowires with the predictions from the model yields qualitative agreement, except for the voltage dependence.

The morphology of the nanowires comprises several factors. Branching, for instance, is a consequence of excessive supersaturation. It is mainly controlled by the bulk concentration of platinum species in the solution, the applied external voltage and the chlorine layer at the wire and/or around the platinum in solution. It is feasible that in other systems than H_2PtCl_6 or K_2PtCl_4 the anion can play a similar role. The diameter of the nanowires is affected on the one hand by the frequency of the applied voltage, because the supersaturation can only be decreased in a limited time window, *i.e.* the negative half-wave in which the nanowire grows. On the other hand, the concentration profile of the metal species in solution determines the minimum radius of a stable solidification front. Crucial to the straightness of the nanowires is the signal form (which, ideally, should be square), the type of cations present in solution and the electric field in the nanowire vicinity. The applied field should be just low enough that the threshold potential is exceeded. The nucleation

density is influenced by the voltage, the frequency, the temperature and the electrode geometry. This is attributed to the presence of the chlorine layer at the electrodes.

Concerning the crystallography, TEM images showed that the wires consist of nanoclusters with 2-5 nm in size. A square voltage as growth signal causes the alignment of the (111)-planes of the clusters within the wire. The orientation of the crystal planes depends on the initial voltage/time slope of the applied voltage. The orientation of the clusters in the wire is directly related to the straightness of the wires. Possible explanations include the desorption of a chlorine layer from the platinum clusters, which is necessary to attach as preferred energetically and the rotation of the clusters before finally binding to the wire.

Platinum wires grown with a sine wave were analyzed with respect to their electronic properties and their implementation in the sensor application. They exhibit a resistivity of around one order of magnitude lower than that of bulk platinum, which is attributed to the polycrystallinity in the wire. Despite their high resistivity, the maximum current density before melting of the wire is several orders of magnitude higher than that of bulk copper. The uniform cluster size distribution in the wire is assumed to be the cause for this. The impedimetric detection of bacteria succeeded in the dry state. The capability of single-object detection was shown.

It must be emphasized that a good part of the points are clearly interrelated to each other. As a consequence, carefully balancing the setup parameters is pivotal to achieve a controllable morphology of the nanowires.

7.2 Outlook

From these conclusions, a variety of follow-up research arises and new applications are feasible.

The future research includes the theoretical analysis of the elektrokinetic flow of the electrolyte induced the tangential field component around the nanowire. The consideration of this phenomenon might be able to account for the difference between the experimentally measured growth velocities and the theoretically

predicted ones. The charge separation according to the externally applied electric field in turn creates a considerable field, with its magnitude possibly being in the same range. Since the electric field surrounding the nanowire is decisive for the morphology of the wire, a detailed knowledge of the overall field might be of importance.

The impedimetric sensor can be improved by integrating the wire into a microfluidic setup for continuous surveillance of a flowing medium (*e.g.* drinking water control). A further aim in the sensor development is the enhancement of the selectivity of the sensor. This can be either done by functionalizing the nanowire with antibodies or aptamers (key-lock principle) or by recording dielectrophoretic spectra of eligible analytes and the development of a multiple-frequency sensor array. The main advantage of the sensor is actually the detection of extremely small particles, like *e.g.* viruses. In order to achieve proper sensing of those species, the size of the gap has to be determined in a controlled manner. This can be done by controlled electromigration, as *e.g.* demonstrated by Austin *et.al.*¹¹⁴

Important engineering guidelines for the fabrication of straight nanowires have been established. The next step is the implementation of these into defined circuits for nanoelectronics, in which the microstructures are fabricated by conventional mask lithography and the nanostructures by means of electrochemical nanowire growth. The possibility to deposit wires at electrode inhomogeneities as illustrated and the control over the nucleation density are further important tools for this. Considering the huge resistance towards electromigration of the nanowires, such circuits would be highly reliable.¹⁰⁴

The further examination of crystallographic manipulation of the clusters incorporated in the nanowire can be the key to define the shape of the grown structures. The deterministic bottom-up growth of nanowires with “programmable” shapes and thus properties, in combination with the demonstrated three-dimensional growth, might become a powerful tool in miscellaneous fields such as photonics.

Further applications include the manufacturing of fractal antennae for the terahertz range.^{94, 115} Such antennae stand out for their broad bandwidth and would be a major

breakthrough in THz technology. Furthermore, intriguing applications might also appear in view of recently discovered ferromagnetism and high magnetic anisotropy of nanosized platinum clusters and ultrathin platinum wires.¹¹⁶⁻¹¹⁸ Moreover, the high surface-to-volume ratio and the better electrical transport characteristics provided by the low diameter of the nanowires likely can boost the sensitivity of nanoscaled gas or biosensors, *e.g.* hydrogen or glucose sensors.¹¹⁹

Finally, electrochemically grown nanowires offer a promising perspective for future applications. Although still considerable effort has to be put in the refinement of this method, the advantage of easy and cost-efficient fabrication of such precise structures as demonstrated should be a sufficient motivation.

Appendix

Solution of Differential Equation (3-16)

The homogenous solution of the differential equation (3-16) can be found by separating variables:

$$\frac{\partial c}{c} = \frac{\hat{F}_{\text{DEP}}}{k_B T r^5} \partial r, \quad (\text{A-1})$$

$$\Rightarrow c_{\text{hom}} = A_2 \exp\left(-\frac{\hat{F}_{\text{DEP}}}{4k_B T r^4}\right). \quad (\text{A-2})$$

A_2 [m^{-3}] is another integration constant with the dimension of a concentration. By variation of constants one can find the general solution

$$c_{\text{gen}} = A_4(r) c_{\text{hom}}, \quad (\text{A-3})$$

which reads

$$c_{\text{gen}} = -\frac{A_1}{D} \exp\left(-\frac{\hat{F}_{\text{DEP}}}{4k_B T r^4}\right) \left(\int_{r_a}^r \frac{\exp\left(\frac{\hat{F}_{\text{DEP}}}{4k_B T r'^4}\right)}{r'^2} dr' + A_3 \right). \quad (\text{A-4})$$

During the variation of constants, the constant A_2 cancels and another integration constant A_3 [m^{-1}] appears, in addition to r_a [m], which is arbitrary.

The model includes these boundary conditions:

- the concentration in an infinite distance from the nanowire tip is the bulk concentration c_∞ . From this first boundary condition

$$c(r \rightarrow \infty) = c_\infty \quad (\text{A-5})$$

we can determine the first integration constant

$$A_1 = - \frac{c_\infty D}{\int_{r_a}^{\infty} \frac{\exp\left(-\frac{\hat{F}_{DEP}}{4k_B T r'^4}\right)}{r'^2} dr' + A_3} . \quad (A-6)$$

- the flux at the nanowire tip $j(r=r_0)=:j_0$ is equal to concentration at the nanowire tip $c(r=r_0)=:c_0$ times the reaction rate k_r of the deposition at the nanowire tip. The second boundary condition reads

$$j_0 = -k_r c_0 . \quad (A-7)$$

From this assumption, we can determine the second integration constant

$$A_3 = \frac{D \exp\left(-\frac{\hat{F}_{DEP}}{4k_B T r_0^4}\right)}{r_0^2 k_r} - \int_{r_a}^{r_0} \frac{\exp\left(-\frac{\hat{F}_{DEP}}{4k_B T r'^4}\right)}{r'^2} dr' . \quad (A-8)$$

Inserting the integration constants in Equation (A-4), the solution in Equation (3-19) is achieved.

Root-Mean-Square of Superimposed Sine Waves

The calculation of the root-mean-square of a Fourier series for a rectangular wave as in Equation (5-2) is shown. The Fourier series itself is

$$v(t) = \hat{v} \frac{4}{\pi} \sum_{n=0}^N \frac{\sin((2n+1)\omega t)}{2n+1} . \quad (A-9)$$

with N being the number of Fourier components and \hat{v} the amplitude of the voltage. Applying the formula for the root-mean-square

$$V_{\text{RMS}} = \sqrt{\frac{1}{T} \int_0^T v^2(t) dt} , \quad (A-10)$$

with T being the period of the applied harmonic signal, one has:

$$V_{\text{RMS}} = \sqrt{\frac{16}{\pi} \sum_{n=0}^N \frac{1}{T(2n+1)} \int_0^{T(2n+1)} \hat{v}^2 \frac{\sin^2((2n+1)\omega t)}{(2n+1)^2} dt} . \quad (A-11)$$

The integral can be solved with $\sin^2(\alpha) = 1/2(1 - \cos(2\alpha))$ and setting $fT = 1$ and $\omega = 2\pi f$, the root-mean-square of a square shaped signal is

$$V_{\text{RMS}} = \frac{4\hat{v}}{\pi} \sqrt{\sum_{n=0}^N \frac{1}{2(2n+1)^2}}. \quad (\text{A-12})$$

Solving for \hat{v} and inserting Equation (A-12) in Equation (A-9) yields Equation (5-2). Since the series under the root of Equation (A-12) converges for $N \rightarrow \infty$ to $\pi^2/16$, the root-mean-square of Equation (A-9) is exactly \hat{v} . The other limit for $N = 0$ (that is a pure sine), leads to $V_{\text{RMS}} = \frac{4}{\pi\sqrt{2}}\hat{v}$.

Fractal Dimension of Wires in Subsection 5.1.4

The results provided in this part were calculated by U. Cikalova and J. Nicolai from Fraunhofer IZFP, Dresden.

Fractal analysis is generally used for the numerical analysis and description of the complexity of natural and mathematical objects.¹²⁰ A typical application of fractal analysis is the characterization of structures in images taken by different imaging methods like conventional optics, SEM, TEM, or ultrasound image, etc.¹²¹ Such analysis may provide quantitative information about the structure of the nanowires, a relationship between the parameters of the growth setup and the fractal dimension can be found. In order to minimize the influences of different magnifications, regions of interest (ROI) of the same size were determined and rescaled to 300 x 300 pixels (see Figure A-1).

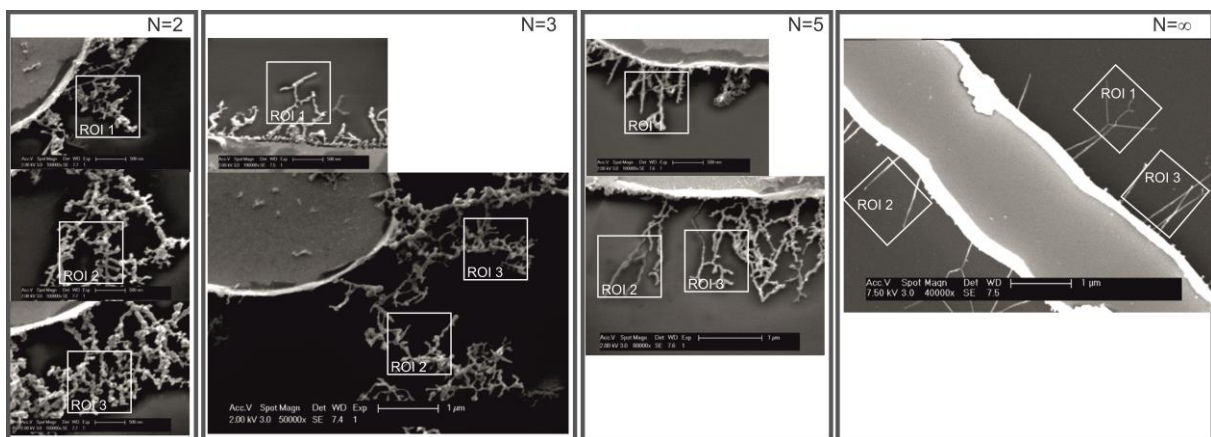


Figure A-1. Selection of different regions of interest in SEM images of nanowires to determine the fractal dimension.

The fractal analysis of these images was carried out by the Box-Counting (BC) method.¹²² To avoid disturbances by the different contrasts of the images, an optimal threshold was chosen for the conversion of the gray-level images to binary images according to Otsu.¹²³ An example of the converted image is shown in Figure A-2. Using the BC method, the binary image of the object is covered with boxes of length r . The fractal dimension D_B is estimated from the equation

$$D_B = -\lim_{r \rightarrow 0} \frac{\log(N(r))}{\log(r)}, \quad (\text{A-13})$$

where $N(r)$ is the number of the boxes needed to completely cover the object in the images.

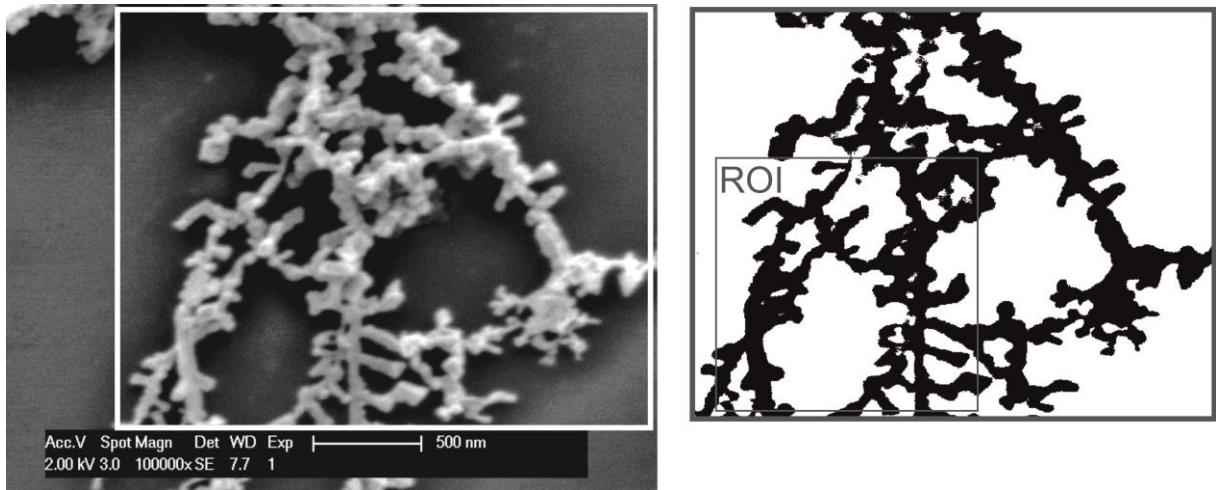


Figure A-2. Example of an SEM image converted to a binary image.

Figure A-3 shows the results of the computation of the fractal dimension. The value of the fractal dimension D_B correlates well with the different initial increase of the applied voltages. The error bar shows the variation in the D_B values due to the choice of the ROI and the definition of the threshold by the binarization process.

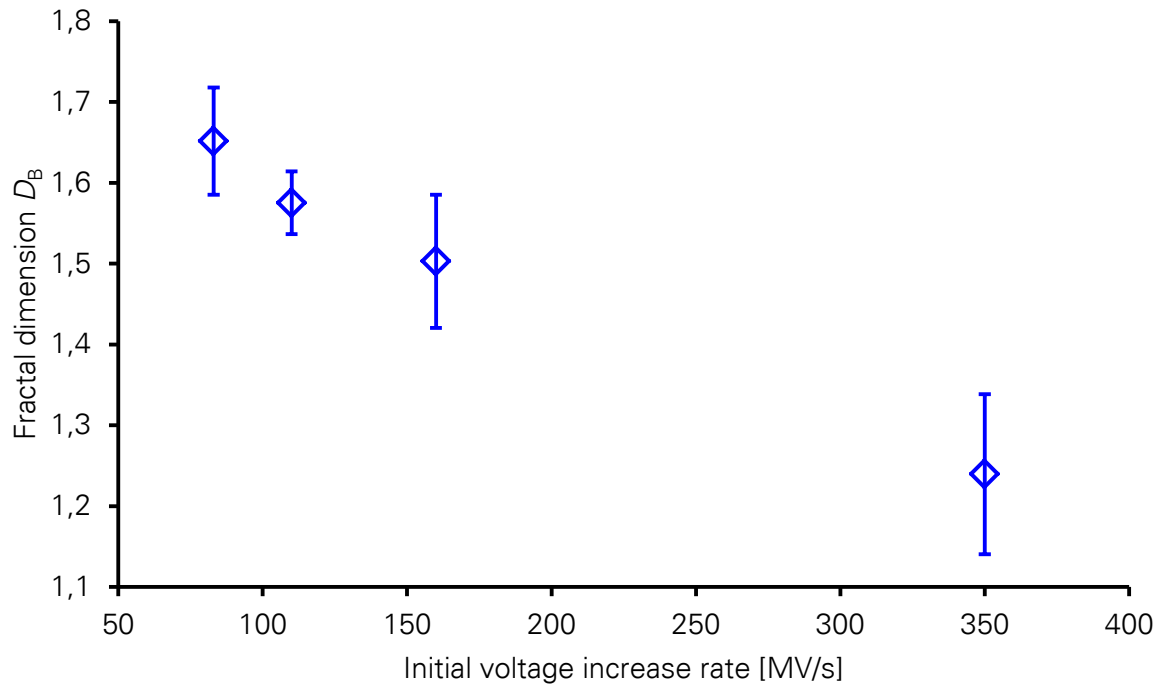


Figure A-3. Fractal dimensions of nanowires grown with differently shaped voltages. The number of Fourier components N of the single data points are, from left to right, 2, 3, 5 and towards infinity (square shaped), respectively. The number of Fourier components corresponds to a specific initial voltage increase (see main text).

The presented preliminary results of the quantitative analysis of the nanowire structure should be improved in the future by optimizations in the image processing process.

Scientific Output

From this thesis, the following publications resulted:

Nerowski, A.; Poetschke, M.; Bobeth, M.; Opitz, J.; Cuniberti, G. *Langmuir* **2012**, *28*, 7498–7504

Nerowski, A.; Opitz, J.; Baraban, L.; Cuniberti, G. Bottom-up Synthesis of Ultrathin Straight Platinum Nanowires: Electric Field Impact, *Nano Res.* **2013**, *6*, 303-311.

Nerowski, A.; Wiesenhütter, U.; Poetschke, M.; Nicolai, J.; Cikalova, U.; Dianat, A.; Erbe, A.; Opitz, J.; Bobeth, M.; Baraban, L.; Cuniberti, G. Platinum Nanowires with Programmable Crystallinity, submitted.

Schmädicke, C.; Nerowski, A.; Baraban, L.; Renner, L. D.; Cuniberti, G. Fabrication of Copper Nanowires from Aqueous Solution, Proceedings of AMA Conferences, **2013**.

Nerowski, A.; Gür, F. N.; Opitz, J.; Baraban, L.; Cuniberti, G. Single *E.coli* Impedance Measurement of Nanoscaled Objects with Metal Nanowires, in preparation.

Nerowski, A.; Gür, F. N.; Opitz, J.; Baraban, L.; Cuniberti, G. Sensoreinrichtung zum Erkennen von polarisierbaren Partikeln in einem Fluid, **2013**, Gebrauchsmuster AZ 20 2013 002 076.8

Acknowledgements

Nach knapp hundert Seiten Wissenschaft darf es auch ruhig mal etwas persönlich werden. Ich möchte die Gelegenheit nutzen, um mich bei allen, die mich am MBZ begleitet haben, zu bedanken. Die Liste der Kollegen, die dazu beigetragen haben, dass diese Zeit so wurde, wie sie geworden ist, ist lang, doch möchte ich hier ein paar besondere Persönlichkeiten herausstellen.

Zunächst geht der Dank an dich, Giovanni, als mein Doktorvater, auch dafür, dass du mich für diese wunderschöne Stadt begeistern konntest. Du hast mir damit die Gelegenheit gegeben, an einem international besetzten Lehrstuhl in einem unglaublich interessanten und multidisziplinären Feld zu arbeiten.

Manfred, als das „Urgestein“ des Lehrstuhls hatte ich mit dir als Betreuer das große Los gezogen. Es gibt wohl wenige Personen auf dieser Welt, die so viel Fachwissen in sich tragen und dennoch ihr Gegenüber immer auf Augenhöhe behandeln.

Countless time was spent by you, Larysa, on listening to progress, correcting drafts or simply contributing with visionary ideas. As “Vollblutwissenschaftlerin”, I hope you can stay on the science path!

Lieber Jörg, ich habe die Zeit mit dir besonders geschätzt, weil die Gespräche mit dir immer sehr offen und konstruktiv waren. Bleib so und auch für dich gilt: viel Erfolg auf dem Weg in den Elfenbeinturm!

Markus, ich denke wir haben den Spagat zwischen Theorie und Experiment ganz gut gemeistert! Vielen Dank auch für die lehrreichen Diskussionen mit dir, insbesondere auch außerhalb des Fachs.

Ein ganz besonderes Dankeschön gilt den Mädels aus meinem Büro. Anja, Claudia, Lotta (in alphabetischer Reihenfolge, damit ich mir auch nichts anhören muss!), ihr habt die Doktorandenzeit an diesem Lehrstuhl mit dem gewissen „Etwas“ versehen, das auch zur Arbeit dazugehört. Ob Bürokratie mit Anja (jetzt habe ich Zeit, etwas aus dem Buch zu basteln... etwas zu spät), Wetten über Claudias Kind (hast du den Zettel eigentlich schon eingerahmt?) oder Versuche, Lotta

anzusprechen (Lotta? ... Lotta...? Lotta!!!), ihr habt dieses Büro zu einem Ort gemacht, wo ich gerne hingegangen bin.

Für den Spaß bei der Arbeit haben aber natürlich alle, die im Laufe der drei Jahre das vierte Stockwerk bevölkert haben, gesorgt. Ob Imperial March und Synapsenkitzler als Handyklingelton, Schadenfreude beim Fußball (Francesca, das letzte Wort ist noch nicht gesprochen...), zünftige Meetings oder einfach nur entspanntes Sitzen auf der Terrasse im Sonnenschein – vielen Dank euch Viertstöcklern für diese Erlebnisse! Da werde ich auch darüber hinwegsehen, dass EINIGE (!) manchmal die Gelblichtlaborregeln nur allzu flexibel interpretiert haben. Aber was soll's – die Erde dreht sich vermutlich trotzdem weiter...

Ein großes Dankeschön auch euch, liebe Eltern, für die Unterstützung in den letzten Jahren. Schließlich hat sich in den letzten zehn Jahren der Ball ganz schön rund gedreht, und dass das so rund ablaufen konnte, ist zu einem großen Teil euer Verdienst.

Tu, Ingrīda, kā vistuvākais no visiem cilvēkiem, esi šī saraksta galā. Ir aizritējuši trīs piedzīvojumiem bagāti gadi, kuros bez disertācijas notika arī citas svarīgas lietas, un Tu man esi vēl un vēlreiz parādījusi, cik vērtīga un nozīmīga Tu man esi. Es ceru, ka spēju Tev sniegt tādu pašu sajūtu, un vēlos vienkārši sacīt: tā turpināsim! ☺

Curriculum Vitae

Work

From 04/2013	Engineer at Sick Engineering GmbH in Ottendorf-Okrilla, sensor developer
10/2010 – 11/2010	Research stay at Pohang University of Science and Technology (POSTECH), South Korea, Division of IT Convergence Engineering
03/2010 – 02/2013	PhD student at the chair „Materials Science and Nanotechnology“ in Dresden
10/2008 – 02/2010	Consultant at ALTEN Engineering, project at MTU Aero Engines Munich in the department “Special Measurement Techniques”

Internships

09/2007 – 10/2007	Research internship at Riga Technical University in Riga, Latvia in the department “Water Engineering and Technology”
11/2006 – 02/2007	Industry internship at Wessel Umwelttechnik GmbH in Hamburg, field application engineer for exhaust air facilities

Studies

03/2008 – 09/2008	Diploma thesis: optimization of antennae for RF measurements in an environmental application
03/2007 – 06/2007	Semester abroad at Ajou University in Suwon, South Korea
10/2003 – 09/2008	Study of environmental engineering at Bayreuth University

References

1. Nie, Z.; Petukhova, A.; Kumacheva, E. *Nat. Nanotechnol.* **2009**, *5*, 15–25.
2. Arico, A. S.; Bruce, P.; Scrosati, B.; Tarascon, J.-M.; van Schalkwijk, W. *Nat. Mater.* **2005**, *4*, 366–377.
3. Wu, Z.; Grossman, J. C. *Nano Lett.* **2008**, *8*, 2697–2705.
4. Ciuculescu, D.; Dumestre, F.; Comesaña-Hermo, M.; Chaudret, B.; Spasova, M.; Farle, M.; Amiens, C. *Chem. Mater.* **2009**, *21*, 3987–3995.
5. Wang, Z. L. *Nanowires and Nanobelts Materials, Properties and Devices Metal and Semiconductor Nanowires Volume I*; Kluwer Academic Publishers, 2003.
6. Lal, S.; Hafner, J. H.; Halas, N. J.; Link, S.; Nordlander, P. *Acc. Chem. Res.* **2012**,
7. Akimov, A. V.; Mukherjee, A.; Yu, C. L.; Chang, D. E.; Zibrov, A. S.; Hemmer, P. R.; Park, H.; Lukin, M. D. *Nature* **2007**, *450*, 402–406.
8. Li, J.; Koehne, J. E.; Cassell, A. M.; Chen, H.; Ng, H. T.; Ye, Q.; Fan, W.; Han, J.; Meyyappan, M. *Electroanalysis* **2005**, *17*, 15–27.
9. Cid, C. C.; Riu, J.; Maroto, A.; Rius, F. X. In *Carbon Nanotubes*; Balasubramanian, K., Burghard, M., Eds.; Methods in Molecular Biology; Humana Press, 2010; Vol. 625; Chapter 18, pp 213–225.
10. Patolsky, F.; Zheng, G.; Hayden, O.; Lakadamyali, M.; Zhuang, X.; Lieber, C. M. *P. Natl. Acad. Sci. USA* **2004**, *101*, 14017.
11. He, B.; Morrow, T. J.; Keating, C. D. *Curr. Opin. Chem. Biol.* **2008**, *12*, 522–528.
12. Balasubramanian, K. *Biosens. Bioelectron.* **2010**, *26*, 1195–204.
13. Xu, J.; Razeeb, K.; Sitaraman, S.; Mathewson, A. The fabrication of ultra long metal nanowire bumps and their application as interconnects. 2012.
14. Walter, E. C.; Penner, R. M.; Liu, H.; Ng, K. H.; Zach, M. P.; Favier, F. *Surf. Interface Anal.* **2002**, *34*, 409–412.
15. Hu, E. L.; Shaw, D. T. In *Nanostructure Science and Technology*; Siegel, R. W., Hu, E. L., Roco, M. C., Eds.; Synthesis and Assembly; Kluwer Academic Publishers, 2010; Chapter 2, pp 15–34.
16. Weber, W. M.; Geelhaar, L.; Unger, E.; Chèze, C.; Kreupl, F.; Riechert, H.; Lugli, P. *Phys. Status Solidi B* **2007**, *244*, 4170–4175.
17. Yang, P.; Yan, R.; Fardy, M. *Nano Lett.* **2010**, *10*, 1529–1536.

18. Chen, J.; Wiley, B. J.; Xia, Y. *Langmuir* **2007**, *23*, 4120–4129.
19. Wang, D.; Sheriff, B. A.; Heath, J. R. *Nano Lett.* **2006**, *6*, 1096–1100.
20. Mijatovic, D.; Eijkel, J. C. T.; Van Den Berg, A. *Lab Chip* **2005**, *5*, 492.
21. Sun, Y.; Xia, Y. *J. Adv. Mater.* **2002**, *14*, 833–837.
22. Kim, W.; Ng, J. K.; Kunitake, M. E.; Conklin, B. R.; Yang, P. *J. Am. Chem. Soc.* **2007**, *129*, 7228–7229.
23. Alaca, B. E. *Int. Mater. Rev.* **2009**, *54*, 245–282.
24. Pohl, H. A. *Dielectrophoresis*; Cambridge University Press, 1978.
25. Kuzyk, A. *Electrophoresis* **2011**, *32*, 2307–2313.
26. Li, M.; Bhiladvala, R. B.; Morrow, T. J.; Sioss, J. A.; Lew, K.-K.; Redwing, J. M.; Keating, C. D.; Mayer, T. S. *Nat. Nanotechnol.* **2008**, *3*, 88–92.
27. Papadakis, S.; Hoffmann, J.; Deglau, D.; Chen, A. *Nanoscale* **2010**, *3*, 1059–1065.
28. Hermanson, K. D.; Lumsdon, S. O.; Williams, J. P.; Kaler, E. W.; Velev, O. D. *Science* **2001**, *294*, 1082–1086.
29. Cheng, C.; Gonela, R. K.; Gu, Q.; Haynie, D. T. *Nano Lett.* **2005**, *5*, 175–178.
30. Nerowski, A.; Poetschke, M.; Bobeth, M.; Opitz, J.; Cuniberti, G. *Langmuir* **2012**, *28*, 7498–7504.
31. La Ferrara, V.; Madathil, A. P.; De Girolamo Del Mauro, A.; Massera, E.; Polichetti, T.; Rametta, G. *Electrophoresis* **2012**, *33*, 2086–2093.
32. Flanders, B. N. *Mod. Phys. Lett. B* **2012**, *26*, 1130001.
33. Bhatt, K. H.; Velev, O. D. *Langmuir* **2004**, *20*, 467–476.
34. Ozturk, B.; Talukdar, I.; Flanders, B. N. *Nanotechnology* **2007**, *18*, 365302.
35. Gierhart, B. C.; Howitt, D. G.; Chen, S. J.; Smith, R. L.; Collins, S. D. *Langmuir* **2007**, *23*, 12450–12456.
36. Ranjan, N.; Vinzelberg, H.; Mertig, M. *Small* **2006**, *2*, 1490–1496.
37. Wu, Y.; Xiang, J.; Yang, C.; Lu, W.; Lieber, C. M. *Nature* **2004**, *430*, 61–5.
38. Ditlbacher, H.; Hohenau, A.; Wagner, D.; Kreibitz, U.; Rogers, M.; Hofer, F.; Aussenegg, F.; Krenn, J. *Phys. Rev. Lett.* **2005**, *95*, 257403.
39. Kawasaki, J. K.; Arnold, C. B. *Nano Lett.* **2010**, *11*, 781–785.
40. Ranjan, N. Dielectrophoretic Formation of Nanowires and Devices. Ph.D. thesis, Technische Universität Dresden, 2009.

41. Shelimov, B.; Lambert, J. F.; Che, M.; Didillon, B. *J. Am. Chem. Soc.* **1999**, *121*, 545–556.
42. Mabbot, G. A. *J. Chem. Educ.* **1983**, *60*, 697–702.
43. Eftekhari, A. *Chem. Phys. Lett.* **2003**, *381*, 427–433.
44. Schwabe, K. *Physikalische Chemie - 1 : Physikalische Chemie*; Akademie-Verlag Berlin, 1986.
45. Lumsdon, S. O.; Scott, D. M. *Langmuir* **2005**, *21*, 4874–4880.
46. Suárez-Iglesias, O.; Medina, I.; Pizarro, C.; Bueno, J. L. *Chem. Eng. Sci.* **2007**, *62*, 6499–6515.
47. Laliberté, M. *J. Chem. Eng. Data* **2007**, *52*, 321–335.
48. NIST Standard Reference Database. 2011; <http://webbook.nist.gov/chemistry/fluid/>.
49. Seeton, C. J. *Tribol. Lett.* **2006**, *22*, 67–78.
50. Randles, J. E. B. *Trans. Faraday Soc.* **1952**, *48*, 828–832.
51. Marcus, Y. *Biophys. Chem.* **1994**, *51*, 111–127.
52. Elding, L. I. *Acta Chem. Scand.* **1970**, *24*, 1527–1540.
53. Elding, L. I. *Inorg. Chim. Acta* **1978**, *28*, 255–262.
54. Wu, L.; Schwederski, B. E.; Margerum, D. W. *Inorg. Chem.* **1990**, *29*, 3578–3584.
55. Toshima, N.; Takahashi, T.; Hirai, H. *Chem. Lett.* **1985**, *14*, 1245–1248.
56. Ciacchi, L. C.; Pompe, W.; De Vita, A. *J. Am. Chem. Soc.* **2001**, *123*, 7371–7380.
57. Hughes, M. P. *Nanotechnology* **2000**, *11*, 124.
58. Glicksman, M. E.; Lupulescu, A. O. *J. Cryst. Growth* **2004**, *264*, 541–549.
59. Langer, J. S. *Phys. Rev. Lett.* **1980**, *44*, 1023–1026.
60. Barton, J. L.; Bockris, J. O. *Proc. R. Soc. A* **1962**, *268*, 485–505.
61. Markov, I. V. *Crystal Growth for Beginners: Fundamentals of Nucleation, Crystal Growth and Epitaxy (2nd Edition)*; World Scientific, 2003.
62. Milchev, A. *Electrocrystallization: Fundamentals of Nucleation and Growth*; Kluwer Academic Press, 2002.
63. Langer, J. S. *Rev. Mod. Phys.* **1980**, *52*, 1–30.

64. Ranjan, N.; Mertig, M.; Cuniberti, G.; Pompe, W. *Langmuir* **2009**, *26*, 552–559.
65. Bhatt, K. H.; Grego, S.; Velev, O. D. *Langmuir* **2005**, *21*, 6603–6612.
66. Schennach, R.; Bechtold, E. *Surf. Sci.* **1997**, *380*, 9–16.
67. Holzwarth, J.; Strohmaier, L. *Ber. Bunsenges. Phys. Chem.* **1973**, *77*, 1145–1151.
68. Campion, R. J.; Deck, C. F.; King, P.; Wahl, A. C. *Inorg. Chem.* **1967**, *6*, 672–681.
69. Ferapontova, E.; Gorton, L. *Bioelectrochemistry* **2002**, *55*, 83–87.
70. Peter, L. M.; Dürr, W.; Bindra, P.; Gerischer, H. *J. Electroanal. Chem.* **1976**, *71*, 31–50.
71. Bazant, M. Z.; Thornton, K.; Ajdari, A. *Phys. Rev. E* **2004**, *70*, 021506.
72. Bazant, M. Z.; Storey, B. D.; Kornyshev, A. A. *Phys. Rev. Lett.* **2011**, *106*, 46102.
73. Grier, D.; Ben-Jacob, E.; Clarke, R.; Sander, L. M. *Phys. Rev. Lett.* **1986**, *56*, 1264–1267.
74. Gao, W.; Baker, T. A.; Zhou, L.; Pinnaduwa, D. S.; Kaxiras, E.; Friend, C. M. *J. Am. Chem. Soc.* **2008**, *130*, 3560–3565.
75. Thapa, P. S.; Ackerson, B. J.; Grischkowsky, D. R.; Flanders, B. N. *Nanotechnology* **2009**, *20*, 235307.
76. Ciobanas, A. I.; Bejan, A.; Fautrelle, Y. *J. Phys. D: Appl. Phys.* **2006**, *39*, 5252–5266.
77. Bejan, A.; Lorente, S. *J. Appl. Phys.* **2006**, *100*, 041301.
78. Gierer, A.; Wirtz, K. *Z. Naturforschg.* **1953**, *8a*, 532–538.
79. Trivedi, R.; Lipton, J.; Kurz, W. *Acta Metall.* **1987**, *35*, 965–970.
80. Shironita, S.; Mori, K.; Shimizu, T.; Ohmichi, T.; Mimura, N.; Yamashita, H. *Appl. Surf. Sci.* **2008**, *254*, 7604–7607.
81. Barabasi, A. L.; Stanley, H. E. *Fractal Concepts in Surface Growth*; Cambridge University Press, 1995.
82. Kumar, V.; Kawazoe, Y. *Phys. Rev. B* **2008**, *77*, 205418.
83. Salzemann, C.; Petit, C. *Langmuir* **2012**, *28*, 4835–4841.
84. Lim, B.; Wang, J.; Camargo, P.; Cobley, C.; Kim, M.; Xia, Y. *Angew. Chem., Int. Ed.* **2009**, *48*, 6304–6308.
85. Peng, Z.; Yang, H. *Nano Today* **2009**, *4*, 143–164.

86. Lüth, H. *Quantenphysik in der Nanowelt*; Springer, 2009.
87. Järvi, T.; Kuronen, A.; Meinander, K.; Nordlund, K.; Albe, K. *Phys. Rev. B* **2007**, *75*, 115422.
88. Järvi, T. T.; Kuronen, A.; Nordlund, K.; Albe, K. *J. Appl. Phys.* **2009**, *106*, 063516.
89. Gür, F. N. Master Thesis.
90. Janik, T. Student project.
91. Suehiro, J.; Hamada, R.; Noutomi, D.; Shutou, M.; Hara, M. *J. Electrostat.* **2003**, *57*, 157–168.
92. Lu, Y. C.; Chuang, Y. S.; Chen, Y. Y.; Shu, A. C.; Hsu, H.; Chang, H. Y.; Yew, T. R. *Biosens. Bioelectron.* **2008**, *23*, 1856–1861.
93. Küpfmüller, K.; Mathis, W.; Reibiger, A. *Theoretische Elektrotechnik - Eine Einführung*; Springer, 2008.
94. Kark, K. *Antennen und Strahlungsfelder*; Vieweg und Teubner, 2006.
95. Kapur, P.; McVittie, J. P.; Saraswat, K. C. *IEEE Trans. Electron Devices* **2002**, *49*, 590–597.
96. Salahuddin, S.; Lundstrom, M.; Datta, S. *IEEE Trans. Electron Devices* **2005**, *52*, 1734–1742.
97. Ma, W. G.; Wang, H. D.; Zhang, X.; Wang, W. *J. Appl. Phys.* **2010**, *108*, 064308.
98. Mayadas, A. F.; Shatzkes, M.; Janak, J. F. *Appl. Phys. Lett.* **1969**, *14*, 345–347.
99. Mayadas, A. F.; Shatzkes, M. *Phys. Rev. B* **1970**, *1*, 1382–1389.
100. Stiebler, M. In *Dubbel - Taschenbuch für den Maschinenbau*; Beitz, W., Grote, K., Eds.; Elektrotechnik; Springer, 2001; Chapter V, pp 1–64.
101. Itakura, K.; Yuki, K.; Kurokawa, S.; Yasuda, H.; Sakai, A. *Phys. Rev. B* **1999**, *60*, 11163–11170.
102. Yasuda, H.; Sakai, A. *Phys. Rev. B* **1997**, *56*, 1069–1072.
103. Zhang, C. H.; Bürki, J.; Stafford, C. *Phys. Rev. B* **2005**, *71*, 235404.
104. Lienig, J. *Introduction to Electromigration-Aware Physical Design*. 2006.
105. Macdonald, J. R. *Impedance Spectroscopy - Emphasizing Solid Materials and Systems*; John Wiley & Sons, 1987.
106. Ende, D.; Mangold, K. M. *Chem. Unserer Zeit* **1993**, *27*, 134–140.

107. Smejtek, P.; Hsu, K.; Perman, W. H. *Biophys. J.* **2005**, *16*, 319–336.
108. Einolf Jr., C. W.; Carstensen, E. L. *Biophys. J.* **1969**, *9*, 634–643.
109. Bai, W.; Zhao, K. S.; Asami, K. *Biophys. Chem.* **2006**, *122*, 136–142.
110. Rosenberg, B. J. *Chem. Phys.* **1962**, *36*, 816–823.
111. Smith, S. R.; Foster, K. R. *Phys. Med. Biol.* **1985**, *30*, 965–973.
112. Bunthawin, S.; Wanichapchart, P.; Tuantranont, A.; Coster, H. G. *Biomicrofluidics* **2010**, *4*, 014102.
113. Boussaad, S.; Tao, N. J. *Appl. Phys. Lett.* **2002**, *80*, 2398.
114. Austin, M.; Chou, S. Y. *J. Vac. Sci. Technol. B Nanotechnol. Microelectron.* **2002**, *20*, 665–667.
115. Zhao, M.; Yu, M.; Blick, R. H. *IEEE J. Sel. Top. Quant.* **2012**, *18*, 166–175.
116. Sakamoto, Y.; Oba, Y.; Maki, H.; Suda, M.; Einaga, Y.; Sato, T.; Mizumaki, M.; Kawamura, N.; Suzuki, M. *Phys. Rev. B* **2011**, *83*, 104420.
117. Teng, X.; Han, W.-Q.; Ku, W.; Hücker, M. *Angew. Chem., Int. Ed.* **2008**, *120*, 2085–2088.
118. Smogunov, A.; Dal Corso, A.; Delin, A.; Weht, R.; Tosatti, E. *Nat. Nanotechnol.* **2008**, *3*, 22–25.
119. Yogeswaran, U.; Chen, S.-M. *Sensors* **2008**, *8*, 290–313.
120. Kaye, B. H. *A Random Walk Through Fractal Dimension*; VCH Publishers, 1989.
121. Evertsz, C. J. G.; Zahlten, C.; Peitgen, H. O.; Zuna, I.; Kaick, G. V. Distribution of Local-Connected Fractal Dimension and the Degree of Liver Fattiness from Ultrasound. *Fractals in Biology and Medicine*, 1993.
122. Lopes, R.; Betrouni, N. *Medical Image Analysis* **2009**, *13*, 634–649.
123. Otsu, N. *IEEE T. Syst. Man Cyb.* **1979**, *9*, 62–66.